

Core plasma turbulence in Wendelstein 7-X

Inauguraldissertation

zur

Erlangung des akademischen Grades eines
Doktors der Naturwissenschaften
(Dr. rer. Nat.)

der

Mathematisch-Naturwissenschaftlichen Fakultät

der

Universität Greifswald

vorgelegt von
Jan-Peter Böhner

Greifswald, 24.01.2022

Abstract

This work investigates turbulence in the core plasma of the optimised stellarator Wendelstein 7-X. It focuses on experimental characterisation and evaluation of the electrostatic micro-instabilities, which drive turbulent fluctuations, and the saturation of turbulence by zonal flows. Expectations for Wendelstein 7-X are formulated by reviewing theoretical work and with the help of gyrokinetic simulations. The experimental analysis centres on line-integrated density fluctuation measurements with the phase contrast imaging diagnostic in electron cyclotron heated hydrogen discharges. An absolute amplitude calibration was implemented, and a method for reliable determination of dominant phase velocities in wavenumber-frequency spectra of density fluctuations has been developed. Line-averaged density fluctuation levels are observed to vary between magnetic configurations. The wavenumber spectra exhibit a dual cascade structure, indicating fully developed turbulence. The dominant instability driving turbulent density fluctuations on transport relevant scales is identified as ion-temperature-gradient-driven modes, which are mainly localised in the edge region of the confined plasma. Despite the line-integrated nature of the measurement, the localisation of density fluctuations is shown by comparing their dominant phase velocity with the radial profile of the $\mathbf{E} \times \mathbf{B}$ rotation velocity due to the ambipolar neoclassical electric field. Nonlinear gyrokinetic simulations and a simplified plasma rotation model within a synthetic diagnostic confirm the localisation. Oscillations of the dominant phase velocity indicate the existence of zonal flows as a saturation mechanism of ion-temperature-gradient-driven turbulence. A direct effect on turbulent density fluctuation amplitudes and radial transport is observed.

Zusammenfassung

In dieser Arbeit wird die Turbulenz im Kernplasma des optimierten Stellarators Wendelstein 7-X untersucht. Der Schwerpunkt liegt auf der experimentellen Auswertung der elektrostatischen Mikroinstabilitäten, die turbulente Fluktuationen antreiben, und der Sättigung der Turbulenz durch zonale Strömungen. Konkrete Erwartungen für Wendelstein 7-X werden durch Zusammenfassen theoretischer Arbeiten und durch gyrokinetische Simulationen formuliert. Die experimentelle Auswertung konzentriert sich auf Messungen linienintegrierter Dichtefluktuationen mit der Phasenkontrastabbildungsdiagnostik in elektronenzyklotronbeheizten Wasserstoffentladungen. Es wurde eine absolute Amplitudenkalibrierung implementiert und eine Methode zur zuverlässigen Bestimmung dominanter Phasengeschwindigkeiten in Wellenzahl-Frequenz-Spektren entwickelt. Es wurde beobachtet, dass die liniengemittelten Dichtefluktuationslevel zwischen verschiedenen magnetischen Konfigurationen variieren. Die Wellenzahlspektren weisen eine Doppelkaskadenstruktur auf, die auf eine voll entwickelte Turbulenz hinweist. Die vorherrschende Instabilität, die turbulente Dichtefluktuationen auf transportrelevanten Skalen antreibt, wird als Ionentemperaturgradientgetriebene Moden identifiziert, die hauptsächlich in der Randregion des eingeschlossenen Plasmas lokalisiert sind. Trotz des linienintegrierten Charakters der Messung kann die Lokalisierung der Dichtefluktuationen durch einen Vergleich ihrer dominanten Phasengeschwindigkeit mit dem radialen Profil der $\mathbf{E} \times \mathbf{B}$ -Rotationsgeschwindigkeit aufgrund des ambipolaren neoklassischen elektrischen Feldes gezeigt werden. Nichtlineare gyrokinetische Simulationen und ein vereinfachtes Plasmarotationsmodell als Teil einer synthetischen Diagnostik bestätigen die Lokalisierung. Oszillationen der dominanten Phasengeschwindigkeit deuten auf die Existenz von zonalen Strömungen als Sättigungsmechanismus der Turbulenz hin. Es wird eine direkte Auswirkung auf die Amplituden der turbulenten Dichtefluktuation und den radialen Transport beobachtet.

Contents

Abstract	iii
Zusammenfassung	v
1 Introduction	1
2 Turbulence and Transport	7
2.1 Fluid turbulence and energy cascades	7
2.2 Transport in magnetic confinement devices	10
2.3 Wendelstein 7-X	19
3 Plasma Turbulence	23
3.1 Gyrokinetic description	24
3.2 Electrostatic micro-instabilities	30
3.3 Micro-instabilities in W7-X	40
3.4 Zonal flows	51
4 Diagnostics and Analysis	57
4.1 Phase contrast imaging	58
4.2 Data analysis tools	69
5 Characterisation of turbulent density fluctuations	89
5.1 Turbulent density fluctuation spectra	89
5.2 Turbulent density fluctuation amplitudes	96
6 Radial structure of density fluctuations	105
6.1 Reference discharge scenario	106
6.2 Dominant fluctuation propagation velocity	107
6.3 $E \times B$ velocity and neoclassical radial electric field	110
6.4 Comparison of velocities	112

Contents

6.5	Simplified rotation model with SPCI	117
6.6	Gyrokinetic simulations	121
7	Zonal-flow-like modulations of the binormal flow velocity	127
7.1	Characterisation	129
7.2	Magnetic configuration dependency	133
7.3	1-2 kHz feature in the medium range iota case	137
7.4	Zonal flow hypothesis	142
7.5	Zonal flow modelling	146
7.6	Global mode hypothesis	150
8	Summary and Conclusion	153
	Bibliography	157
	Acronyms	175
	List of Figures	177
	Statutory declaration	181
	Acknowledgements	183

1

Introduction

The American physicist and Nobel laureate Richard P. Feynman wrote in his famous lectures on physics about turbulence,

There is a physical problem that is common to many fields, that is very old, and that has not been solved. It is not the problem of finding new fundamental particles, but something left over from a long time ago—over a hundred years. Nobody in physics has really been able to analyze it mathematically satisfactorily in spite of its importance to the sister sciences. It is the analysis of circulating or turbulent fluids. (R. P. Feynman, *The Feynman lectures on physics*, 1965)

whereas German physicist and Nobel laureate Werner Heisenberg, who founded the Max-Planck Institute for Plasma Physics (IPP) and was an early advocate of nuclear fusion research in Germany, is attributed the quote,

When I meet God, I'm going to ask him two questions: why relativity? And why turbulence? I really believe he'll have an answer for the first. (W. Heisenberg, 1976)

The two quotes neatly capture the ambivalent feelings one meets when approaching the notoriously complex problem of turbulence, which puzzled some of the greatest minds in mathematics and physics. The definition of turbulence on its own is not trivial, since there are only few universal features. The search for universal features from basic principle is what is

commonly known as »the turbulence problem« [1]. In fact, one of the famous millennium problems in mathematics is the proof that unique solutions exist for the Navier-Stokes equation, which describes the (turbulent) flow of fluids [2].

There are, however, some key aspects which are necessary for turbulence to arise: being an inherently nonlinear phenomenon, the equations describing the turbulent system must contain a nonlinearity. In contrast to chaotic systems, turbulent systems require many degrees of freedom. Furthermore, there needs to be some kind of dissipation for turbulence to reach a saturated state. The principle phenomenology which arises can be described as follows: a source of free energy in the system drives instabilities, which grow and develop into complex flow patterns and fluctuations. Eddies of various sizes distribute the energy over a large range of length scales via nonlinear interaction of the flow. Energy leaves the turbulence through dissipation, such that a state of statistical equilibrium is reached, which is called saturation. The basic ideas of fluid turbulence as well as energy cascades are introduced in more detail in section 2.1.

Feynman claims turbulence is one of the most important problems in classical physics. But what makes it so important? While the derivation of universal features is a rather academic problem, there are many fields of science in which turbulence and its implications cause very real problems. Aircraft design and construction have to deal with turbulence, because it affects the lift of the wings, as do weather forecasts and climate models, since turbulence also occurs on continental scales affecting the dynamics of the atmosphere. Another relevant consequence of turbulence in many applications is transport. Turbulent eddies and whirls are much more efficient at transporting momentum, particles and heat across a medium than simple diffusion due to a gradient. This is the reason why we intuitively stir our coffee (or analogously tea, for the British reader) to mix in cold milk instead of waiting for it to diffuse. Without effective turbulent transport, pollution in metropolitan areas would accumulate indefinitely and the heat produced by nuclear fusion in the core of the sun would not be able to escape and reach Earth within an acceptable time [3]. There are mainly two aspects which determine the severeness of turbulent transport: the *amplitude* as well as the *spatial scale* of fluctuations. On the one hand, these are connected to the energy injection, i. e. to how much free energy is available in the system for turbulence and how effective and on which scale instabilities introduce this

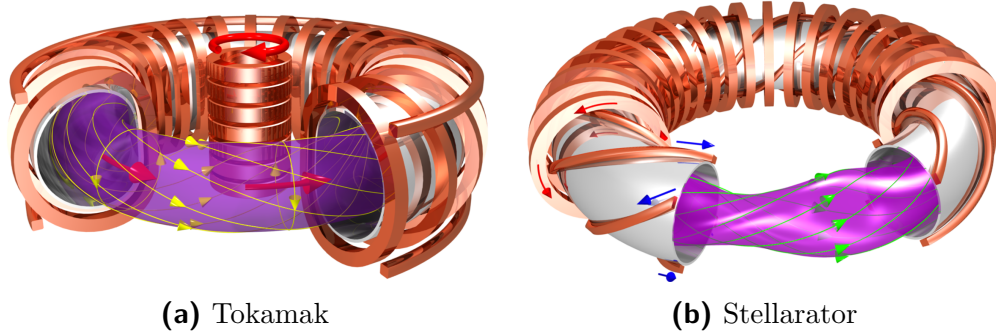


Figure 1.1: Illustrations of the principle concepts of tokamak and stellarator.
Graphics: C. Brandt, IPP 2011

energy to the turbulent flow. On the other hand, the nonlinear distribution of energy across scales as well as the saturation mechanism affect the scale and amplitude of saturated turbulent fluctuations causing transport.

This work is concerned with the specific application of turbulence in hot fusion plasmas. Turbulent transport plays a major role in magnetic confinement fusion (MCF) research, which aims at harvesting energy from nuclear fusion in magnetically confined hot plasmas. The reaction in nuclear fusion reactors on Earth is similar to the one in the sun, but turbulent transport of heat is disadvantageous. Temperatures which exceed the core temperature of the sun must be reached and sustained for viable energy production. In currently technologically practicable devices, fast turbulent heat loss inhibits reaching the conditions at which the plasma can maintain the core temperature by internally heating itself via fusion reactions.

In the 1950s, two concepts for the confinement of plasma in a torus-shaped helically twisted magnetic field were developed: the tokamak and the stellarator. Figure 1.1 shows schematic drawings of how the magnetic field is generated in each concept. The toroidal field component, which goes the long way around the torus, is generated by external magnetic coils in either case. The poloidal field component, which goes the short way around the torus, is generated by a strong toroidal plasma current in a tokamak and by additional external coils in a stellarator. In both concepts, nested magnetic flux surfaces are generated on which the magnetic force balances the thermal pressure of the plasma. Besides the use or lack of a strong plasma current, a major difference between tokamaks and stellarators is the

symmetry of the magnetic field: while the tokamak field is axisymmetric, the stellarator field inherently lacks symmetry in real space coordinates. As in all fields of physics, symmetry is advantageous and tokamaks exhibited better confinement than classical stellarators. Only optimised stellarators which approach quasi-symmetry, i. e. a symmetry in magnetic field-aligned coordinates, achieve similar or better confinement than comparably sized tokamaks. For more detailed discussions of the basic concepts, the reader is referred to extensive existing literature on tokamaks (e. g. [4]), stellarators (e. g. [5–7]) and their comparison [8, 9].

The confinement quality is still a central topic of MCF research, since it is key for a successful power plant operation. The radial transport of particles and heat from the core to the boundary of the plasma determines whether a fusion relevant pressure can be reached and sustained in the plasma core and ultimately the feasibility of MCF for power production. It can be divided into two contributions: collisional and anomalous transport. Collisional transport arises due to binary collisions between electrons and ions on the scale of the gyromotion, which is also called *classical transport*. In toroidal magnetic field configurations, the geometry must be taken into account, leading to an increased collisional transport, which is called *neoclassical (NC)*. However, experimentally measured diffusion, e. g. in tokamaks, is much larger than NC theory predicts. The additional radial transport was traditionally referred to as *anomalous* and is attributed to turbulent fluctuations. A more detailed introduction to neoclassical and turbulent transport is provided in section 2.2. It was found that turbulent transport scales unfavourably with operational parameters and it became clear that successful operation of tokamaks as fusion reactors relies on improved confinement regimes such as the H-mode [10, 11], where turbulent transport is suppressed by an edge transport barrier [12]. Because of its apparent importance for confinement, theoretical and experimental efforts were started to understand the strong turbulent transport and its suppression in tokamak plasmas. After decades worth of research, a fairly good understanding of the fundamental mechanisms exists, even though the prediction of turbulent transport levels is still challenging. For reviews on this topic see HORTON [13] and DOYLE *et al.* [14].

In classical stellarators, there is additional collisionless transport, causing the overall NC transport to be so large that the turbulent contribution plays a minor role for the overall confinement. Accordingly, the research on tur-

bulence in stellarators is not quite as advanced as for tokamaks. However, NC transport in stellarators can be reduced by optimising the magnetic field geometry. With the advent of advanced and optimised stellarators, turbulence becomes the confinement-limiting factor in stellarators as well. One example of an optimised stellarator and focus of this work is Wendelstein 7-X (W7-X). It is a quasi-isodynamic stellarator [15], first of its kind and one of the largest existing stellarators [16]. The technical details of the Wendelstein 7-X experiment are described in section 2.3. Recent results have provided evidence for improved NC confinement [17], i. e. confirmed that the optimisation is indeed effective. Accordingly, turbulent heat transport was found to be the dominant mechanism for heat losses [18–21], similarly to tokamak plasma confinement.

So far, mostly analytical and numerical studies have provided progress in understanding the difference between turbulence in optimised stellarators and its tokamak counterpart [22–29]. Turbulence is in many aspects similar in both concepts with distinct differences due to the magnetic field geometry [8, 26]. After decades of theoretical work, experimental data of core plasma turbulence in a stellarator dominated by turbulent heat transport has become available with the latest operation phase of W7-X. The primary tool for core turbulence measurements is the phase contrast imaging (PCI) diagnostic, which provides scale-resolved line-integrated density fluctuation measurements.

This work, for the first time, takes a general approach to experimentally characterise different aspects of core turbulence in the highly optimised stellarator W7-X. Instead of turbulent transport itself, which can not be measured directly, the fundamental mechanisms of excitation and saturation of plasma turbulence are investigated. For the injection of energy, the type of electrostatic micro-instability which drives turbulent fluctuations is identified. Regarding the saturation, the appearance of zonal flows is monitored. First, theoretical understanding is reviewed in chapter 3. The mathematical description, physical mechanisms and device-specific features of the most relevant electrostatic micro-instabilities as well as zonal flows are introduced. With the help of numerical simulations, tangible expectations are formulated for W7-X. The PCI diagnostic and related data analysis tools are introduced in chapter 4. Experimental data is analysed with direct comparisons to dedicated numerical simulations. For the characterisation of the fundamental transport ingredients, first frequency and wavenumber spec-

tra, i. e. temporal and spatial scales, as well as amplitudes of line-integrated density fluctuations are investigated in chapter 5. Despite the line-integrated nature of the measurement, the radial distribution of density fluctuations can be analysed, which is described in chapter 6 and provides indications for the dominant electrostatic micro-instability. In chapter 7, experimental indications for turbulence saturation via zonal flows are evaluated. Finally, in chapter 8, the results are summarised and the main conclusions are drawn.

2

Turbulence and Transport

2.1 Fluid turbulence and energy cascades

Turbulence can be observed in many physical systems, most prominently in fluids, which we encounter in everyday life, e. g. in wind or flowing water. Fluid turbulence is described by the Navier-Stokes equation for the incompressible flow ($\nabla \cdot \mathbf{u} = 0$) [30]

$$\partial_t \mathbf{u} + \mathbf{u} \cdot \nabla \mathbf{u} = - (1/\rho) \nabla p + \nu \nabla^2 \mathbf{u}, \quad (2.1)$$

where \mathbf{u} is the flow velocity, ρ is the mass density and ν the viscosity of the fluid. The nonlinearity, which makes all the trouble, is contained in the term $\mathbf{u} \cdot \nabla \mathbf{u}$ and dissipation is described by $\nu \nabla^2 \mathbf{u}$. The Navier-Stokes equation contains all necessary physics for the description of turbulence and is known for almost 200 years, so why is turbulence still a problem? As mentioned in the introduction, it is not yet possible to show that unique solutions to the Navier-Stokes equation exist, let alone derive universal laws for turbulence. However, efforts for finding universal features with statistical and dimensional analysis were partially successful. One of the central ideas is the cascade model, which was described by Leonardo da Vinci, who was also the first to introduce the term *turbulence* (*turbolenza*) [3], and formally introduced by RICHARDSON [31] in 1922: energy is passed on between fluctuations of different scales, which is observed as eddies breaking into smaller eddies until viscosity is dominant. Andrey Kolmogorov derived in his seminal papers from 1941 expressions for the distribution of energy across scales in a cascade by fundamental dimensional arguments. He assumed inertial,

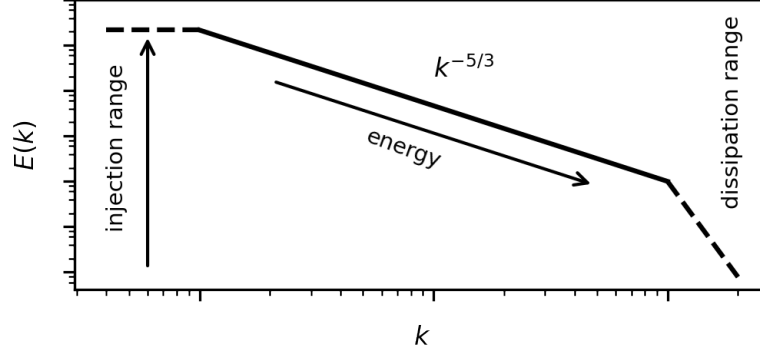


Figure 2.1: Inertial range of the energy cascade to smaller scales in 3D turbulence with Kolmogorov scaling. Energy enters the system at large scales and is transported to small scales, where it dissipates.

i. e. energy conserving, nonlinear processes, and postulated that solutions of the Navier-Stokes equation have the same scale invariance as the equation itself [3]. The interaction between scales is described by *structure functions*, which are moments of $\delta\mathbf{u}(r) = \mathbf{u}(x+r) - \mathbf{u}(x)$, the velocity difference on the scale, r . Following the argument of scale invariance, Kolmogorov derived an explicit expression of the third-order structure function, the famous four-fifth-law [1]. The four-fifth-law was interpreted independently amongst others by HEISENBERG & TAYLOR [32] in 1948 for the energy density spectrum as,

$$E(k) \sim k^{-5/3}, \tag{2.2}$$

where $k = 2\pi/r$ is the inverse length scale of the flow structures. The energy cascade is illustrated in figure 2.1. In the injection range, energy enters the system and is distributed to other scales according to the four-fifth-law, yielding the energy spectrum of equation (2.2). The interaction of scales is local, meaning energy is exchanged between neighbouring scales and thus cascades across the inertial range. At small scales, it is dissipated e. g. due to viscosity. Saturation is reached, when $E(k)$ is constant in time at constant energy input. In terms of the coffee (or tea) example, we insert energy into the fluid by stirring on the scale of the cup size. Smaller eddies form and break into even smaller eddies. Even if we continue stirring, the fluctuations

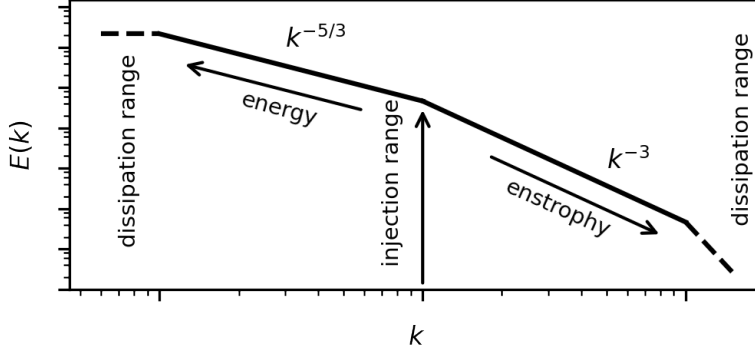


Figure 2.2: The two inertial ranges of the dual-cascade in 2D turbulence with scalings according to Kraichnan. Energy enters the system at injection range. The energy transfer dominates towards larger scales leading to an inverse energy cascade. The enstrophy transfer dominates towards smaller scales and results in the direct cascade.

do not become indefinitely violent, because kinetic energy is transformed into heat by viscous dissipation at the smallest scales.

This picture holds true for fully developed 3-dimensional homogeneous isotropic turbulence. In 2-dimensional systems, an additional cascade can be observed. The vorticity, $\boldsymbol{\omega} = \nabla \times \mathbf{u}$, which describes the spinning of the flow, is mostly aligned along a certain direction in 2-dimensional systems. Examples for 2-dimensional environments exhibiting turbulence are fast rotating systems such as stellar accretion disks or systems with one length scale significantly shorter than others such as oil films or planetary atmospheres. The aligned vorticity gives rise to a new invariant, i. e. conserved quantity, which is called enstrophy, $\Omega = \frac{1}{2}\langle|\boldsymbol{\omega}|\rangle^2$ [33]. It is analogous to the energy density, $E = \frac{1}{2}\langle|\mathbf{u}|\rangle^2$. Both energy and enstrophy are interchanged in a cascade, which is called a *dual-cascade*, but now there are two separate inertial ranges due to different scale dependencies of energy and enstrophy exchange. The dual-cascade scenario was derived by KRAICHNAN [34] in 1967 and is illustrated in figure 2.2. Enstrophy transport dominates the direct cascade towards higher wavenumbers and results in the energy density distribution, $E(k) \sim k^{-3}$. Energy transport dominates the inverse cascade towards lower wavenumbers and yields the same result as the direct cas-

cade in 3-dimensional systems, $E(k) \sim k^{-5/3}$. The inverse energy cascade increases the energy in the system until mean flow on the system scale length is excited and leads to second dissipation range. This may seem counterintuitive but is observed in planetary atmospheres. The zones and belts of the Jovian atmosphere as well as the jet streams on Earth are examples of zonal flows (ZFs), which are equatorial bands of high mean flow velocity with alternating direction and strong velocity shear in between. ZFs play an important role for turbulence saturation and are described in section 3.4 in more detail.

Magnetised plasmas have to be treated differently from neutral fluids, but in terms of turbulence they behave similarly to a 2-dimensional fluid, since turbulent vortices are mainly aligned with the highly directed magnetic field. Accordingly, dual-cascades as well as ZFs are observed in plasma turbulence.

2.2 Transport in magnetic confinement devices

Particle and heat diffusive transport in magnetic confinement devices can be described as Fickian processes:

$$\mathbf{\Gamma} = -D\nabla n, \quad (2.3)$$

$$\mathbf{q} = -n\chi\nabla T, \quad (2.4)$$

where $\mathbf{\Gamma}$ is the particle flux density, D is the diffusion coefficient and n is the particle number density. Analogously, \mathbf{q} is the heat flux density, χ is the thermal diffusivity and T is the temperature. As described in the introduction, the transport has a collisional and an anomalous contribution. They are additive, i. e. in terms of diffusion coefficients one may write, $D = D_{\text{coll}} + D_{\text{ano}}$ and analogously for χ . In the following, the two contributions are each introduced with respect to their physical mechanism and the respective diffusion coefficient.

2.2.1 Collisional transport

The one-dimensional *random walk* process is an intuitive approach for describing collisional transport: a particle is displaced due to a collision by the step length l after a typical step time τ . The resulting diffusion coefficient

is given by

$$D_{\text{rw}} = \frac{l^2}{2\tau}. \quad (2.5)$$

With this approach, the discussion of the various transport processes in tokamaks and stellarators can be reduced to a discussion of the respective characteristic length and time scales.

In magnetised plasma, the fundamental step size is the Lamor radius of the electron gyromotion, ρ_{Le} , and the time scale is the electron-ion collision time, τ_{ei} , yielding the classical diffusion coefficient [35]

$$D_{\text{cl}} = \frac{\rho_{Le}^2}{2\tau_{ei}} = \frac{e^2 n_e \ln \Lambda \sqrt{m_e}}{8\sqrt{2}\pi\epsilon_0^2 B^2 \sqrt{T_e}}, \quad (2.6)$$

where e is the elementary charge, $\ln \Lambda$ the Coulomb logarithm, ϵ_0 the vacuum permittivity, n_e , m_e and T_e are the electron density, mass and temperature, respectively, and B is the magnetic field strength.

2.2.2 Neoclassical transport

The transport in a plasma is only classical if the magnetic field is homogeneous. In the toroidal geometry of magnetic confinement devices, the inhomogeneous magnetic field gives rise to drifts and more complex particle trajectories. This leads to a number of additional transport processes, which generally exceed the classical transport by more than one order of magnitude. The increased diffusion due to the toroidal geometry is called NC transport. In the following, the different processes and regimes are explained.

Pfirsch-Schlüter regime

A magnetic field in toroidal geometry must decrease from the inboard to the outboard side of the torus (on average across a flux surface). This magnetic field gradient causes a guiding centre drift in opposite directions for ions and electrons, which results in a charge separation and a vertical electric field in the plasma. The charge separation is compensated by the Pfirsch-Schlüter current due to particle movement along the magnetic field lines which connect the two regions. Because of the finite resistivity of the

plasma, a part of the vertical electric field remains and causes an $\mathbf{E} \times \mathbf{B}$ guiding centre drift for the particles. As the particles go around the torus, this leads to a radial displacement of the guiding centre orbit from the magnetic flux surface, δ_{PS} . Accordingly, particles can not only cross the width of a gyroradius with each collision but also drift the width of the orbit displacement between collisions. The maximum drift is reached if the time between collisions is larger than the duration of one full poloidal turn, the transit time, $\tau_{\text{tr}}/\tau_{ei} < 1$. In this case, the displacement can be taken as the new step size of the random walk process. It is given by $\delta_{\text{PS}} \approx \frac{\rho_{Te}}{\nu}$, where ν is the rational transform. The diffusion coefficient is therefore

$$D_{\text{PS}} = \frac{\delta_{\text{PS}}^2}{2\tau_{ei}} = \frac{1}{\nu^2} D_{\text{cl}}. \quad (2.7)$$

If the collision time is smaller than the transit time, $\tau_{\text{tr}}/\tau_{ei} > 1$, particles can not drift the whole displacement between collisions and the step width depends on the collision time,

$$D_{\text{PS}} = \frac{(v_{\text{D}}\tau_{ei})^2}{2\tau_{ei}} \propto \tau_{ei} = \frac{1}{\nu}, \quad (2.8)$$

where v_{D} is the drift velocity and ν is the collision frequency.

Banana regime

The increasing magnetic field strength which particles experience when going from out- to inboard side of the torus additionally acts as a magnetic mirror for some particles. They bounce between two points of strong magnetic field and are trapped in closed orbits within the torus which look like bananas. The radial width of a banana orbit, $\delta_{\text{ba}} \approx \delta_{\text{PS}}/\sqrt{\epsilon}$, is the appropriate step size for the random walk transport of these particles. It is even larger than the Pfirsch-Schlüter displacement since the inverse aspect ratio, the ratio of the minor radius of the flux surface and the major radius of the magnetic axis, $\epsilon = r/R_0$, is much smaller than 1 in most toroidal devices. The step time of the random walk process is the effective collision time, $\tau_{\text{eff}} \approx \tau_{ei}\epsilon$, which accounts for the conversion to a transit particle. Finally, only a fraction, $\sqrt{\epsilon}$, of the particles is trapped and the diffusion coefficient is therefore

$$D_{\text{ba}} = \sqrt{\epsilon} \frac{\delta_{\text{ba}}^2}{2\tau_{\text{eff}}} = \frac{1}{\epsilon^{3/2}} D_{\text{PS}} = \frac{1}{\epsilon^{3/2}\nu^2} D_{\text{cl}}. \quad (2.9)$$

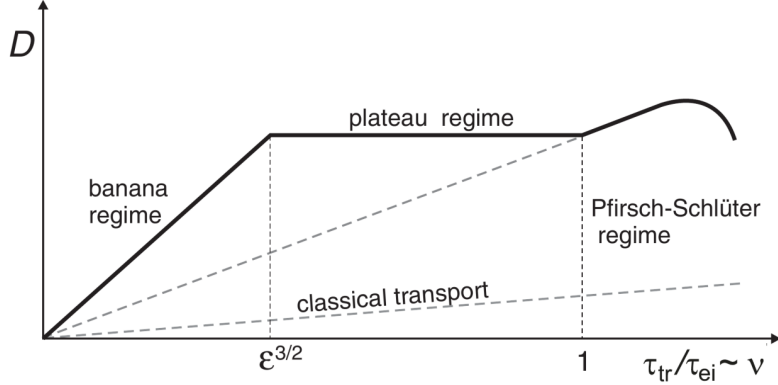


Figure 2.3: Neoclassical diffusion coefficient over collision frequency with different transport regimes in tokamaks. Modified from [36].

Similarly to the Pfirsch-Schlüter transport, the transport due to trapped particles only works as described, if the particles have enough time between collision to fulfil an entire banana orbit, $\tau_{\text{eff}} > \tau_{\text{ba}} = \tau_{\text{tr}}/\sqrt{\epsilon}$. Since this translates to $\tau_{\text{tr}}/\tau_{ei} < \epsilon^{3/2}$, it is separate from the collision regime of the Pfirsch-Schlüter transport. Figure 2.3 illustrates the different NC transport regimes in a typical tokamak. At very low collision frequency, the transport due to trapped particles dominates until the collisions prevent full banana orbits at $\tau_{\text{tr}}/\tau_{ei} > \epsilon^{3/2}$. The step width and thus the diffusion coefficient decreases, until the Pfirsch-Schlüter transport becomes dominant. In the plateau regime in between the collisionless banana regime and the collisional Pfirsch-Schlüter regime, $\epsilon^{3/2} < \tau_{\text{tr}}/\tau_{ei} < 1$, the diffusion coefficient is approximated as

$$D_{\text{pl}} \approx \frac{1}{\nu^2} \frac{\rho_{Le}^2}{2\tau_{\text{tr}}}. \quad (2.10)$$

For even larger collision frequencies, the diffusion coefficient changes to a $1/\nu$ -dependency, as described above.

Additional collisionless transport in stellarator

The classical stellarator geometry has local magnetic wells characterised by $\delta B/B \sim \epsilon_h$ [8]. As a consequence, particles can not only be toroidally

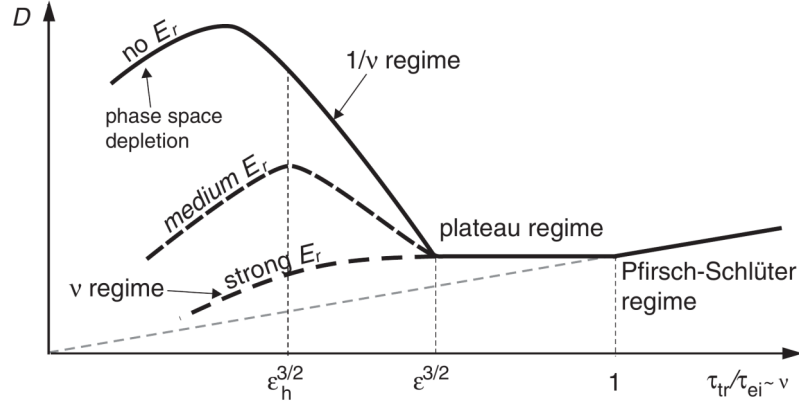


Figure 2.4: Neoclassical diffusion coefficient over collision frequency with different transport regimes in stellarators. The stellarator specific $1/\nu$ -regime at low collisionality is altered by a radial electric field. Modified from [36].

trapped between the reflection points on the inboard side of the torus, but also in the local well, which helically winds around the torus, i. e. *helically trapped*. In classical stellarator geometry, helically trapped particles continuously drift outward and are not confined, leading to large additional particle losses in the collisionless regime. This type of transport is not diffusive but actually inhibited by collisions, which de-trap particles into confined passing orbits before they are lost. The effective collision frequency for helically trapped particles can be determined analogously to the toroidally trapped ones by replacing $\epsilon \rightarrow \epsilon_h$, such that $\tau_{\text{eff}} = \tau_{ei}\epsilon_h$. The random walk step length is given similarly to the collisional Pfirsch-Schlüter case by $\delta_h = v_D\tau_{\text{eff}}$, which leads to the same $1/\nu$ -dependency of the diffusion coefficient,

$$D_{1/\nu} = \sqrt{\epsilon_h} \frac{(v_D\tau_{\text{eff}})^2}{2\tau_{\text{eff}}} \propto \epsilon_h^{3/2} \frac{1}{\nu}. \quad (2.11)$$

Figure 2.4 shows the qualitative change between transport regimes in a stellarator. Approaching the collisionless limit, the transport is reduced since helically trapped particles are lost faster than passing particles are helically trapped by collisions. This leaves a gap in the phase space distribution and is hence called phase space depletion. The $1/\nu$ -regime poses a huge problem for

stellarator reactor confinement. Reactors aim to operate at low collisionality, but the unfavourable temperature scaling, $D_{1/\nu} \propto T_e^{7/2}$, impedes reaching fusion relevant temperatures for classical stellarators. Therefore, there have been efforts to optimise the geometry of the magnetic field such that the radial component of the bounce-averaged drift is reduced and an effective parameter, $\epsilon_{\text{eff}} \ll \epsilon_{\text{h}}$, is used in equation (2.11) [8]. The $1/\nu$ -regime diffusion is also less severe in the presence of a radial electric field. The corresponding poloidal $\mathbf{E} \times \mathbf{B}$ drift bends the orbit of helically trapped particles poloidally, which increases the loss time.

Ambipolar electric field

The diffusion coefficient for ions is generally much larger than for electrons [8]. In order to maintain ambipolarity of the particle fluxes, $Z_i \Gamma_i = \Gamma_e$, a self-consistent radial electric field is established, which compensates the difference [37, 38]. The local diffusive particle flux density is then given by [39]

$$\Gamma_\alpha^{\text{NC}} = -n_\alpha D_\alpha \left(\frac{n'_\alpha}{n_\alpha} - \frac{q_\alpha E_r}{T_\alpha} \right) \quad (2.12)$$

where $\alpha = e, i$, Z denotes the particle species (electrons, ions, impurities) and q_α the particle charge. If the ambipolar electric field is strong enough, the orbit of helically trapped ions is poloidally closed again due to the $\mathbf{E} \times \mathbf{B}$ drift. In this case, the diffusion coefficient has a $\sqrt{\nu}$ -dependency [8],

$$D_{\sqrt{\nu}} \sim \frac{v_D^2 \sqrt{\nu}}{\Omega_E^{3/2}}, \quad (2.13)$$

where $\Omega_E \sim E_r/rB$ is the $\mathbf{E} \times \mathbf{B}$ drift frequency. At very low collision frequency, ions experience collisionless de-trapping and the diffusion coefficient is again proportional to ν . In typical stellarator operation with $T_e \approx T_i$, the electrons are in the $1/\nu$ -regime and the ions in the $\sqrt{\nu}$ -regime, with a negative radial electric field compensating a stronger ion diffusion [8]. This situation is called *ion root*. Due to the strong temperature dependence in the $1/\nu$ -regime, $D_e \propto T_e^{7/2}$, the electron diffusion increases strongly for local electron heating ($T_e \gg T_i$) and a second stable solution to the ambipolarity condition with a positive E_r arises, which is called *electron root* [8, 38].

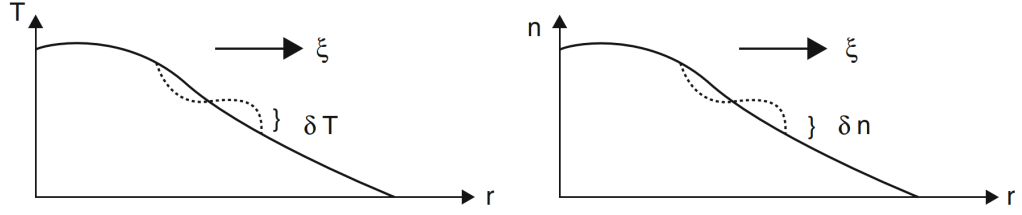


Figure 2.5: Schematic picture of the mixing length approach. In presence of a background gradient, the perturbation is determined by the mixing length, ξ . Taken from [40].

2.2.3 Turbulent transport

Mixing length approach

Transport in fluid turbulence was first explained by Joseph Boussinesq by the *mixing length* approach, which assumes a random walk process for fluid elements due to convection by eddies [3]. The characteristic step length is the mixing length, $\xi = \tilde{u}\tau_{\text{corr}}$, where \tilde{u} is the velocity at which the fluid element is convected and τ_{corr} is the correlation time for which the eddy persists. In the presence of a background gradient, the perturbation of a quantity, f , is then determined by

$$\tilde{f} = -\xi\nabla f, \quad (2.14)$$

which is illustrated for temperature ($\tilde{f} = \delta T$) and density ($\tilde{f} = \delta n$) in figure 2.5. The decomposition of a turbulent quantity into a stationary (time averaged) and a fluctuating part, $f = f_0 + \tilde{f}$, is called Reynolds decomposition [41] and is the basis for most statistical approaches to turbulence. The corresponding transport due to convection by eddies can then be estimated by

$$F = \langle \tilde{f}\tilde{u} \rangle \approx \tilde{u}^2\tau_{\text{corr}}\nabla f \approx D\nabla f, \quad (2.15)$$

which gives the same result as the random walk Ansatz with $D = \frac{\xi^2}{\tau_{\text{corr}}} = \tilde{u}^2\tau_{\text{corr}}$.

Transport in electrostatic plasma turbulence

In electrostatic plasma turbulence, particles and heat are transported by the local time-varying $\mathbf{E} \times \mathbf{B}$ flow, $\tilde{\mathbf{v}}_E = \mathbf{B} \times \nabla \tilde{\phi} / B^2$, due to a microscopic fluctuation of the electric potential, $\tilde{\phi}$. The particle and heat transport through a flux surface, S , is given by [14, 42]

$$\Gamma_\alpha = \frac{1}{S} \int_S n_\alpha \tilde{\mathbf{v}}_E \cdot d\mathbf{a} = -D_\alpha^{\text{eff}} \frac{dn_\alpha}{dr}, \quad (2.16)$$

$$q_\alpha = \frac{1}{S} \int_S n_\alpha T_\alpha \tilde{\mathbf{v}}_E \cdot d\mathbf{a} = -\chi_\alpha^{\text{eff}} \frac{dT_\alpha}{dr}, \quad (2.17)$$

where $\alpha = i, e$ denotes the particle species, \mathbf{a} is the unit vector normal to the flux surface and r is the radial coordinate. The effective diffusivities provide information on the basic mechanisms which drive turbulence in the plasma. The perturbative $\mathbf{E} \times \mathbf{B}$ flow acts equally on ions and electrons, which makes the turbulent particle transport inherently ambipolar. There may be different turbulent heat transport for electrons and ions, however, if $T_e \neq T_i$. Assuming radially symmetric wave-like potential fluctuation, the $\mathbf{E} \times \mathbf{B}$ flow goes in both radial directions and vanishes on a flux surface average, $\int_S \tilde{\mathbf{v}}_E \cdot d\mathbf{a} \approx 0$. The stationary parts of density and temperature are constant on the flux surface and thus do not contribute to turbulent transport. Turbulent transport therefore only depends on fluctuating quantities,

$$\Gamma_\alpha = \langle \tilde{n}_\alpha \tilde{v}_E \rangle, \quad q_\alpha = \langle \tilde{n}_\alpha \tilde{T}_\alpha \tilde{v}_E \rangle, \quad (2.18)$$

where $\langle \dots \rangle$ denotes the flux surface average. Two aspects therefore largely determine the radial transport due to fluctuations: first, the amplitude of \tilde{n} , \tilde{T} and $\tilde{\phi}$, which is set by the saturation level of the turbulence. Secondly, the cross-phase between these quantities, which mostly depends on the instability causing the fluctuations. For the example of particle transport, one obtains [36]

$$\Gamma_\alpha \propto \frac{k_\theta}{B} |\tilde{n}_\alpha| |\tilde{\phi}| \sin(\varphi_{n\phi}), \quad (2.19)$$

where k_θ is the poloidal wavenumber. Maximum transport occurs at a cross-phase between density and potential fluctuation of $\varphi_{n\phi} = \pi/2$. If the

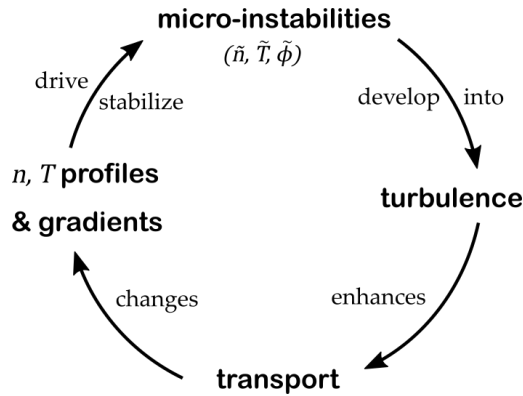


Figure 2.6: Turbulence interaction in fusion plasmas.

perturbations are perfectly in phase, no net transport occurs. Similar arguments can be made for the heat transport, where the phase between the potential and temperature fluctuations predominantly determines the transport level. Since the phase between temperature and density fluctuations can vary depending on the micro-instability, heat and particle transport are rather decoupled, which is unique to turbulent transport.

In summary, turbulent transport in fusion plasmas can be described by effective diffusion coefficients (cf. equation (2.16)). They are determined by fluctuation amplitude and cross-phase of density, temperature and electrostatic potential, which arise from electrostatic micro-instabilities. Due to their crucial role for confinement, these micro-instabilities are subject of intensive research and also the main topic of chapter 3. They are generally driven or stabilised by the radial gradients of density and temperature. Even though the understanding of the fundamental mechanism of plasma turbulence has progressed, a complete self-consistent picture of turbulent transport in a hot fusion plasma is still very challenging. Plasma turbulence acts on itself by affecting the radial profiles via transport, which greatly influences the growth of micro-instabilities. This results in a strongly nonlinear feedback loop, as illustrated in figure 2.6.

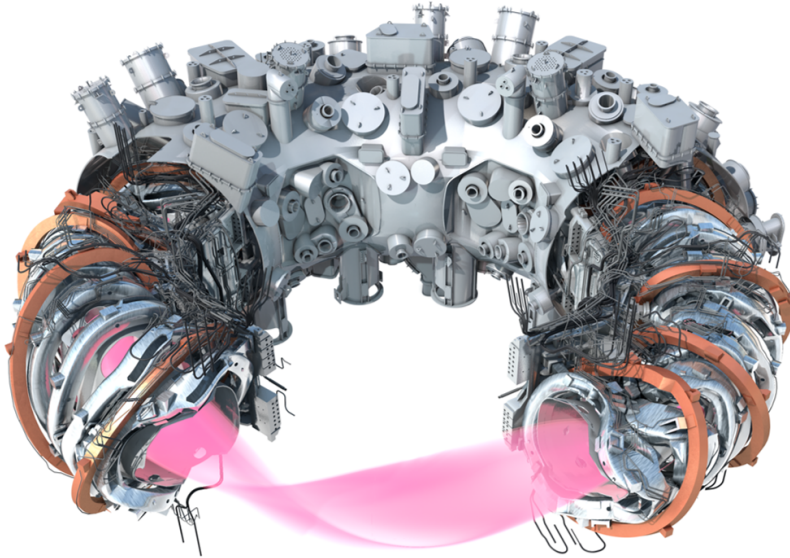


Figure 2.7: The Wendelstein 7-X stellarator. The plasma (pink) is generated inside the inner vacuum vessel, which is surrounded by the 50 non-planar (silver-coloured) and 20 planar (copper-coloured) superconducting magnetic field coils. The outer vacuum vessel closes off the cryostat which encloses the magnetic coils.

2.3 Wendelstein 7-X

The Wendelstein 7-X stellarator is operated at the Max-Planck Institute for Plasma Physics in Greifswald. 50 superconducting non-planar modular coils generate the magnetic field, which is optimised for low NC transport. 20 additional superconducting planar coils are used to vary the rotational transform. The coil system was designed to be precise and flexible, which was achieved albeit major technical challenges during construction [18, 43–45]. Figure 2.7 shows a schematic of the device including the plasma, the coils, the support structure of the coils and the inner and outer vacuum vessel. The main technical parameters are summarised in table 2.1.

The goal of the W7-X project is the demonstration of the feasibility of stellarators for fusion energy in several steps [46]. In particular, the successful construction of the complex engineering design [18, 43, 44] as well as the successful optimisation towards low NC transport [17] have been

Table 2.1: Technical device parameters of W7-X. B_0 is the magnetic field strength on axis and ι is the rotational transform at the edge of the plasma, which can be varied between the given values.

parameter	value
minor radius	0.5 m
major radius	5.5 m
plasma volume	30 m ³
B_0	2.5 T
ι	5/6 to 5/4

demonstrated. In upcoming experiments with fully water cooled plasma facing components, continuous plasma operation for up to 30 min will be attempted. In the long term, W7-X aims to achieve high plasma β , which is only possible with performance optimisation and requires knowledge of the turbulent transport mechanisms.

W7-X has a field periodicity of five, meaning it consists of five identical toroidally arranged modules, each consisting of two mirrored half-modules. Figure 2.8 depicts a top view of W7-X with three cross sections, which alternate along the torus: the triangular, an intermediate, and the bean shaped cross section. They exhibit largely different shear, curvature and compression of the magnetic flux surfaces, which is a major difference to the axisymmetric tokamak. At high β , contours of constant B are poloidally closed, but not toroidally. Particles which are trapped in the toroidal mirrors precess around the torus in a roughly poloidal direction without leaving the confined plasma, i.e. the bounce averaged radial drift vanishes [15, 48]. This quality is referred to as *quasi-isodynamicity* and prevents the large collisionless losses, which occur in classical stellarators [49]. By varying the coil current ratios, different magnetic field geometry can be achieved with different mirror ratios and rotational transform profiles [50]. In previous experiment campaigns, there have been designated configurations within the accessible parameter space. The W7-X *standard* configuration is defined by equal current in the five individual modular coil types and no current in the planar coils. Increasing or decreasing the toroidal mirror ratio yields the *high* and *low mirror* configuration (although the latter was not common in past experiments). Using the planar coils the rotational transform is increased or decreased. The rotational transform at the last closed flux

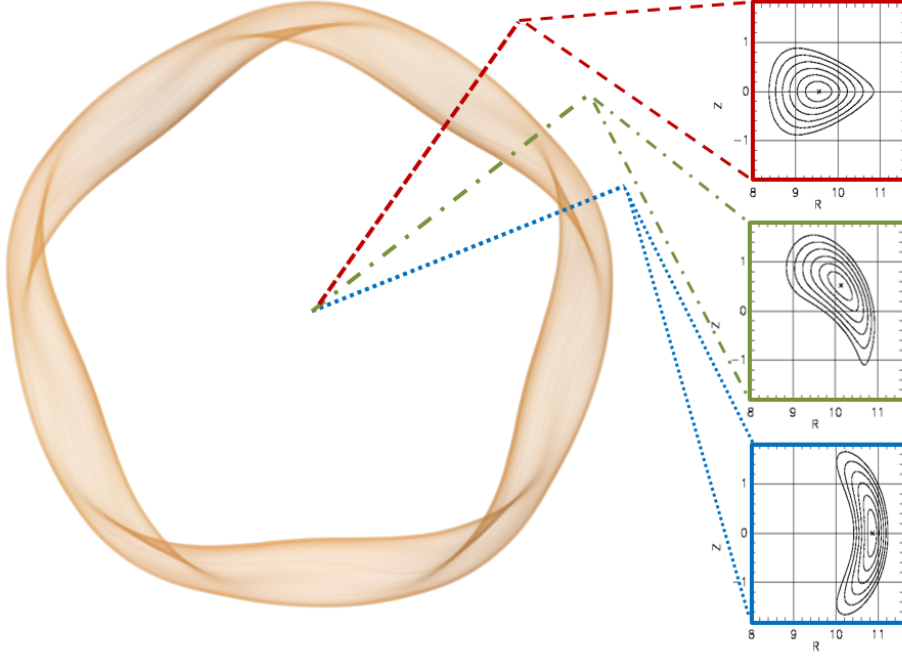


Figure 2.8: Top view of W7-X showing the five-fold symmetry of the magnetic field. Three cross sections are depicted, which alternated along the torus. The upper panel shows the triangular cross section, the lower panel shows the bean shaped cross section. Taken from PERSEO [47].

surface (LCFS), ι_a , is set to a low rational leading to resonances forming intrinsic island chains in the scrape-off layer (SOL) of W7-X, which are important for the heat transport to the island divertor [51]. The standard and high mirror configurations have $\iota_a = 5/5$, forming five independent islands. The magnetic configuration with increased rotational transform and $\iota_a = 5/4$ is called *high iota* configuration and analogously there exists the *low iota* configuration with $\iota_a = 5/6$. Figure 2.9 shows the radial profile of ι for the four different configurations. r_{eff} is the effective minor radius of the plasma, which in the context of W7-X is defined via the toroidally averaged poloidal cross-sectional area, $\langle A \rangle$, as $r_{\text{eff}} = \sqrt{\langle A \rangle / \pi}$. The minor radius at the LCFS is traditionally labelled a , such that $r_{\text{eff}}/a = 0$ corresponds to the magnetic axis and $r_{\text{eff}}/a = 1$ to the LCFS. The ι -profiles are flat in contrast

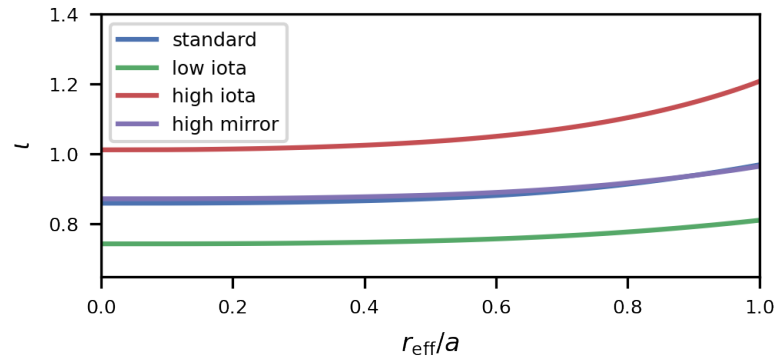


Figure 2.9: Radial profiles of the rotational transform, ι , of different W7-X magnetic configurations.

to typical tokamaks and shifted up and down between configurations without considerably changing the form of the profile.

W7-X is equipped with electron cyclotron resonance heating (ECRH) and neutral beam injection (NBI), providing up to 8.5 MW and 3.5 MW of heating power, respectively, in the latest experiment phase [18]. These systems are continuously being upgraded and an additional ion cyclotron radiation heating (ICRH) system has been installed for future experiments.

3

Plasma Turbulence

The basic features of plasma turbulence have already been introduced in the previous chapters: the vorticity is generally aligned with the magnetic field, which evokes similarities to 2-dimensional fluid turbulence. The plasma is convected by $\mathbf{E} \times \mathbf{B}$ flow due to fluctuating electric potential, which arises due to electrostatic micro-instabilities. The resulting fluctuations of density, temperature and potential cause, depending on their cross-phase, strong particle and heat transport.

In this chapter, physical mechanisms and mathematical descriptions are introduced in more detail. Gyrokinetic theory, which is used for the treatment and simulation of turbulent micro-instabilities, is introduced in section 3.1. In section 3.2, the physical mechanisms and basic types of electrostatic micro-instabilities are described. These micro-instabilities are discussed in the context of W7-X in section 3.3. Expectations for the experiment on the basis of linear gyrokinetic simulations are formulated. Finally, in section 3.4, the phenomenology and generation of ZFs in plasma turbulence and in particular in stellarators is described.

Before going on to the details, the principle boundaries of electrostatic micro-turbulence are briefly discussed. The typical size of the turbulent fluctuations, which fill the whole plasma volume, is much smaller than the machine size, i. e. they are microscopic. The relative and absolute scale of turbulence plays an important role for transport as well as for its mathematical treatment: it is generally assumed that the relevant fluctuations are much smaller and faster than system scales or confinement times. On the

other hand, they are much slower than electron plasma waves and the gyromotion of ions and electrons. These effects are therefore usually averaged over in the treatment of micro-turbulence, as in gyrokinetic theory. Plasma turbulence can be not only electrostatic but also electromagnetic, which involves fluctuations of the magnetic field, $\tilde{\mathbf{B}}$. This requires a minimum ratio of thermal plasma pressure to magnetic pressure, $\beta = nT/(B^2/2\mu_0)$. So far, W7-X operated at low values of β , such that the turbulence is assumed to be electrostatic.

3.1 Gyrokinetic description

The study of electrostatic micro-instabilities improves the understanding of turbulence drive and therefore how turbulence can be mitigated. The treatment of the plasma as a fluid is generally not sufficient for this. In particular, wave-particle interactions, which are crucial for some instabilities, can not be described in a fluid picture but require a full kinetic treatment. Modern studies of plasma turbulence therefore heavily rely on the *gyrokinetic* approach. The basic principle of gyrokinetics is the reduction of 6-dimensional phase space to five dimensions by averaging over the gyromotion of the particles, which was first introduced in 1968 by RUTHERFORD & FRIEMAN [52] as well as TAYLOR & HASTIE [53]. For a detailed review on the foundations of nonlinear gyrokinetic theory, see BRIZARD & HAHM [54].

3.1.1 Gyrokinetic equation

The basic steps of the gyrokinetic derivation are sketched out in this section and the reader is referred to existing literature for more details [54–57]. The starting point is the **Vlasov equation**, the fundamental equation of kinetic theory for collisionless plasmas [58],

$$\frac{\partial f}{\partial t} + \mathbf{v} \cdot \nabla_{\mathbf{r}} f + \frac{q}{m} (\mathbf{E} + \mathbf{v} \times \mathbf{B}) \cdot \nabla_{\mathbf{v}} f = 0, \quad (3.1)$$

where $f(\mathbf{r}, \mathbf{v}, t)$ is the distribution function in phase space for either particle species. It is analogous to the collisionless Boltzmann-equation with a Lorentz force field. In general, Coulomb collisions can not be ignored and are included via the Fokker-Planck collision operator, which statistically

describes the long-range Coulomb collisions [58]. Including the operator on the right hand side of equation (3.1) yields the **Fokker-Planck equation**. For the discussion of basic micro-instabilities, the collisionless equation is sufficient.

The first step towards the gyrokinetic equation is a change of variables to guiding-centre coordinates known as the **Catto transformation** [55, 56]:

$$(\mathbf{r}, \mathbf{v}, t) \longrightarrow (\mathbf{R}, \mu, \mathcal{E}, \vartheta, t), \quad (3.2)$$

with guiding centre position, $\mathbf{R}(\mathbf{r}, \mathbf{v}) = \mathbf{r} + \mathbf{v} \times \hat{\mathbf{b}}/\Omega$, where $\hat{\mathbf{b}} = \mathbf{B}/B$ is the unit vector in the magnetic field direction and $\Omega = qB/m$ is the gyration frequency. The particle velocity is decomposed as

$$\mathbf{v} = v_{\parallel} \hat{\mathbf{b}} + v_{\perp} (\hat{\mathbf{e}}_1 \cos \vartheta + \hat{\mathbf{e}}_2 \sin \vartheta), \quad (3.3)$$

where the first term describes the velocity of the guiding centre in the magnetic field direction, and the second term the velocity of the gyration motion, where $\hat{\mathbf{e}}_1$ and $\hat{\mathbf{e}}_2$ form an orthogonal base with $\hat{\mathbf{b}}$. The latter is expressed by the magnetic moment, $\mu(\mathbf{r}, \mathbf{v}) = mv_{\perp}^2/2B$, and the gyrophase, ϑ . Finally, the total energy is used, $\mathcal{E} = v^2/2 + (q/m)\phi_0(\mathbf{r})$, where ϕ_0 is the electric potential. This leads to the general form of the gyrokinetic equation,

$$\frac{\partial f}{\partial t} + \dot{\mathbf{R}} \frac{\partial f}{\partial \mathbf{R}} + \dot{\mu} \frac{\partial f}{\partial \mu} + \dot{\mathcal{E}} \frac{\partial f}{\partial \mathcal{E}} + \dot{\vartheta} \frac{\partial f}{\partial \vartheta} = 0, \quad (3.4)$$

with the respective explicit expressions for $\dot{\mathbf{R}}$, $\dot{\mu}$, $\dot{\mathcal{E}}$, and $\dot{\vartheta}$.

Next, the **gyro-average** is applied to the equation, which averages any quantity, Q , over one turn of the gyromotion and thus removes the dependency on ϑ [55],

$$\langle Q \rangle(\mathbf{R}, \mu, \mathcal{E}, t) = \frac{1}{2\pi} \int_0^{2\pi} Q(\mathbf{R}, \mu, \mathcal{E}, \vartheta, t) d\vartheta, \quad (3.5)$$

where all variables except t and ϑ are fixed. Applying the gyro-average to the Fokker-Planck equation yields the drift kinetic equation, which is used to find equilibrium solutions and resolve large scale effects [7]. The guiding centre drifts arise through

$$\langle \dot{\mathbf{R}} \rangle = v_{\parallel} \hat{\mathbf{b}} + \mathbf{v}_E + \mathbf{v}_d, \quad (3.6)$$

with the $\mathbf{E} \times \mathbf{B}$ and magnetic drift velocities,

$$\mathbf{v}_E = \frac{\hat{\mathbf{b}} \times \nabla \phi_0}{B}; \quad \mathbf{v}_d = \frac{\hat{\mathbf{b}}}{\Omega} \times \left(\frac{v_\perp^2}{2} \nabla \ln B + v_\parallel^2 \boldsymbol{\kappa} \right). \quad (3.7)$$

Here, the magnetic curvature, $\boldsymbol{\kappa} = \hat{\mathbf{b}} \cdot \nabla \hat{\mathbf{b}}$, is introduced.

The gyrokinetic approach aims to resolve turbulent fluctuations with a length scale, ρ , and typical frequency, ω , which follow the **gyrokinetic ordering** of the fundamental expansion parameter [56, 57],

$$\epsilon = \frac{\rho}{L} \sim \frac{q\phi}{T} \sim \frac{\omega}{\Omega} \ll 1, \quad (3.8)$$

where L is the system length scale and ϕ is the fluctuating electric potential. A detailed derivation of gyrokinetic theory based on scale separation was done by PLUNK [56]. The distribution function is expanded as $f = f_0 + f_1 + \dots$, where f_0 is chosen to be a Maxwellian equilibrium solution. The first order perturbation, f_1 , is commonly further decomposed into $f_1 = -\frac{q\phi}{T} f_0 + g$. The first term is the adiabatic response of the equilibrium distribution to the potential perturbation, while g is the non-adiabatic part of the distribution function. The **gyrokinetic equation** to first order of ϵ , is then given by [7, 57]

$$\frac{\partial g}{\partial t} + (v_\parallel \hat{\mathbf{b}} + \mathbf{v}_E + \mathbf{v}_d) \cdot \nabla (f_0 + g) = \frac{qf_0}{T} \frac{\partial \langle \phi \rangle}{\partial t}. \quad (3.9)$$

The $\mathbf{E} \times \mathbf{B}$ drift is now due to the perturbation, $\mathbf{v}_E = (\hat{\mathbf{b}} \times \nabla \langle \phi \rangle) / B$, while \mathbf{v}_d is still due to the background magnetic field. The nonlinearity which leads to turbulence is therefore contained in \mathbf{v}_E . For the linear stability analysis of electrostatic micro-instabilities, this term is neglected.

3.1.2 Gyrokinetic simulation

Numerical plasma turbulence simulation typically solve the gyrokinetic equation for ions and electrons. The exact implementation varies between codes, as some codes simulate the full distribution function, f , while other so-called δf -codes only solve the perturbed part. Despite being expensive, gyrokinetic simulations are indispensable for progress in plasma turbulence

understanding. Both the characterisation of specific phenomena as well as the interpretation of experimental observation rely on simulations, since a comparison to analytical theory is often limited by the complexity of the problem.

Depending on the application and computational resources, different types of simulations are deployed: if wave-particle interactions are negligible for the secondary particle species, it is common to assume a purely adiabatic response (e. g. $g_e = 0$) instead of solving the kinetic equation for both in order to save computation time. Linear simulations are used to study the stability of micro-instabilities and are less computationally expensive than nonlinear simulations, which are required for an analysis of fluctuation amplitudes, mode structures and transport levels. For local turbulence effects, flux tube simulations are used, which are limited to a finite size tube around a specific magnetic field line for (usually) one full poloidal turn. Flux surface simulations contain the entire flux surface and can resolve the spatial distribution and spreading of turbulence over the surface. Finally, there are global simulations which include a large fraction of the plasma volume. Fully 3-dimensional global nonlinear gyrokinetic simulations provide the most accurate approach, but they are still at an early stage of their development and prohibitively expensive. A code developed at IPP is the gyrokinetic electromagnetic numerical experiment (GENE) code [59], which was further developed for global simulations of arbitrary magnetic geometries into the 3-dimensional expansion of GENE (GENE-3D) [60, 61].

3.1.3 Analytic gyrokinetics

For analytical studies of instabilities, it is common to additionally assume the **drift wave ordering**, in which the perturbation is stretched out along the magnetic field direction, $k_{\parallel}L \sim k_{\perp}\rho_i \sim 1$ (cf. section 3.2.1). Therefore, the eikonal expression for ϕ and g is used [24],

$$\phi(\mathbf{r}, t) = \hat{\phi}(\mathbf{r}, \omega) \exp i(S(r) - \omega t), \quad (3.10)$$

$$g(\mathbf{r}, t) = \hat{g}(\mathbf{r}, \omega) \exp i(S(r) - \omega t), \quad (3.11)$$

where $\hat{\phi}$ and \hat{g} vary slowly in every direction and the fast perpendicular oscillatory behaviour is contained in $\exp(iS)$. S is chosen as [24]

$$\nabla S \equiv \mathbf{k}_{\perp} = k_{\alpha} \nabla \alpha + k_{\psi} \nabla \psi, \quad (3.12)$$

where ψ is the toroidal magnetic flux and α is the Clebsch angle, such that $\mathbf{B} = \nabla\psi \times \nabla\alpha$ [7]. The gyro-average of the eikonal expression yields a first order Bessel function, $J_0\left(\frac{k_\perp v_\perp}{\Omega}\right)$, such that [57]

$$\frac{\partial\langle\phi\rangle}{\partial t} = -i\omega J_0\phi, \quad (3.13)$$

$$\nabla\langle\phi\rangle \simeq i\mathbf{k}_\perp J_0\phi. \quad (3.14)$$

The final form of the gyrokinetic equation, which is used in analytical studies, is then [22, 24, 57]

$$iv_\parallel \nabla_\parallel g + (\omega - \omega_d)g = \frac{q\phi}{T} J_0(\omega - \omega_*^T) f_0, \quad (3.15)$$

where the diamagnetic frequency and magnetic frequency have been introduced as

$$\omega_*^T = \omega_* \left[1 + \eta \left(\frac{v^2}{v_\perp^2} + \frac{3}{2} \right) \right], \quad \omega_d = \mathbf{k}_\perp \cdot \mathbf{v}_d,$$

with

$$\omega_* = \frac{T k_\alpha}{q} \frac{d \ln n}{d\psi}, \quad \eta = \frac{d \ln T}{d \ln n}.$$

For local analyses, \mathbf{k}_\perp can be assumed to be constant along the magnetic field direction and the diamagnetic frequency can be rewritten in the more common form [24],

$$\omega_* = \frac{k_y \rho_L}{L_n \sqrt{2}} v_T = \frac{T}{qB} \frac{k_y}{L_n}, \quad (3.16)$$

where $v_T = \sqrt{2T/m}$ is the thermal velocity and $k_y = k_\alpha B_0 (dr/d\psi) / \sqrt{2}$ is the binormal wavenumber. In the following, the local definitions are used with $k_\alpha \equiv k_y$. L_n is the density gradient length scale, which is defined for a general quantity X as

$$L_X = - \left(\frac{\partial \ln X}{\partial r} \right)^{-1}. \quad (3.17)$$

3.1.4 Quasineutrality and dispersion relation

The gyrokinetic equation (3.15) for each particle species together form a system of equations, which are coupled through the potential, ϕ . This system is closed by the quasineutrality condition [22],

$$\sum_a q_a \int d^3\mathbf{v} J_0 g_a = \sum_a \frac{n_a q_a^2}{T_a} \phi, \quad (3.18)$$

where a denotes the particle species. Assuming adiabatic electrons ($g_e = 0$) and $Zn_i = n_e$ with $Z = q_i/q_e$, the quasineutrality condition simplifies to

$$\int d^3\mathbf{v} J_0 g_i = n_i(1 + \tau)\varphi, \quad (3.19)$$

where $\varphi = q_i\phi/T_i$ is the normalised electrostatic potential and $\tau = T_i/(ZT_e)$ is the temperature ratio.

The goal of analytic studies of micro-instabilities is to derive a dispersion relation, $\omega(k)$, of the respective instability by combining the gyrokinetic equation with the quasineutrality condition. In general, the dispersion relation is complex, $\omega \approx \omega_r + i\gamma$, where the real part, ω_r , is the frequency and the imaginary part, γ , is the growth rate of the instability.

3.2 Electrostatic micro-instabilities

Most of the turbulent transport in tokamaks and stellarators is related to electrostatic micro-instabilities. The fundamental physical mechanisms for these instabilities are the drift wave and interchange instability, which are described in section 3.2.1. They were originally referred to as universal instabilities since they are intrinsic to inhomogeneous plasmas and toroidal magnetic fields. HASEGAWA & MIMA [62] first described experimentally observed strong plasma turbulence with a model equation based on the drift wave mechanism. In contrast to earlier models, the ion polarisation drift provides the nonlinearity instead of the $\mathbf{E} \times \mathbf{B}$ drift. The advantage is the compressibility of the polarisation drift, which is necessary to explain broad frequency spectra [63]. While the Hasegawa-Mima model describes the nonlinear evolution of drift waves well, it is linearly stable because it lacks a mechanism for non-adiabatic electron response, which is necessary to drive the drift wave instability. For this purpose, HASEGAWA & WAKATANI [64] introduced electron inertia through electron resistivity into the model and later included magnetic curvature [65], which drives global hydrodynamic instability according to the interchange mechanism. The Hasegawa-Mima and Hasegawa-Wakatani models are only mentioned for historic context; for more details see e. g. HASEGAWA & MIMA [63]. Drift wave turbulence has been investigated for decades, mostly for tokamaks as reviewed e. g. by WEILAND & ZAGORODNY [40].

In present discussions of plasma turbulence, the instabilities are distinguished by their source of free energy. The most relevant types for turbulent transport in tokamaks are the ion-temperature-gradient-driven (ITG) and electron-temperature-gradient-driven (ETG) modes, as well as the trapped-electron mode (TEM), which are discussed in sections 3.2.2 to 3.2.4. These modes can take various forms and should be understood as a combination of both the drift wave and the interchange instability (and often other types). They are distinguishable by their spatial scale and frequency, with ITG modes having the largest scale, closely followed by TEMs and ETG modes on much smaller scales. Figure 3.1 shows typical linear growth rate spectra of each mode. ITG modes and TEMs mostly overlap in k_{\perp} -space, while ETG modes also appear at these scales but peak at much larger k_{\perp} . According to the mixing length model, larger scales cause more turbulent transport in the presence of the same background gradient. The cross-phase

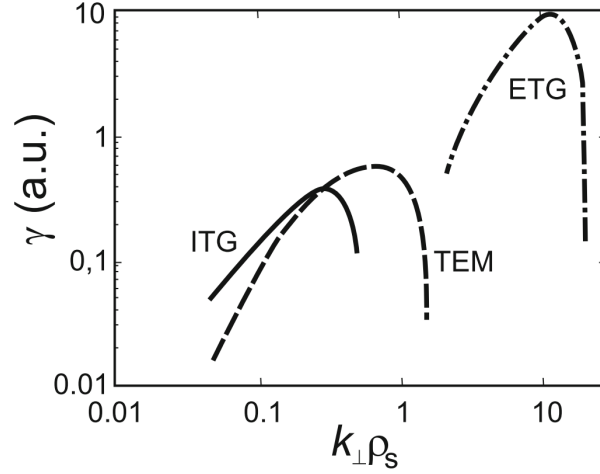


Figure 3.1: Typical micro-instability growth rate spectra in tokamaks. Taken from STROTH [35].

of density, temperature and potential as well as the self-consistent nonlinear generation of large scale structures is, however, just as important for the resulting transport level as the scale of the linear instability. A quasi-linear mixing length estimate of the effective diffusion is commonly obtained with the linear growth rate, γ , and corresponding perpendicular wavenumber, k_{\perp} , of a turbulent mode as [14],

$$D^{\text{eff}} \sim \frac{\gamma_{\text{max}}}{k_{\perp}^2}. \quad (3.20)$$

The best estimate is obtained by maximising γ/k_{\perp}^2 over k_{\perp} for a given linear growth rate spectrum [26], which helps identify transport relevant instabilities without a fully nonlinear treatment.

3.2.1 Physical mechanism

Drift waves and interchange instabilities represent two aspects of the fundamental physical mechanism of electrostatic micro-instabilities in inhomogeneous plasmas with finite pressure gradient, ∇p . The main difference is the coupling mechanism between the pressure perturbation and the electrostatic potential perturbation. Figure 3.2 shows a sketch of the principle

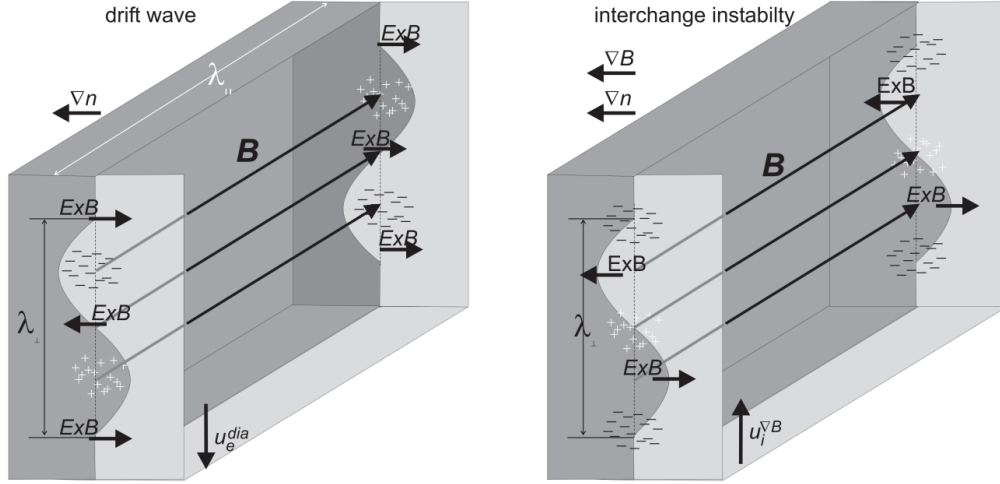


Figure 3.2: Schematic illustration of the drift wave and interchange instability mechanism. Taken from STROTH [35].

mechanisms in a simple geometry. In case of drift waves (left panel), the potential is caused by a fast parallel electron response along the magnetic field direction. In the interchange mechanism (right panel), it is caused by the charge dependent magnetic drift due to an inhomogeneity of the magnetic field in combination with the perpendicular structure of the perturbation. In both cases, the potential perturbation results in a perpendicular $\mathbf{E} \times \mathbf{B}$ drift, but the cross-phase with respect to the pressure perturbation is different. For drift waves, the potential and pressure perturbation are in phase, which leads to wave propagation, while the interchange mechanism yields a cross-phase of $\pi/2$, leading to growth of the perturbation.

There exist analogous phenomena in neutral fluids. Drift waves are analogous to Rossby waves in planetary atmospheres, which occur due to gravity ($\hat{=}$ parallel electrostatic force) and a latitudinal gradient of the Coriolis force ($\hat{=}$ radial density gradient) [66]. The interchange instability is analogous to the Rayleigh-Taylor instability in neutral fluids [67].

In toroidal configurations, the two mechanisms are not strictly separated but merely different limits. If the parallel wavelength is small compared to the system scale length, $\lambda_{\parallel} \ll R$, the variation and curvature of the magnetic field are small on the scale of the mode, such that parallel dynamics dominate. This is the drift wave limit. In the limit of long parallel wavelength, $\lambda_{\parallel} \sim R \sim$

L_B , the toroidal geometry becomes important and the interchange instability becomes relevant. In the following, the two mechanisms are explained in more detail.

Drift waves

Even though the drift wave is the limit of finite parallel wavelength, the perpendicular wavelength is much shorter $\lambda_\perp/\lambda_\parallel = k_\parallel/k_\perp \ll 1$ (cf. drift wave ordering). Since particles move freely along the magnetic field (neglecting collisions and trapping), they will compensate the parallel pressure gradient. Electrons have a much higher mobility than ions due to their lower mass and are therefore assumed to respond instantaneously (i. e. adiabatic). A charge separation will occur following the Boltzmann relation,

$$\frac{\tilde{n}}{n_0} = \frac{e\tilde{\phi}}{T_e}. \quad (3.21)$$

The electric potential, $\tilde{\phi}$, is in phase with the density perturbation and the corresponding perpendicular electric field, $\tilde{\mathbf{E}} \perp \mathbf{B}$, has a phase shift of $\pi/2$. The $\mathbf{E} \times \mathbf{B}$ drift is not charge dependent and causes a plasma advection instead of a charge separation. Due to the phase shift of $\pi/2$, the density perturbation will not grow but propagate in the electron diamagnetic direction — this is called a *drift wave*. The dispersion relation is $\omega = \omega_*$, i. e. without imaginary growth rate. In a toroidal geometry, the drift wave propagates along the flux surfaces in the electron diamagnetic direction.

As mentioned in the introduction to this section, the ion polarisation drift, which arises due to the varying electric field, $\mathbf{v}_p = \frac{m}{eB^2} \frac{d}{dt} \mathbf{E}$, needs to be included. It acts in the same direction as the $\mathbf{E} \times \mathbf{B}$ drift and leads to a correction of the dispersion relation,

$$\omega = \frac{\omega_*}{1 + (k_\alpha \rho_s)^2}, \quad (3.22)$$

where $\rho_s = c_{s,i}/\Omega_i \approx \frac{\sqrt{m_i T_e}}{ZeB}$ is the drift scale. The effect of the polarisation drift is relevant for medium to small scales, $k_\alpha \gtrsim \rho_s$.

The drift wave including the polarisation drift is still stable (cf. Hasegawa-Mima model). An instability only occurs if the electron response is not adiabatic (cf. Hasegawa-Wakatani model). The retardation of the electrons

e. g. due finite inertia causes a cross-phase between \tilde{n} and $\tilde{\phi}$. The $\mathbf{E} \times \mathbf{B}$ and polarisation drift then also lead to an increase of the perturbation amplitude.

Interchange instability

The interchange instability is the long parallel wavelength limit, $k_{\parallel} = 0$, i. e. no parallel dynamics are involved. In contrast to the drift wave, the interchange mechanism requires an inhomogeneity of the magnetic field, which causes the perpendicular charge dependent magnetic drift. The charge separation occurs due to inhomogeneous drift along the perturbation: on the flanks of the perturbation, fewer electrons arrive from the low density part as ions from the high density part and vice versa. The resulting electrostatic potential, $\tilde{\phi}$, has a cross-phase of $\pi/2$ to the density perturbation and the resulting electric field is therefore in phase with \tilde{n} , opposite to the drift wave. The $\mathbf{E} \times \mathbf{B}$ drift is therefore maximally stabilising or destabilising.

Recalling equation (3.7), the magnetic drift velocity has a contribution through ∇B and through the curvature, $\boldsymbol{\kappa} = \hat{\mathbf{b}} \cdot \nabla \hat{\mathbf{b}}$, which can be approximated for small plasma β as $\boldsymbol{\kappa} \approx \nabla \ln B$ [24]. The perturbation is unstable if the magnetic and density inhomogeneity point in the same direction, $\nabla B \parallel \nabla n$, and stable if they are anti-parallel. In toroidal configurations such as tokamaks, the inboard side is stable and the outboard side is unstable, as illustrated in figure 3.3. The different curvature regions are accordingly called *good*, or *favourable* curvature and *bad*, or *unfavourable* curvature. The growth rate can be estimated as [58]

$$\gamma = \sqrt{k_{\alpha} \frac{v_{\perp}^2/2 + v_{\parallel}^2}{L_B L_n}}, \quad (3.23)$$

where L_B and L_n are the magnetic and density gradient length scale. If L_B and L_n have the same sign, γ is real and the perturbation grows exponentially and vice versa. The interchange instabilities cause convective transport by interchanging flux tubes of different pressure, hence the name. Besides to magnetic curvature, they are also sensitive to magnetic shear, since radially interchanging flux tubes in a configuration with magnetic shear necessarily leads to field line bending, which requires energy and thus has a stabilising effect.

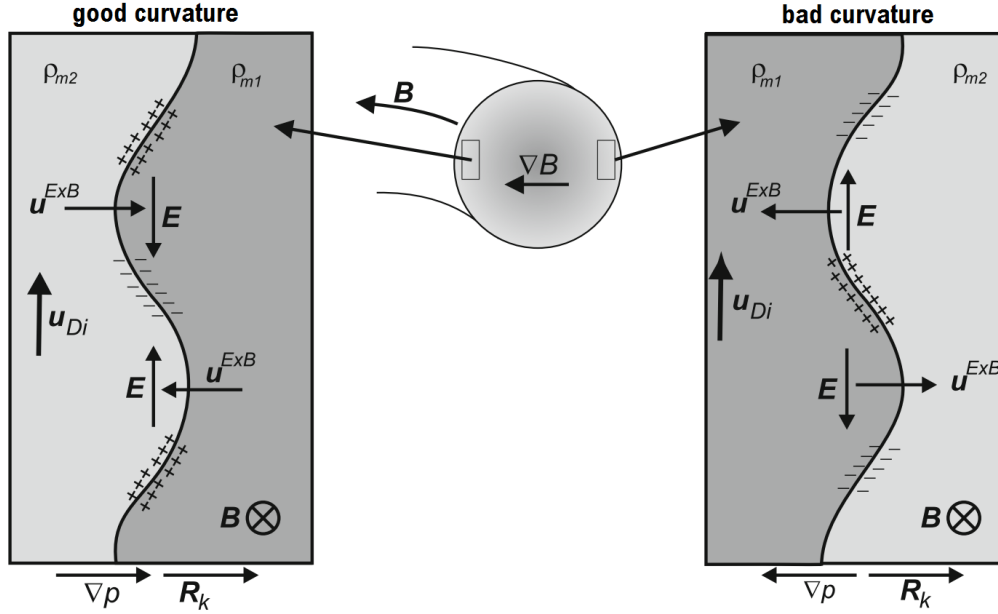


Figure 3.3: Schematic illustration of the interchange instability curvature drive mechanism. Taken from STROTH [35].

From the dispersion relations of drift wave and interchange instability it follows that there is a separation on the binormal scale but reversed with respect to the parallel scale: since the drift wave growth rate scales as $\gamma \propto k_\alpha^{-4}$ [35] and the interchange growth rate as $\gamma \propto k_\alpha^{1/2}$, drift waves are expected to dominate at long perpendicular wavelengths, while the interchange mode grows faster at small perpendicular wavelengths.

3.2.2 Ion temperature gradient mode

The ITG mode is considered the single most important instability for turbulent ion heat transport in tokamaks. One of the reasons for this are the large scale fluctuations connected to it ($k_\alpha \rho_s \leq 1$). A simple physical picture is often not useful anymore, since the mode can be driven unstable through various mechanism at the same time. The common aspect which defines the instability is that energy enters the mode through the ion temperature gradient. One generally distinguishes two types: slab and toroidal ITG mode. These types are boundary cases of the strongly driven fluid limit, where

$\eta_i \gg 1$ and $a/L_{T_i} \gg 1$, i. e. where the ion temperature gradient is large and exceeds the density gradient. Here, a is the minor radius and $\eta_i = L_n/L_{T_i}$. This limit is not justified in most experiment cases where resonances need to be considered [27], but it is useful for discussing qualitative differences between the two branches of this mode.

The earliest ITG instability models used the slab model [68, 69]. What is now called slab ITG mode is analogous to a temperature gradient-driven drift wave. It depends on parallel dynamics, k_{\parallel} is a free parameter with the typical ordering, $k_{\parallel}/k_{\perp} \ll 1$, and there is no influence of magnetic drifts [24]. Including the toroidal geometry and magnetic drifts later lead to the toroidal ITG mode [70, 71], which is analogous to a temperature gradient-driven interchange instability. It is the limit of long parallel wavelength, $k_{\parallel} = 0$, and the mode is destabilised by ∇T_i as well as the magnetic drift [24, 27].

Dispersion relation

The first full gyrokinetic theory for the ITG mode was formulated by ROMANELLI [72]. A kinetic treatment is especially necessary close to marginal stability, $\eta_i \approx 1$, where kinetic effects and resonances play a major role compared to the fluid effects. The complications of deriving a dispersion relation for the general case escalate quickly [27] and provide little insight into the fundamental mechanisms. Therefore, this discussion is limited to the strongly driven fluid limit ($\omega/\omega_*^T \ll 1$). The local dispersion relation as derived by PLUNK *et al.* [24] via expansion in ω/ω_*^T , is given by

$$\tau\omega^3 + (1 - b\eta)\omega_*\omega^2 + \omega_d\omega_*^T\omega + \frac{1}{2}\omega_*^T\omega_{\parallel}^2 = 0, \quad (3.24)$$

where $b = k_{\alpha}^2\rho_s^2$ and $\omega_{\parallel} = k_{\parallel}v_T$.

The limit of the **slab mode** is $\omega_{\parallel}^2/\omega^2 \gg \omega_d/\omega$, i. e. parallel dynamics dominate over magnetic drifts, which yields

$$\omega^3 + \omega_*\omega^2/\tau + \omega_*^T\omega_{\parallel}^2/2\tau = 0, \quad (3.25)$$

where additionally finite Larmor radius effects are neglected by setting $b = 0$. In the strongly driven limit, the last term on the left hand side, which is proportional to $(L_{T_i}\tau)^{-1}$, is relevant for the destabilisation of the mode. The mode is predominantly destabilised by the ion temperature

gradient and sensitive to the temperature ratio. The frequency scales as $\omega \propto \omega_*^{\text{T}1/3} \propto k_\alpha^{1/3}$.

The limit of the **toroidal mode** is $\omega_\parallel^2/\omega^2 \ll \omega_d/\omega$, i. e. magnetic drifts dominate over parallel dynamics, which yields

$$\tau\omega^3 + \omega_*\omega^2 + \omega_d\omega_*^{\text{T}}\omega = 0, \quad (3.26)$$

$$\Leftrightarrow \omega = \frac{1}{2\tau} \left(-\omega_* \pm \sqrt{\omega_*^2 - 4\tau\omega_d\omega_*^{\text{T}}} \right). \quad (3.27)$$

The destabilising part is the last term in the square root, which is proportional to $\kappa/(L_{T_i}\tau)$. In addition to the dependencies which are shared between the two branches, the toroidal mode is destabilised by the curvature, as expected. Its frequency scales as $\omega \propto k_\alpha$, since both ω_* and ω_d are linear in k_α . Accordingly, the toroidal branch dominates at short wavelength and the slab branch at long wavelength, which is confirmed even in non-local analysis [24]. This is the same qualitative behaviour as expected from the similarity to interchange instability and drift wave, respectively.

Both branches of the ITG mode are stabilised by the normalised density gradient through $\omega_* \propto L_n^{-1}$ and propagate in the ion diamagnetic direction. There is an additional stabilising effect due to magnetic shear, which is not obvious from the local dispersion relation but known from the discussion of the interchange instability. Global magnetic shear in toroidal geometry is the variation of the rotational transform in the radial direction, $\propto \iota'(\psi)$. In tokamaks, the global magnetic shear is defined as $s = -\frac{r}{\iota} \frac{d\iota}{dr}$ [7]. Due to magnetic shear, neighbouring flux tubes drift apart when following the magnetic field, which leads to an increase of k_\perp , causing an increased finite Larmor radius suppression [24]. This effect only manifests itself in a non-local approach.

3.2.3 Electron temperature gradient mode

The electron temperature gradient drives instabilities analogously to that of the ion temperature. Linearly, the ETG and ITG mode are symmetric, meaning the mechanisms are identical with the role of ions and electrons reversed. In comparison to other modes, the scale of ETG modes is much smaller due to $\rho_e \ll \rho_i$. As a consequence, they were not considered relevant for transport in tokamaks for a long time, since the mixing length approach

suggests low transport for small scale fluctuations. However, JENKO *et al.* [59] realised that the nonlinear evolution is qualitatively different: while ITG saturates in ZFs, ETG modes form radially elongated vortices, so-called streamers, in certain situations (mean shear $s \sim 1$ and low pressure gradient). These streamers are much more effective at plasma convection across flux surfaces than the small-wavelength ETG mode fluctuations. Heat transport due to ETG turbulence can reach confinement relevant values in classical tokamaks [14]. The nonlinear difference between ETG and ITG modes stems from the respective mechanism for the adiabatic response to ϕ . The fast parallel electron response due to low electron inertia in the ITG mode context is taken over by a perpendicular response by the larger ion gyration motion for ETG modes. In the gyrokinetic description, this difference appears as an additional term, $-\tau n \langle \phi \rangle_{\text{fs}}$, in the quasi-neutrality condition (equation (3.18)) for the ITG [56]. $\langle \phi \rangle_{\text{fs}}$ is the flux surface average of the potential, which is only relevant for secondary modes driving ZFs. Since it is missing in the ETG formalism, the generation of ZFs is restrained.

3.2.4 Trapped-electron mode

In simplest terms, collisionless trapped-electron modes arise due to a resonance between drift waves and the precession of trapped electrons [22, 73]. Wave-particle resonances are inherently kinetic mechanisms and a full kinetic description seems inevitable (even though bounce-averaged fluid equations for the description of TEMs were derived by BEER & HAMMETT [74]). For the TEM, the ordering of time scales is important. The frequency at which a particle in a banana orbit bounces between the reflection points, ω_b , depends on the thermal speed of the particle and is therefore different for ions and electrons. Generally, the mode frequency is taken to be intermediate [22, 74],

$$\omega_{bi} \ll \omega \ll \omega_{be}, \quad (3.28)$$

$$\omega \sim \omega_* \gg \omega_d \sim \nu_{\text{eff}}, \quad (3.29)$$

where $\nu_{\text{eff}} = \tau_{\text{eff}}^{-1}$ is the effective collision frequency of trapped electrons (cf. section 2.2.2). The ion bounce frequency is low compared to the mode frequency, such that to lowest order trapped and passing ions are the same on the time scale of the mode. The electron bounce frequency is much higher

and trapped electrons fulfil many orbits on the time scale of the mode and the precession drift becomes important. The ordering in equation (3.28) can be used to simplify the gyrokinetic equations of the ions and electrons.

For ions, the first term on the left hand side of the gyrokinetic equation (3.15) can be ignored and the solution is simply,

$$g_i \simeq \left(1 - \frac{\omega_{*i}^T}{\omega}\right) \frac{eJ_0\phi}{T_i} f_{i0}. \quad (3.30)$$

In tokamaks, the ordering furthermore implies a small fraction of trapped particles [22]. To lowest order, $g_e = 0$ and the ion solution in combination with the quasineutrality conditions just gives the drift wave dispersion, $\omega = \omega_{*e}$, for $b \rightarrow 0$.

For electrons, the fast bounce movement can be removed from the equation analogous to the gyro-average by applying the bounce-average [22],

$$\bar{Q}(\lambda) = \oint \frac{Q(l)dl}{\sqrt{1-\lambda B(l)}} \bigg/ \oint \frac{dl}{\sqrt{1-\lambda B(l)}}, \quad (3.31)$$

where $\lambda = v_{\perp}^2/(v^2 B)$ and the integration is performed along the banana orbit between two bounce points. This is analogous to the gyrokinetic average, where the particle movement which is much faster than the time scale of interest is removed from the equation via averaging. For trapped electrons the first term in equation (3.15) is dominant [22] but vanishes due to the bounce-average [57]. The solution for trapped electrons is then given by

$$g_{e0}^{\text{tr}} = -\frac{\omega - \omega_{*e}^T}{\omega - \bar{\omega}_{de}} \frac{e\bar{\phi}}{T_e} f_{e0}. \quad (3.32)$$

The denominator in equation (3.32) enables resonant drive of the mode through the bounce-averaged magnetic drift of the electrons, which characterises the precession of the trapped particles. However, since $\omega \sim \omega_{*e}$, the resonance only works if $\omega_{*e}\bar{\omega}_{de} > 0$, i. e. if the trapped electrons precess roughly in the electron diamagnetic direction. This can be understood as unfavourable bounce-averaged curvature [48]. In tokamaks, trapped particles precess toroidally and spend more time on the outboard side of the plasma, where the curvature is unfavourable. The conventional TEM is therefore

unstable. It is density-gradient-driven, propagates in the electron diamagnetic direction and the mode amplitude peaks in magnetic wells, where trapped electrons are located. It should be noted that this derivation assumes very low collision frequencies ('collisionless regime'). Collisions lead to de-trapping and stabilise the TEM. If the collision frequency is high enough, trapped electrons do not complete entire banana orbits and the resonance terminates.

It should be further noted that trapped electrons can also contribute to other modes on the drift wave scale, such as ITG modes. They are the primary cause for non-adiabatic electrons prohibiting a Boltzmann response to ϕ [74]. The only difference in the gyrokinetic formalism is the assumption that for the TEM ϕ vanishes in regions without trapped electrons, whereas for the ITG mode it satisfies the usual dispersion relation.

3.3 Micro-instabilities in W7-X

In W7-X, the same fundamental instabilities occur as introduced in the previous section for the general case. However, they exhibit specific properties owing to the complex W7-X magnetic field geometry. In the following, these differences are discussed for each instability. At the end of this section, particular expectations for the instabilities in typical W7-X discharges are formulated. Parameter scans and a radially resolved analysis of growth rates with linear gyrokinetic flux tube simulations are presented.¹ The basis for the radial analysis are model profiles of density, electron and ion temperature, which resemble a typical experiment situation. The simulations include kinetic electrons and ions, no collisions and only electrostatic perturbations.

3.3.1 Ion temperature gradient mode

The aspects of the ITG instability which are independent of the magnetic field geometry are identical in W7-X and tokamaks. Figure 3.4 shows ITG growth rates from linear flux tube simulations with kinetic electrons in GENE for various a/L_{T_i} and temperature ratios in the W7-X standard configuration. For each case, the maximum growth rate of the wavenumber

¹The simulations were planned and interpreted in close cooperation with J. A. Alcusón, who carried out the simulations with the GENE code.

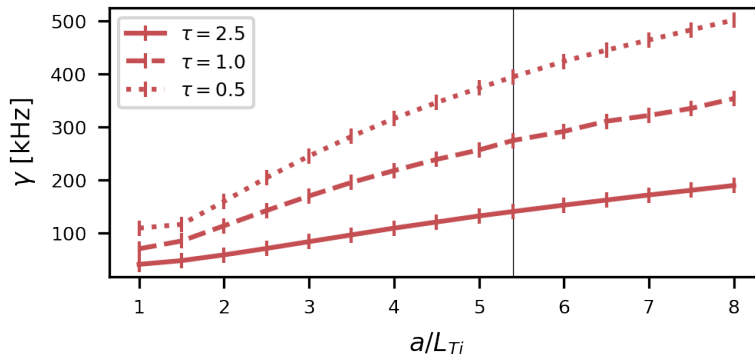


Figure 3.4: Simulated growth rates of the ITG mode for a range of inverse normalised ion temperature gradient lengths and three different temperature ratios, $\tau = T_i/T_e$. A finite density gradient, $a/L_n = 1$, and a flat electron temperature, $a/L_{T_e} = 0$, were assumed for the simulation.

spectrum is depicted. As expected, the growth rate increases with a/L_{T_i} and decreases with $\tau = T_i/T_e$. However, contrary to tokamaks, there is no critical gradient below which the mode is stable. Since there is always a finite density gradient in experiment situation, $a/L_n = 1$ was adopted in this example, which in principal enables density-gradient-driven modes at low a/L_{T_i} . However, a critical gradient is generally not observed even for pure ITG mode simulations [27]. Finite growth rate at very low a/L_{T_i} in W7-X is attributed to ITG modes of the Floquet type [27].

Stellarators should generally benefit from their negative global magnetic shear [8]. W7-X is a low shear device, cf. the flat ι profiles in figure 2.9, but the local shear between neighbouring flux tubes can vary significantly on a flux surface. Therefore a local magnetic shear is defined as $S = -\mathbf{X} \cdot (\nabla \times \mathbf{X})$ with $\mathbf{X} = \frac{\mathbf{B} \times \nabla \psi}{|\nabla \psi|^2}$ [7], which is equal to the global shear if averaged over a flux surface. Local shear in W7-X exhibits spikes along a flux tube, which affect the parallel mode structure of micro-instabilities. ITG modes can therefore be localised to certain regions on a flux surface by curvature, global or local shear and exhibit a generally more complicated parallel mode structure than in a tokamak [23, 24]. Furthermore, there is a poloidal localisation to the outboard side mid-plane in the bean shaped cross section, which is mostly attributed to the unevenly distributed curvature [8, 28, 75]. Both

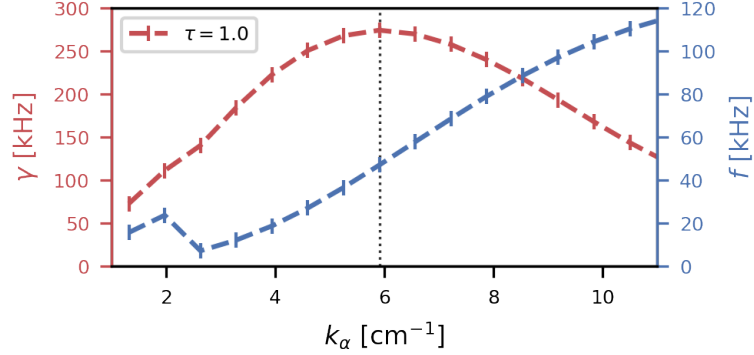


Figure 3.5: Simulated ITG growth rates and real frequencies in the relevant wavenumber range for different temperature ratios at $a/L_{T_i} = 5.4$.

linear growth rates as well as nonlinear fluctuation levels are confined to a narrow band in flux surface simulation results. Different flux tubes on the same flux surface can therefore exhibit considerably different fluctuation amplitudes, which is not the case for tokamaks. Another consequence of the poloidal localisation is a strong sensitivity to the radial electric field, E_r [28, 76]. Poloidal $\mathbf{E} \times \mathbf{B}$ rotation shifts growing modes out of the narrow strong curvature region and therefore reduces their overall growth rate. Note that this effect is due to radial electric field magnitude, not due to a flow shear induced by a radial gradient of E_r .

Due to the five-fold symmetry, the connection length between good and bad curvature regions is much shorter in W7-X than in a tokamak with similar size and aspect ratio. This was suggested to lead to a more ‘slab-like’ ITG mode in W7-X than in tokamaks [24]. However, the low negative shear is thought to favour the toroidal branch of the mode [27]. Indeed, linear simulations of experimentally relevant ion temperature gradient and density gradient show a linear scaling of the real frequency component with k_α indicating a toroidal ITG mode (cf. equation (3.26), dispersion relation of the toroidal ITG mode). Figure 3.5 shows the growth rate and frequency spectra at $a/L_{T_i} = 5.4$ and $a/L_n = 1$. The fastest growing mode is at $k_\alpha = 6 \text{ cm}^{-1}$. At this wavenumber, the frequency is linear in k_α at a phase velocity of $v_{\text{ph}} \approx 500 \text{ m s}^{-1}$.

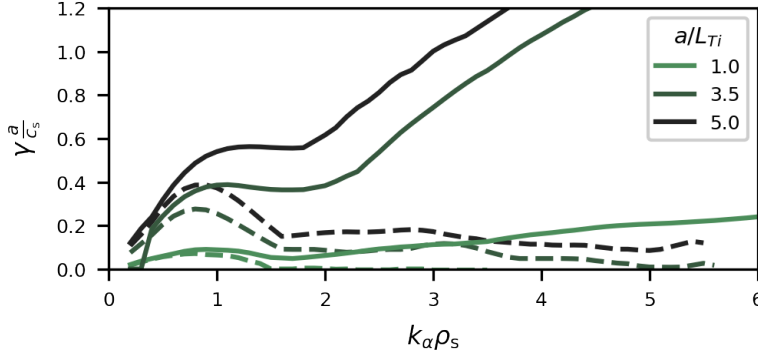


Figure 3.6: Growth rate spectra at different ion temperature gradient lengths from linear flux tube simulations with GENE. The solid lines correspond to simulations with equal gradients, $a/L_{T_i} = a/L_{T_e}$, the dashed lines represent simulations without electron temperature gradient ($a/L_{T_e} = 0$). In both cases, a finite density gradient, $a/L_n = 1$, is assumed.

3.3.2 Electron temperature gradient mode

It has been shown by PLUNK *et al.* [77], that ETG modes are less severe for transport in stellarators than in tokamaks if $T_i \approx T_e$. The negative shear in stellarators prevents the formation of radial streamers, which are the reason for large cross-field transport due to ETG modes in tokamaks. The condition of equal ion and electron temperature is only valid in the outer third of the plasma radius in common W7-X discharges. In the core, ETG modes were found to be relevant for experimentally measured electron heat transport [78]. Furthermore, their linear growth rate generally exceeds the ones of ITG modes and TEMs, albeit at larger wavenumbers. Figure 3.6 shows growth rate spectra for three different temperature gradients with $a/L_{T_i} = a/L_{T_e}$ (solid lines) and $a/L_{T_e} = 0$ (dashed lines). The cases without electron temperature gradient show the typical peak of the ITG mode at $k_{\alpha} \rho_s \lesssim 1$, which increases in amplitude for larger a/L_{T_i} . Simulations with electron temperature gradient exhibit much larger growth rates especially in the typical ETG mode wavenumber range $k_{\alpha} \rho_s \gtrsim 10$. However, even at large scales close to the ITG mode peak, ETG modes considerably affect the overall growth rate. It is therefore not clear at this point, which role

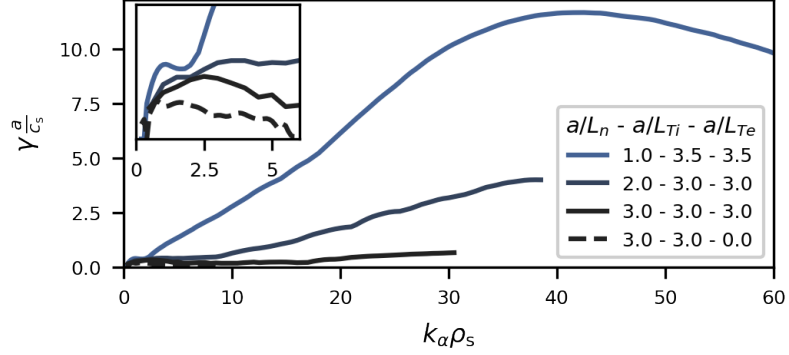


Figure 3.7: Growth rate spectra at different density gradients from linear flux tube simulations with GENE. ETG modes are considerably affected by the increasing density gradient and basically stable above $\eta_e = 1$.

ETG modes play for transport in W7-X in general.

An effective stabilisation of ETG modes with increasing density gradient is observed, which fits expectations. Figure 3.7 shows four growth rate spectra with similar temperature gradients and $a/L_{T_i} = a/L_{T_e}$ and increasing a/L_n . The inset shows an enlarged view of the low wavenumber part of the spectrum. The growth rate of ETG modes at large values of $k_{\alpha} \rho_s$ is strongly reduced for increasing density gradient. For $\eta_e \leq 1$, ETG modes are basically stable, a further increase of a/L_n does not reduce the overall growth any more. However, the electron temperature gradient must have some destabilising effect even at $\eta_e = 1$, since the growth rate is reduced for $a/L_{T_e} = 0$ (dashed line). This might be connected to a destabilising contribution of the electron temperature gradient to TEMs.

3.3.3 Trapped-electron mode

In high β discharges in configurations with high mirror, W7-X approaches the quasi-isodynamic symmetry. In this limit, it possesses the *maximum-J* property, where J is the second adiabatic invariant [26, 48],

$$J = \int m v_{\parallel} dl = m v \int \sqrt{1 - \lambda B(l)} dl. \quad (3.33)$$

J is constant on a flux surface, i. e. independent of α , and decreases radially, $\frac{\partial J}{\partial \psi} < 0$. The first property is a consequence of the quasi-isodynamic magnetic field. The bounce averaged radial magnetic drift of trapped particles then vanishes and the precession is poloidally closed [26, 49]

$$\overline{\nabla\psi \cdot \mathbf{v}_d} = \frac{1}{q\tau_{ba}} \frac{\partial J}{\partial \alpha} = 0. \quad (3.34)$$

The maximum- J property then has an effect on the direction of the poloidal precession of trapped particles [8, 26]

$$\overline{\nabla\alpha \cdot \mathbf{v}_d} = -\frac{1}{q\tau_{ba}} \frac{\partial J}{\partial \psi}. \quad (3.35)$$

For electrons, the bounce averaged magnetic drift is therefore [26, 48]

$$\bar{\omega}_{de} = k_\alpha \overline{\nabla\alpha \cdot \mathbf{v}_d} + k_\psi \overline{\nabla\psi \cdot \mathbf{v}_d} = \frac{k_\alpha}{e\tau_{ba}} \frac{\partial J}{\partial \psi} \quad (3.36)$$

such that it is opposite to the electron diamagnetic direction,

$$\omega_{*e} \bar{\omega}_{de} = -\frac{k_\alpha^2 T_e}{e^2 \tau_{ba}} \frac{\partial J}{\partial \psi} \frac{d \ln n_e}{d\psi} < 0. \quad (3.37)$$

The condition for conventional TEMs, $\omega_{*e} \bar{\omega}_{de} > 0$, is not fulfilled in devices with maximum- J geometry, i. e. trapped particles can not resonate with drift waves. This is equivalent to a favourable bounce averaged curvature. In W7-X, regions of unfavourable curvature and regions of trapped particles are separated. As a consequence, the standard density-gradient-driven TEM is inherently suppressed, which was confirmed by gyrokinetic simulations [23]. It is not completely stable, as it would be in perfectly quasi-isodynamic configurations, because in practice, the condition $\frac{\partial J}{\partial \alpha} = 0$ can not be fulfilled for all trapped particle orbits.

Other modes were found in numerical simulations, which are density-gradient-driven and peak in magnetic wells, as expected for TEMs, but propagate in the ion diamagnetic direction and have wavelengths on the order of the ion gyroradius. They draw their energy from the ions rather than the electrons and are referred to as the ion-driven TEM (ITEM). This type of mode was analytically described by PLUNK *et al.* [25] and arises through

a resonance of the mode with the ion magnetic drift. Trapped electrons are required to reduce the phase velocity sufficiently to enable this resonance. The resonance of the trapped electrons with the drift wave frequency is still stabilising for favourable bounce-averaged curvature and a finite electron temperature gradient additionally stabilises the mode. Nonlinear simulations indicate that the transport level is at least one order of magnitude lower than for comparable TEMs in tokamaks [26]. The mode structure does not necessarily peak in regions of unfavourable curvature.

Finally, electron-temperature-gradient-driven TEMs also exist, which are thought to appear on electron scales and propagate in the electron diamagnetic direction. As mentioned before, the electron temperature gradient is thought to be ineffective for destabilising TEMs [22]. Due to their small scale, it is not clear whether ∇T -driven TEMs contribute considerably to turbulent transport. On the other hand, there are indications for electron heat transport due to ∇T -driven TEMs in heat pulse propagation experiments [78] and the linear simulations results in figure 3.7 suggest a destabilising contribution of the electron temperature gradient at small wavenumbers and $\eta_e = 1$. The role of ∇T -driven TEMs in W7-X might therefore need more attention in theoretical studies.

Overall, trapped particle modes should play a minor role in W7-X. This is a contrast to tokamaks, where they account for a large fraction of the edge turbulent transport [14]. This becomes particularly clear, if the maximum linear growth rate of simulations with varying combinations of $(a/L_{T_i}, a/L_n)$ is depicted in a two-dimensional map. Towards higher values of a/L_{T_i} , ITG modes become unstable and show large growth rates and at large values of a/L_n , conventional TEMs become relevant. In between, however, at $\eta_i \approx 1$, a *stability valley* is formed, which does not exist in tokamaks or non-optimised stellarators [29].

3.3.4 Radial analysis and experimental expectations for experiment

In order to formulate theoretical expectations for the experiment, the growth rates of instabilities are analysed for varying r_{eff}/a . The basis for this analysis are model profiles of density, ion and electron temperature which resemble the experimental situation of gas-fuelled hydrogen discharges with ECRH.

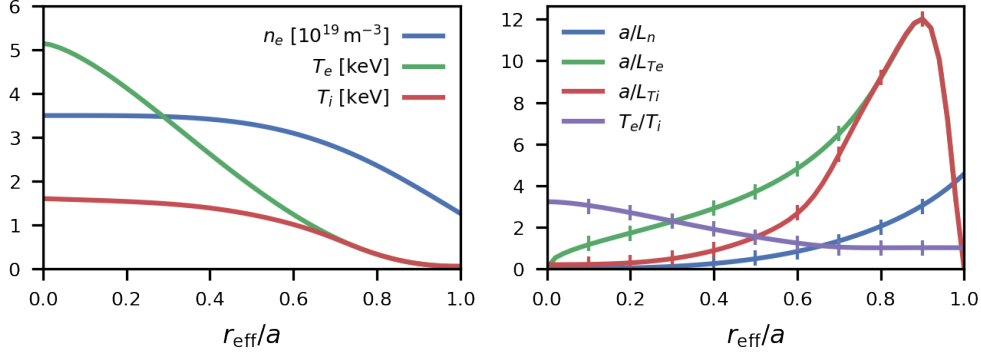
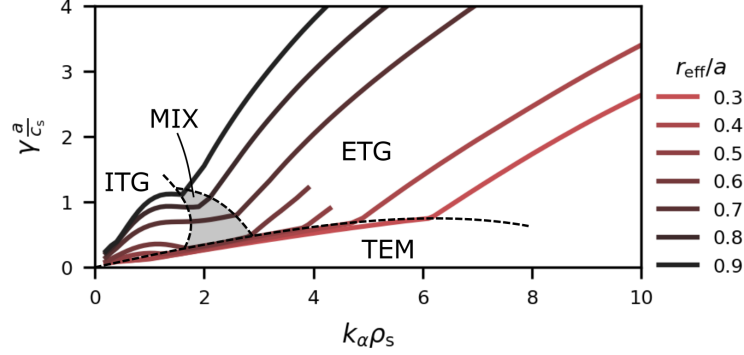


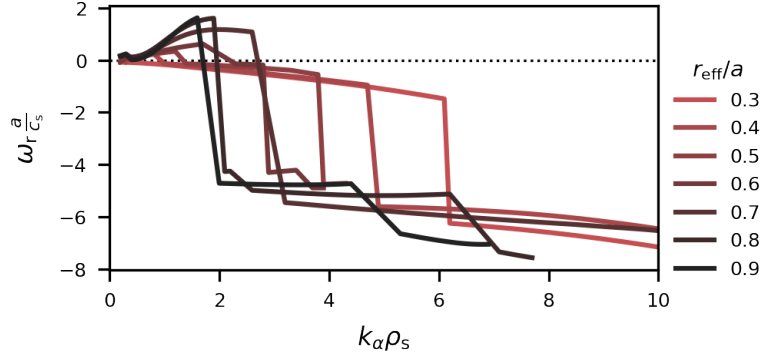
Figure 3.8: Typical radial profiles of plasma parameters during gas-fuelled hydrogen ECRH discharges in W7-X.

Flux tubes which pass through the high fluctuation band at the outboard mid-plane in the bean shaped cross section at the respective radius are selected for the simulations. Geometrical differences along the radius are therefore captured by the simulations as well. Figure 3.8 shows the radial profiles of T_e , T_i and n_e (left) as well as the corresponding normalised inverse gradient lengths, a/L_X (cf. equation (3.17)), and the ratio of ion and electron temperature (right), which are used as input for the simulation. The vertical lines in the right panel mark the values at the nine selected radial positions $r_{\text{eff}}/a = 0.1, 0.2, \dots, 0.9$. The central heating of electrons with ECRH in W7-X leads to generally peaked electron temperature profiles. The ion temperature profile is rather flat in the core and much lower than the electron temperature due to weak coupling between the two species at the relatively low density. They are in thermal equilibrium in the edge of the plasma, $r_{\text{eff}}/a > 0.7$. The density profile is flat in the core and develops a small gradient towards the edge. All normalised inverse gradient lengths increase towards the edge of the plasma. The density gradient does not increase as strongly as the temperature gradients, which suggests that the edge of the plasma is overall more unstable than core. The author acknowledges that the model profile of T_i as shown in figure 3.8 and used for the simulations underestimates the gradient close to the magnetic axis. The simulations at $r_{\text{eff}}/a < 0.3$ are therefore not considered in the following.

Figure 3.9 shows the growth rate and frequency spectra for the various



(a) Growth rate spectra.



(b) Frequency spectra.

Figure 3.9: Radial evolution of micro-instabilities in linear flux tube simulations with GENE. Gradients and temperature ratio are assumed according to figure 3.8.

radial positions. Generally, the growth rates increase towards the edge of the plasma, as expected from the gradient lengths. Due to the comparably large electron temperature gradient, there is a strong contribution of ETG modes, which are identified by their large growth rates at high wavenumbers with simultaneously high negative frequencies. Jumps in the frequency spectrum are attributed to a change of dominant mode type at this wavenumber. At low radii, the ETG mode growth rates are likely suppressed by the stabilising temperature ratio. For $r_{\text{eff}}/a \geq 0.5$, the typical ITG mode contribution

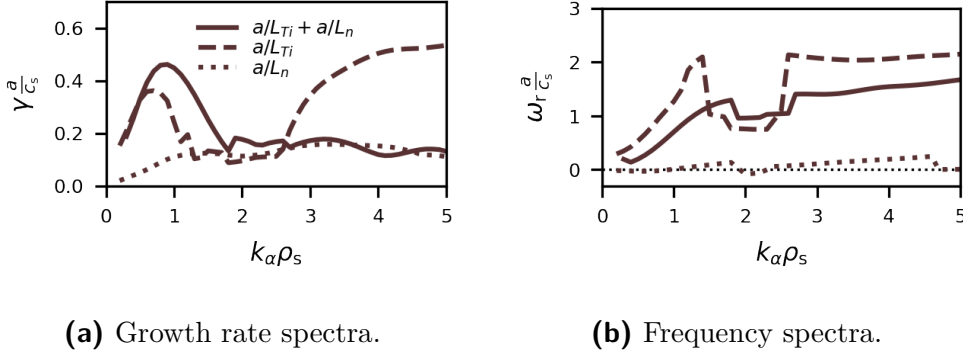


Figure 3.10: Comparison of ITG and TEM/ITEM in linear flux tube simulations with GENE. Gradients and temperature ratio are assumed according to $r_{\text{eff}}/a = 0.7$ in figure 3.8.

with positive frequencies is observed at $k_{\alpha} \rho_s \lesssim 1$. In the transition to the ETG mode regime, a mix of ITG mode and ITEM is suspected, because the frequencies are positive. In the inner half of the plasma, the ion temperature gradient is not large enough to drive strong ITG modes and there is another mode at large to medium wavelengths with moderate negative frequencies and relatively low growth rates, which is identified as a TEM. It is, however, somewhat surprising to find TEMs in a regime with virtually no density gradient, which suggests that the mode is predominantly electron-temperature-gradient-driven.

In any case, the strong growth rates at large radii suggest this region is more relevant for transport. In order to investigate the nature of the underlying modes, the growth rate spectra at $r_{\text{eff}}/a = 0.7$ as an example case are investigated in more detail. The simulations were repeated without electron temperature gradient for an isolated analysis of ITG mode and TEM. Figure 3.10 shows the growth rate and frequency spectra for three different cases: one with both ion temperature and density gradient and two with only one type of gradient each. The first case corresponds to the mixed case, the latter cases to isolated ITG mode and TEM, respectively. The cases are not additive, since the density gradient affects the growth rate of the ITG mode and vice versa. The stabilising effect of the density gradient on the ITG mode growth scale is subordinate compared to the destabilising potential for TEMs, because the growth rate of the mixed case

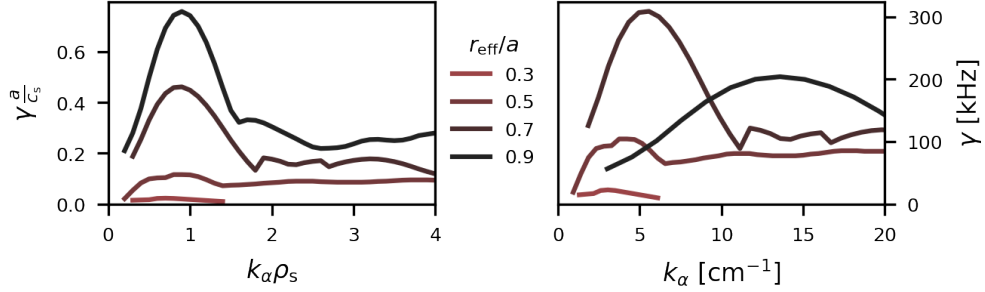


Figure 3.11: Growth rate spectra at different radii from linear flux tube simulations with GENE.

is increased even at $k_\alpha \rho_s \sim 1$. Merely a second high wavenumber part of the ITG mode is completely stabilised by the density gradient, and for $k_\alpha \rho_s > 3$ the growth rate of the mixed case is on the same level as the pure density gradient case. The frequencies are mostly positive, i. e. the mode propagates in the ion diamagnetic direction, which agrees with the ITEM. The mixed case exhibits similar growth rates but higher frequencies. Overall, this shows that a clear distinction of modes is not possible and possibly not useful, as ITG with trapped-electron contribution and ITEM blend into each other.

One important aspect of the interpretation of simulation results is taking the normalisation into account. Figure 3.11 shows growth rate spectra for four flux tubes without electron temperature gradient. The left panel shows the normalised spectra, which exhibit a peak of the growth rate at $k_\alpha \rho_s \lesssim 1$ typical for ITG modes. For larger radii, the growth rate increases mostly due to increasing a/L_{T_i} values. The normalisation of growth rates and wavenumbers which is generally used in simulations and for display depends on the ion sound speed and therefore varies radially. In the right panel of figure 3.11, the same growth rate spectra are depicted in real units as calculated for the given temperature profiles. The fastest growing mode is now at different values of k_α for each flux tube. Additionally, the maximum growth rate itself is also modified. While the flux tube at $r_{\text{eff}}/a = 0.9$ exhibits the strongest growth rates in normalised units, this is the case for the flux tube at $r_{\text{eff}}/a = 0.7$ in real units.

In summary, theoretical understanding suggests that the strongest instabilities arise in the outer half of the plasma, close to the edge. ITG

modes play a dominant role on ion scales, as expected, with possible contributions of ITEMS. Classic TEMs are strongly suppressed by the maximum- J property of W7-X and play a subordinate role. ETG modes are an important contribution to the linear growth rate spectrum at large radii and wavenumbers, but the mitigation of radial streamers by the negative shear in W7-X prevents strong transport due to ETG modes. At large wavelengths, which are generally more relevant for turbulent transport, ITG modes are clearly the most important mechanism to drive turbulence. There have already been experimental indications for this: in discharges with hydrogen ice pellet injection, improved energy confinement is observed after the pellet injection, which is attributed to a stabilisation of ITG modes by an increased density gradient in the plasma core [20, 79]. Furthermore, the flat ion temperature profiles which barely vary over the large number of discharges in past experiments are likely due to destabilisation of ITG modes by an increased ratio of T_e and T_i in the core [21]. Experimental density fluctuations in the drift scale and intermediate wavenumber regime are therefore expected to be mostly determined by ITG modes.

3.4 Zonal flows

Besides energy conservation, which is assumed a priori, the Hasegawa-Wakatani model yields a second conserved quantity, potential enstrophy [63]. This property is known to result in a dual cascade of energy and (potential) enstrophy in 2-dimensional fluid turbulence. The inverse cascade leads to a global mean flow pattern known as zonal flows. This observation in the Hasegawa-Wakatani model was the first direct indication of ZF generation in drift wave turbulence [63]. ZFs are known from geophysics and astrophysics, e. g. from the belts and zones of Jupiter. The flow goes along the zones, which stretch out in the longitudinal direction and vary in the latitudinal direction, as indicated in figure 3.12. In toroidal plasmas, ZFs are directed in the poloidal direction and have a radial structure, $k_r \neq 0$, but are toroidally symmetric, $n = 0$, as also illustrated in figure 3.12. They have zero frequency and are predominantly poloidally symmetric as well, $m = 0$, even though there may be some coupling to low- m sideband modes [80]. In both systems, the shear flow between the zones prohibits transport of vortices across the zones. Thus, ZFs reduce radial transport through turbulence in toroidal

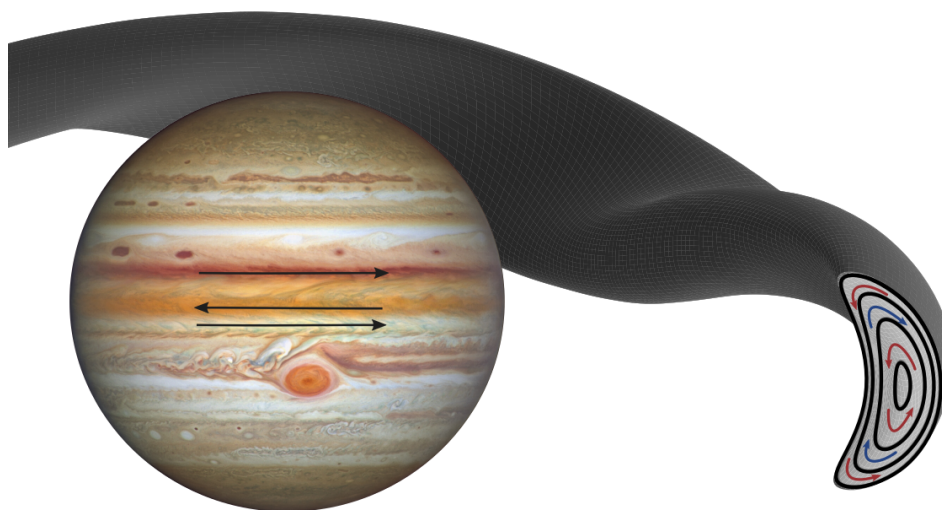


Figure 3.12: Illustration of ZFs in the turbulent atmosphere of Jupiter and in W7-X. Picture of Jupiter: ©NASA, ESA, A. Simon (Goddard Space Flight Center), and M.H. Wong (University of California, Berkeley) and the OPAL team; CC BY 4.0

devices. In other words, turbulence regulates itself through self-generated ZFs. There are two mechanisms to consider in this picture [81]:

1. Sheared flow causes a suppression of turbulent transport by limiting the scale size of vortices and thus the diffusive step size. The physical mechanism is the decorrelation of fluctuations as illustrated in figure 3.13 a)–c). Vortices are stretched by the flow shear until they break apart into smaller vortices. While this mechanism reduces transport, it does not transfer energy between the vortices and the ZF [81].
2. The energy transferred to ZFs is lost to turbulence and the intensity of the fluctuations which cause radial transport is reduced. ZFs therefore act as an energy sink reducing energy which is available for transport. The physical mechanism of the energy transfer from turbulence to ZFs is described by vortex stretching, which is illustrated in figure 3.13 d)–f). Vortices are sheared by the mean flow shear and strained out until taken over by the mean flow. Through this process, which is known in fluid turbulence as well, energy can be transferred from

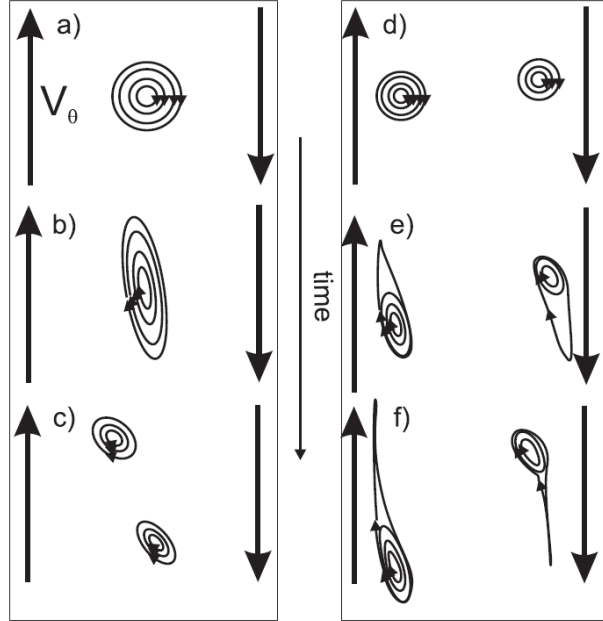


Figure 3.13: Artist view of decorrelation of vortices (a–c) and vortex thinning (d–f) due to ZFs. Taken from MANZ *et al.* [81].

vortices to the shear flow.

The second process describes the nonlinear generation of ZFs by drift wave turbulence, which received substantial attention by theoretical research in the last three decades. Generally, different scales of drift wave turbulence interact via *three-wave coupling*, which is a general feature of equations with quadratic nonlinearity [33]. Two modes, \mathbf{k} and \mathbf{k}' , can only interact via a third mode, \mathbf{k}'' , such that $\mathbf{k} + \mathbf{k}' + \mathbf{k}'' = 0$. In the context of ZF generation, this generally means that two high- k drift waves interact with one low- k_r zonal flow excitation [80]. The three-wave coupling appears explicitly through the quadratic vorticity nonlinearity in the Fourier representation of the Hasegawa-Mima equation [82].

This interaction is the basis for an approach to ZF generation which involves *secondary instabilities* [83–85]. The mechanism was proposed by COWLEY *et al.* [83] and describes ZFs as an instability which grows on the poloidal gradients of the primary instability (i. e. the drift wave). In a quasi-linear picture, saturation is reached when the growth rates of the

primary and secondary instability are similar, $\gamma_{\text{secondary}} \approx \gamma_{\text{primary}}$. More generally, secondary modes include all modes which are fed by the primary, but ZFs are usually the dominant component. The energy condensates at the largest scale as in the inverse cascade picture. An exception was found for ∇T_e -driven TEMs in tokamaks, where ZFs are not the dominant saturation mechanism and other secondary modes are more important [86]. Tertiary instabilities, which are generalised Kelvin-Helmholtz flow shear instabilities driven by the ZF, are believed to lead to a limitation of ZFs by returning energy back to $m \neq 0$ fluctuations [80].

An alternative approach to the secondary instability is the *modulational instability*. A radial modulation of the drift wave amplitude much like a radial envelope grows like an instability and leads to ZFs, as first shown by CHEN *et al.* [87]. Experiments show evidence for the modulational instability, which is observed as a reduction of energy at short wavelengths for increasing ZF amplitude [81].

In the words of STRINTZI & JENKO [82], the secondary and modulational instability as well as the wave kinetic approach »merely represent different ways of looking at the same physical phenomenon«. For certain simplifications, they can be shown to be equivalent [82]. A more descriptive picture is provided in real space as opposed to the mode coupling in Fourier space. Here, the nonlinear interaction is contained in the turbulent contribution to *Reynolds stress*, $\langle \tilde{v}_r \tilde{v}_\theta \rangle_{\text{fs}}$. Poloidal flow is generated via [88]

$$\frac{\partial}{\partial t} \langle v_\theta \rangle_{\text{fs}} = - \left\langle \frac{\partial}{\partial r} (\tilde{v}_r \tilde{v}_\theta) \right\rangle_{\text{fs}}, \quad (3.38)$$

which describes the amplification of shear flow by fluctuating velocity components and is closely related to the physical picture of vortex stretching.

A comprehensive review of the phenomenology, dynamics and generation mechanisms of ZFs was compiled by DIAMOND *et al.* [80]. It should be noted that the regulation of turbulence via ZFs is different from turbulent transport suppression by sheared mean $\mathbf{E} \times \mathbf{B}$ flow. The latter arises in the context of transport barrier formation and prevails even in the absence of a drift wave drive (cf. reviews by BURRELL [89] or TERRY [90]). In past experiments of W7-X, the measurements of the mean radial electric field agreed well with expectations for the neoclassical ambipolar field [91–93]. The shearing rate of the neoclassical E_r is too low for shear suppression of turbulence.

3.4.1 Zonal flows in W7-X

In toroidal geometry, poloidal flow inevitably leads to a density compression on the inboard side of the torus. This compression then relaxes as an acoustic wave, which is known as the geodesic acoustic mode (GAM). The dispersion relation takes the simple form [94]

$$\omega_{\text{GAM}} = \frac{c_s}{R} \sqrt{2 + \iota^2}, \quad (3.39)$$

where R is the major radius of the torus. For a typical discharge in W7-X standard configuration at $r_{\text{eff}}/a = 0.7$, $\omega_{\text{GAM}}/(2\pi) \approx 35$ kHz. Due to their specific frequency, GAMs are a useful characteristic feature for the identification of ZFs, which are otherwise challenging to measure. In many devices, GAMs have been experimentally observed as flow or potential oscillations. In W7-X, GAMs are predicted to be weakened [95], but ZFs exhibit a different oscillating part, which is specific to stellarators: *Mishchenko oscillations* [95, 96]. A zonal electric potential perturbation decays exponentially in tokamaks due to a slow compensation by trapped ions. In stellarators, such a perturbation leads to an oscillatory behaviour in addition to the exponential decay, which was first described analytically by MISHCHENKO *et al.* [96]. The oscillation stems from the finite bounce-averaged radial drift of locally trapped particles. The larger this drift, the higher the ZF oscillation frequency, ω_{ZF} . The tokamak is the limit of zero radial drift and thus $\omega_{\text{ZF}} = 0$. Due to its neoclassical optimisation, which results in almost vanishing bounce-averaged radial drift, the ZF oscillation frequency in W7-X is very low compared to that of the GAM, $\omega_{\text{ZF}}/(2\pi) \approx 1$ to 3 kHz [97]. Mishchenko oscillations have previously been measured in the less optimised low-shear stellarator TJ-II in the range of 10 kHz [98].

In both tokamaks and stellarators, a finite amount of zonal electric potential remains after the exponential (or oscillatory) decay, the Rosenbluth-Hinton (RH) residual. In tokamaks, the magnitude of the RH residual is assumed to determine the ZF amplitude [80]. In stellarators, the RH residual is lower than in tokamaks, but the ZF amplitude is found to be much larger and mostly affected by the magnetic geometry [99]. In particular, the geodesic curvature, $\kappa_g = (\hat{\mathbf{n}} \times \hat{\mathbf{b}}) \cdot \boldsymbol{\kappa}$, where $\hat{\mathbf{n}} = \nabla\psi/|\nabla\psi|$ is the flux surface normal, is identified as an important ingredient. For the example of W7-X, lower κ_g was found to result in a smaller oscillation frequency and a larger ZF amplitude [99].

ZFs are ubiquitous in dynamical models of fusion plasma turbulence and expected to exist in W7-X in some way or another. They occur in gyrokinetic simulations for W7-X [75, 100, 101] and have been measured on numerous devices [102] including the low-shear stellarator TJ-II [98, 103]. ZFs and their radial structure have previously been measured by correlating two toroidally and radially separated heavy ion beam probe (HIBP) measurements [104] and via 2-dimensional probe head measurements in the edge of the plasma [98]. So far, W7-X is missing the diagnostic capability to measure the fluctuating potential at two spatially separated measurement points. The reader is referred to FUJISAWA [102] for a general review on ZF measurements in other devices.

4

Diagnosics and Analysis

Studying micro-turbulence in plasma experiments breaks down to the problem of measuring small scale fluctuations. The relevant fluctuating measurement quantities are density, \tilde{n} , temperature, \tilde{T} , electrostatic potential, $\tilde{\phi}$, and the magnetic field, $\tilde{\mathbf{B}}$. The turbulent heat and particle fluxes can not be measured directly and must be determined from the fluctuating quantities and their cross-phase. Since the fluctuations are usually small compared to the steady-state values of the plasma parameter, i.e. the fluctuation degree is much smaller than one, it is often not feasible to apply the same diagnostics which are used to measure steady-state values. Another challenge is posed by their spatial localisation and the wide range of spatio-temporal scales which need to be resolved. These requirements evoked the development of new techniques and diagnostic designs [105, 106]. On W7-X, several fluctuation specific diagnostics were installed and operated in the first two experiment campaigns, such as various probes scanning the edge plasma on the Multi-purpose manipulator (MPM) [107, 108], Doppler back-scattering (DBS) [109], correlation ECE (CECE) [110], poloidal correlation reflectometer (PCR) [111], and PCI [112–114]. Several more are being developed and installed for the upcoming experiments, such as gas puff imaging (GPI), beam emission spectroscopy (BES), a HIBP and ECE imaging (ECEI). For a detailed discussion of diagnostic instrumentation for micro-turbulence including most of the diagnostics mentioned here, see [106]. Only the CECE diagnostic, measuring electron temperature fluctuations, and the PCI diagnostic, measuring line-integrated density fluctuations, were able to measure throughout the entire plasma radius in previous experiments of W7-X. The focus of this work is the analysis of measurement data from the PCI dia-

gnostic. For PCI, the advantage of being sensitive to density fluctuations in the core and edge of the plasma comes with the disadvantage of having no radial resolution due to the line-integration. The measured fluctuations are in general turbulent and not regular, which means a characterisation can only be done via their spectral properties. They provide information about the micro-instabilities causing the fluctuations, which are of interest for understanding turbulence in fusion plasmas and ultimately how to control it.

The rest of this chapter is organised as follows: in section 4.1, the working principle of the PCI method as well as the technical details and capabilities of the PCI diagnostic at W7-X is described. Section 4.2 contains the description of the necessary analysis tools for the evaluation of PCI data with respect to turbulence studies. This includes general methods for signal processing as well as specific analysis tools for PCI which were developed in the framework of this project.

4.1 Phase contrast imaging

PCI is a well established method to visualise phase objects with improved contrast. It was first developed by dutch physicist Frits Zernike [115], who later was awarded the 1953 Nobel Prize in Physics »for his demonstration of the phase contrast method, especially for his invention of the phase contrast microscope« [116]. The PCI principle has also been adapted for measuring a line-integrated fluctuating electron density in plasmas [117, 118]. The density fluctuations, \tilde{n} , can be regarded as a phase object for infrared (IR) lasers, due to the change in refractive index that is associated with them. Using PCI, an image of the density fluctuations can be measured, even in absence of a background density gradient, as it is required for e. g. DBS. The appeal of this technique is the clever, direct way of measuring density fluctuations, which produces data containing spatio-temporal information about the turbulence throughout the whole plasma. It comes, however, with the trade-off that there is no resolution along the line of sight (LOS) and the measurement data is difficult to interpret correctly due to the line-integration.

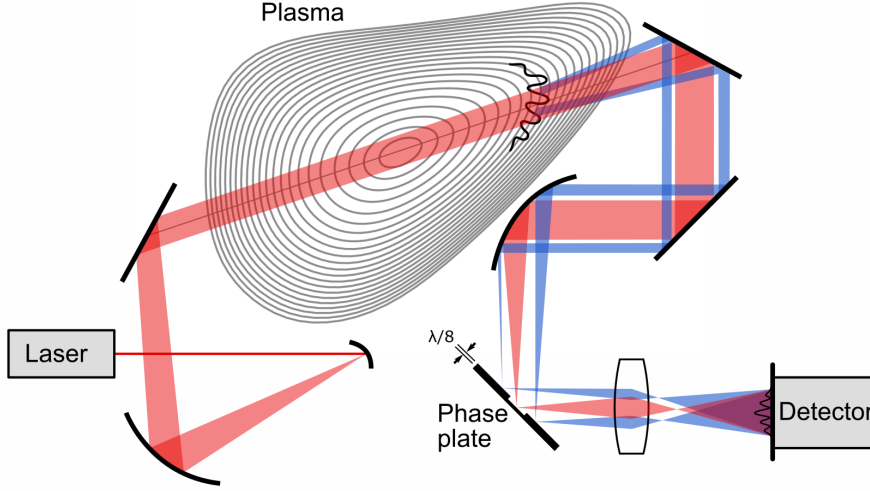


Figure 4.1: Principle phase contrast imaging diagnostic setup.

4.1.1 Working principle

When collimated light travels through a medium with varying refractive index, a non-uniform phase shift is introduced to the electromagnetic field of the light. The structure within the medium, e. g. the density fluctuations in a fusion plasma, is called the phase object. The phase shift can not directly be measured with common detectors which measure the intensity of the light, $I = |\mathbf{E}|^2 / (2\eta_0)$, where \mathbf{E} is the electric field vector and η_0 is the vacuum impedance. In order to make the phase object visible, the phase shift has to be converted to a change of intensity in an image plane. This is done by separating the part of the light which scatters on the phase object in the focal plane and introducing an additional phase shift relative to the unscattered part. Since the turbulent fluctuations in fusion relevant plasmas are generally much smaller than the mean density, $\tilde{n}_e/\bar{n}_e \sim \mathcal{O}(10^{-2})$, they can not easily be measured by other diagnostics for the electron density. On many magnetic confinement experiments (TCA [118], DIII-D [119–124], Alcator C-Mod [121, 125–127], TCV [128, 129], HL-2A [130], LHD [131, 132], W7-X [112–114, 133]), PCI systems have therefore been installed for investigating density fluctuations. Figure 4.1 shows a schematic drawing of a PCI diagnostic for plasma devices using W7-X flux surfaces as an example.

An IR laser beam is broadened and sent through the plasma, which is represented by the Poincaré plot of the magnetic flux surfaces. The phase shift of the laser beam after the plasma is determined by the refractive index along the LOS, N , which is proportional to the electron number density, n_e , [134]

$$\phi(\mathbf{x}_\perp) = \frac{2\pi}{\lambda_0} \int_{\text{LOS}} N(\mathbf{x}_\perp, z) dz \approx \frac{2\pi}{\lambda_0} L - r_e \lambda_0 \int_{\text{LOS}} n_e(\mathbf{x}_\perp, z) dz, \quad (4.1)$$

where \mathbf{x}_\perp and z are the directions perpendicular to and along the laser beam path, respectively, L is the total length of the LOS, λ_0 is the free space wavelength of the laser and r_e is the classical electron radius. The turbulent nature of the fluctuations allows for the Reynolds decomposition of electron density, $n_e = \bar{n}_e + \tilde{n}_e$, in equation (4.1) and accordingly of the phase shift, $\phi = \phi_0 + \tilde{\phi}$, where

$$\tilde{\phi} = -r_e \lambda_0 \int_{\text{LOS}} \tilde{n}_e dz. \quad (4.2)$$

The electric field of the laser beam including the phase shift can then be expressed as [121]

$$\mathbf{E} = \mathbf{E}_0 e^{i(\phi_0 + \tilde{\phi})} \approx \mathbf{E}_0 e^{i\phi_0} (1 + i\tilde{\phi}), \quad (4.3)$$

where \mathbf{E}_0 is the electric field of the laser beam before the plasma and the expansion is justified by $\tilde{\phi}$ being small. A direct measurement at this point would result to first order in $I \propto |\mathbf{E}|^2 = |\mathbf{E}_0|^2 (1 + \tilde{\phi}^2) \approx |\mathbf{E}_0|^2$. The part of the beam which is shifted by $\tilde{\phi}$ is scattered by a small angle since the wavelength of the laser is chosen to be much smaller than the typical length scale of the spacial variation of $\tilde{n}_e(\mathbf{x}_\perp, z)$. The scattered part is drawn in blue in figure 4.1. The separated unscattered and scattered parts are focussed onto a phase plate in order to introduce a relative phase shift between the parts. The phase plate is a mirror with a central groove of depth $\lambda_0/8$. The scattered part hits the main surface of the mirror and the unscattered part is focussed into the groove such that a path length of $\lambda_0/4$ and thus a phase of $\pi/2$ is added relative to the scattered part. In the image plane, which is at the detector in figure 4.1, the beams can interfere and the field is now given by $\mathbf{E} = \mathbf{E}_0 e^{i\phi_0} (i + i\tilde{\phi})$. The modulation of the phase is now translated linearly

to a modulation of the intensity, $I \propto |\mathbf{E}_0|^2 (1 + 2\tilde{\phi} + \tilde{\phi}^2) \approx |\mathbf{E}_0|^2 (1 + 2\tilde{\phi})$. The intensity at the detector can again be split up into $I = I_0 + \tilde{I}$, where $\tilde{I} \propto \int_{\text{LOS}} \tilde{n}_e dz$, which is the key proportionality for the measurement of turbulent density fluctuations. Even though the contrast between the mean and the fluctuating signal can be strongly increased using PCI, the constant part of the signal is generally still much larger due to $\tilde{n}_e/\bar{n}_e \ll 1$. Since the scattered and unscattered part of the beam are separated at the phase plate, it is possible to selectively reduce I_0 by only partially reflecting the beam in the phase plate groove. The remaining reflected fraction, which is needed to create the phase contrast signal, is electrically filtered out after the detector and before digitising the signal.

4.1.2 The PCI diagnostic at W7-X

The PCI system at W7-X was developed in a collaborative effort between the MIT Plasma Science and Fusion Center (PSFC), the IPP and SUNY Cortland. Detailed descriptions of the optical setup and the diagnostic capabilities can be found in [112–114]. In this section, a summary of the most relevant components and features of the diagnostic in its state during the OP1.2a and OP1.2b experiment campaigns is provided. A number of changes to the setup and optics layout are since implemented for the upcoming OP2 experiment campaigns. The principle setup and key features, however, are unchanged. Figure 4.2 shows a drawing of the full PCI setup in the experiment hall. It consists of a laser optical table, which hosts the IR laser and adjacent optics, two mirror boxes and beam lines, which guide the laser beam through two opposing entry ports of the W7-X plasma vessel, and a detector optical table, where the detectors and other crucial optical components are located. On the laser table, a Synrad Firestar t60 CO₂ laser with wavelength $\lambda_0 = 10.6 \mu\text{m}$ and 100 W continuous wave (CW) output power is installed, which generates the probe laser beam. For the alignment of the optical system, an additional visible HeNe laser is used, which is co-aligned to the IR laser beam early in the beam path. The two laser beams each pass through a telescope on a motorised remote controllable stage, which adjust the beam diameter. A magnification of $M = 0.8$ to 4 can be achieved with the IR laser telescope. An additional fixed telescope which consists of two off-axis parabolic (OAP) mirrors with a magnification

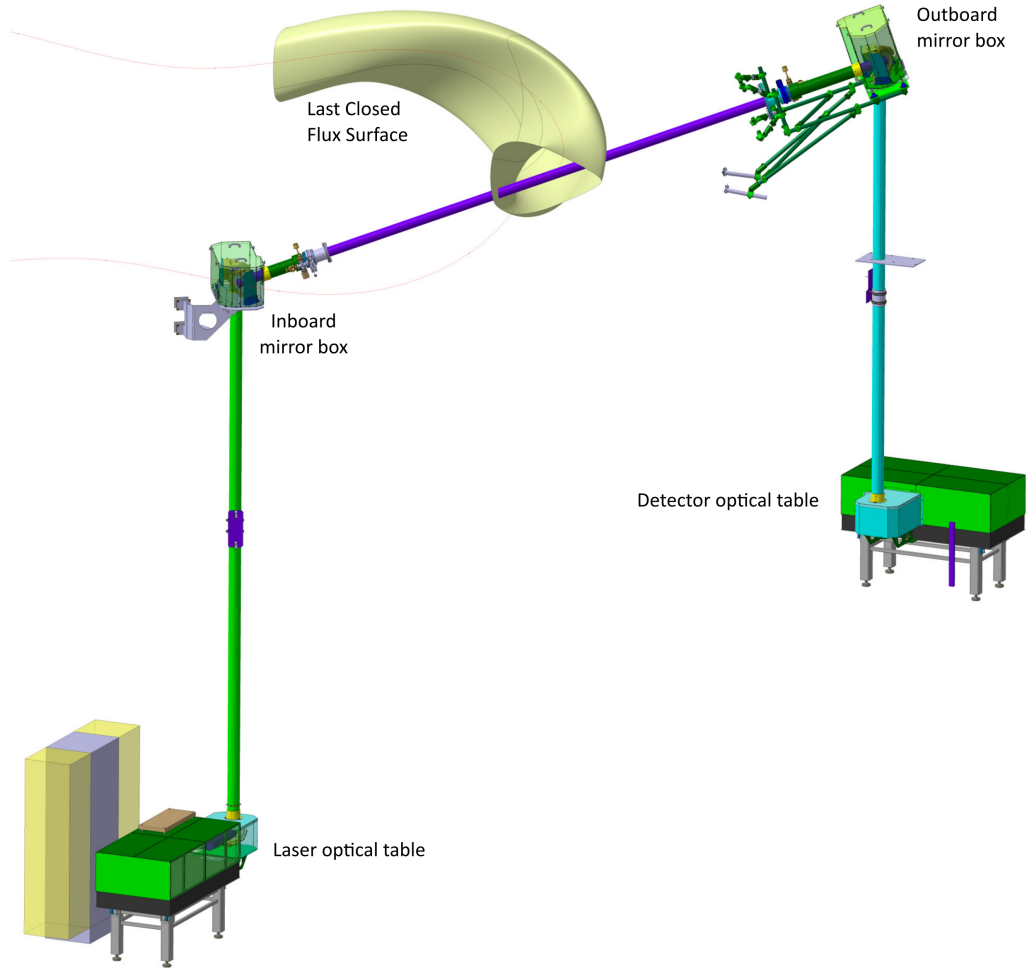


Figure 4.2: Setup of the PCI diagnostic at W7-X.

of $M = f_2/f_1 = 80"/9" = 8.9$ increases the laser beam diameter to its final width before leaving the laser optical table towards the plasma vessel. The beam width after the transmitting side optics is typically set to 80 to 100 mm with a full achievable range of 25 to 140 mm. After passing through the plasma vessel, the laser beam hits a focussing OAP mirror on the detector optical table. The orientation of the beam is adjusted by a beam rotator in order to match the average direction of the imaged field aligned fluctuations to the orientation of the phase plate and the 1d detector array.

The fluctuations are assumed to be elongated along the magnetic field and propagate perpendicular to it within the flux surface. The pitch angle of the magnetic field within the LCFS varies within a range of 22 degrees along the PCI LOS. The centre of this range is chosen as a reference for the exact angle of the beam rotator, such that the measurement direction is perpendicular to the magnetic field at that point. In the focal plane after the beam rotator, the phase plate is installed. It is a gold plated ZnSe substrate with a 1.1 mm wide central groove. The width of the groove, d , and the focal length of the large OAP mirror, $f = 80''$, determine the lowest wavenumber which can be resolved [112], $k_{\min} = \pi d / \lambda_0 f = 1.6 \text{ cm}^{-1}$. After the phase plate, a small OAP mirror collimates the beam and forms a telescope with the first OAP mirror with magnification $M = 6'' / 80'' = 0.075$. The beam is finally split into two equal parts each passing through a telescope on a motorised remote controllable stage and hitting one of the two detectors. The net magnification of the receiving side optics ranges from $M = 2.67$ to 13.33 , which sets the Nyquist wavenumber to $k_N = 4.7$ to 23.5 cm^{-1} , considering the spacing between the detector elements, $\Delta_{\text{det}} = 0.5 \text{ mm}$. Additionally, a system for radial localisation of the measurement using selective mask filters as well as a feedback system for compensating mechanical vibrations were implemented [112, 114] but not yet successfully applied during the past experiments.

The diagnostic is equipped with a Fostex FT17H sound speaker for calibration purposes. The variation of the refractive index in air due to pressure fluctuations of an ultrasonic sound wave causes a phase shift in the laser beam which is analogous to the phase shift induced by electron density fluctuations in the plasma [125]. The usage of sound waves for the calibration of PCI diagnostics on fusion experiments was first proposed by Weisen [118] and has been implemented for other PCI systems as well [122, 125, 135–137]. Figure 4.3 shows a schematic of the sound wave measurement. The sound wave is launched before every discharge such that there is no plasma in the vessel and a phase contrast image of only the pressure fluctuations is measured. The speaker is located outside of the plasma vessel in the outboard mirror box (see figure 4.2). It is installed at an angle such that the sound wave propagates through the laser beam along the measurement direction. This setup enables a direct measurement of the wavenumber of the fluctuations. The sound wave of the speaker has a well defined frequency, wavenumber and amplitude, which makes it suitable for calibration. The

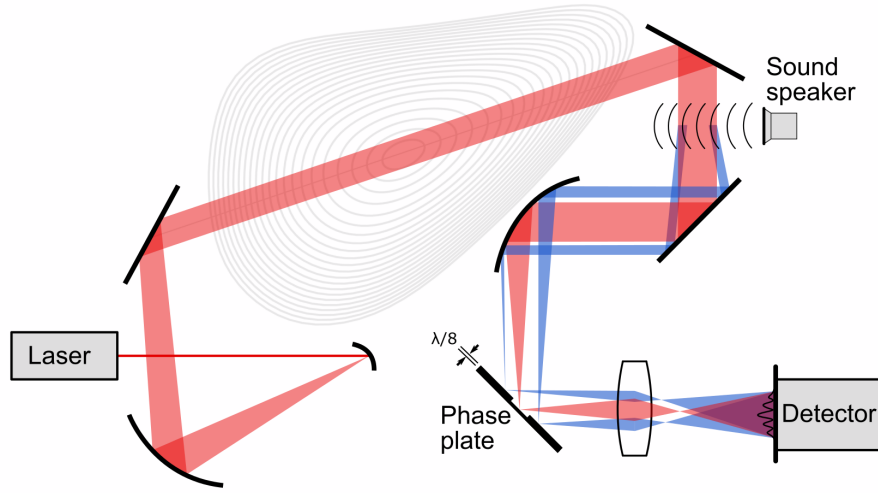


Figure 4.3: Schematic of a sound wave measurement for calibration.

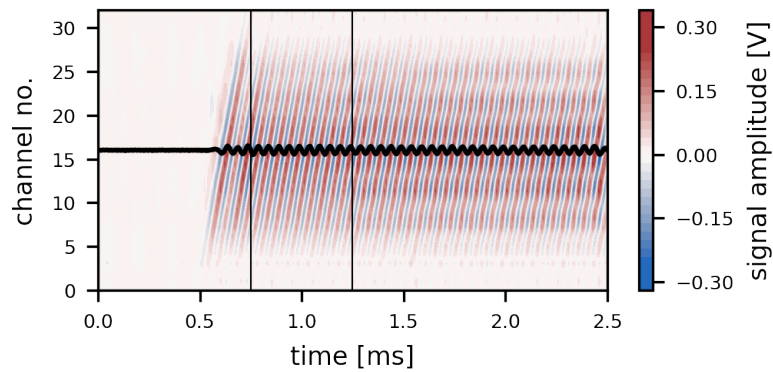


Figure 4.4: PCI measurement of a 20 kHz sound wave. The solid black line represents the signal amplitude of the central LOS. The sound wave is launched by the speaker at 0 ms.

speaker can be operated continuously or launch bursts of various frequencies. A burst with frequency $f_{\text{sw}} = 20 \text{ kHz}$ and wavenumber $k_{\text{sw}} = 3.7 \text{ cm}^{-1}$ is used for calibration. Figure 4.4 shows a measurement of such a burst. The signal amplitude is represented by colour. The solid black line represents the signal amplitude of the central LOS and depicts a clear sinusoidal wave-

form. The sound wave is launched by the speaker at the beginning of the measurement and arrives at the closest LOS (channel no. 1) 0.5 ms later. The wave front travels across the detector array until it reaches the last LOS 0.75 ms after the launch, which is marked by a vertical black line in figure 4.4. The timing matches the expectations set by the speed of sound in air at room temperature and a magnification of the receiving side optical system of $M = 5$. The signal amplitude is highest for the central channel and decreases towards the edges of the detector, which is due to the Gaussian cross section of the laser beam. A second vertical black line in figure 4.4 marks the time 1.25 ms after the launch of the sound wave at which the amplitude profile changes and an interference pattern appears. The pattern is caused by a standing wave which is the superposition of the forward wave and a reflected wave reaching the laser beam at that time point. The lid of the mirror box is lined with sound absorbing material in order to reduce the impact of the reflected wave. Nevertheless, the time window between 0.75 ms and 1.25 ms after the launch with the unperturbed sound wave is used for amplitude calibration.

For the absolute amplitude calibration, the corresponding pressure fluctuations need to be measured. They are obtained using a calibrated microphone. Figure 4.5 shows the 2d measurement of the sound field above the speaker during a continuous 20 kHz emission. The speaker is located at $h = 0$ cm and $x = 0$ cm. The sound pressure decreases stronger in the lateral direction, x , than in the frontal direction, h . The dotted white line in the colour plot marks the height of the central LOS above the speaker in the mirror box, which is also the centre of the laser beam. The top panel shows the sound pressure amplitude at that height. Since it decreases rapidly for larger $|x|$, the contribution of the wave outside of the measurement boundaries is neglected. The pressure amplitude integrated along x decreases linearly with increasing height above the speaker, which is shown in the right panel. The wave pattern which is visible in the colour plot and the line plot of $\int \tilde{p} dx$ is a measurement artefact. The black dashed line is the result of a linear regression on the measurement data and is considered to be a better representation for $\int \tilde{p}(x, h) dx$. The value at the height of the central LOS, which is considered for the absolute amplitude calibration, is marked by thin dotted lines. Sections 4.2.3 and 4.2.5 cover the details of this calibration.

At the end of this section, it is worth discussing the diagnostic capabilities from the standpoint of theoretical modelling expectations. The first thing

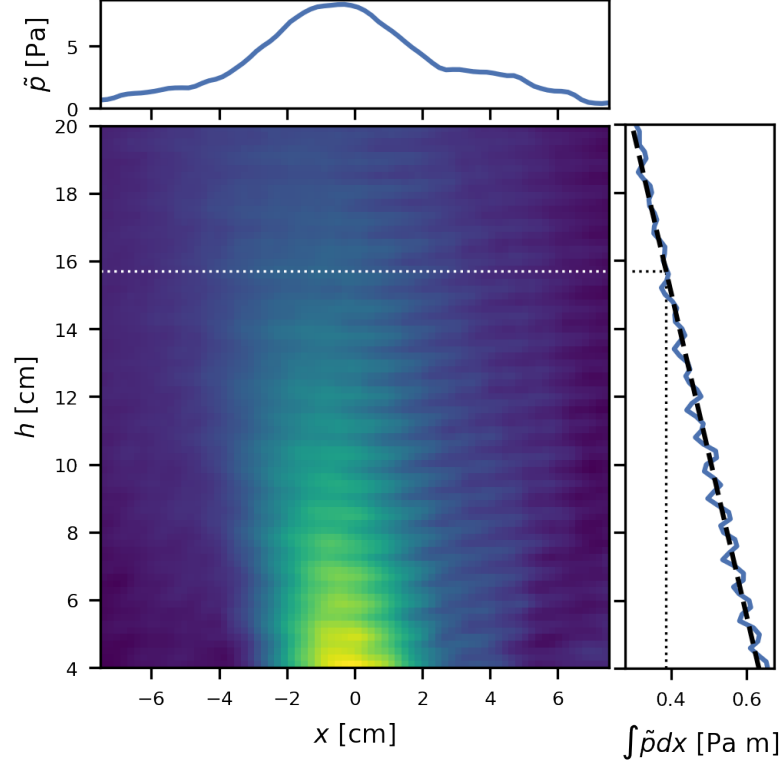


Figure 4.5: Sound field measurement above the speaker used for calibration. The dotted white line in the colour plot marks the height of the central LOS above the speaker. The top panel shows the sound pressure amplitude at that height. The right panel shows the line-integrated pressure amplitude for each height.

which is discussed is the wavenumber range of the fluctuations. As discussed in 3.3.4, the linear growth rates of ITG mode and TEM obtained from flux tube simulations with GENE are the largest at $r_{\text{eff}}/a \approx 0.7$. At this radius, the wavelength of the fastest growing mode is $k_{\alpha} \approx 6 \text{ cm}^{-1}$. Wavenumber of the dominant mode decreases towards smaller radii and increases towards the edge in a range between $k_{\alpha} = 2$ to 15 cm^{-1} (see figure 3.11). Since the lower wavenumber limit of the PCI diagnostic is $k_{\text{min}} = 1.6 \text{ cm}^{-1}$ and the accessible upper limit is $k_{\text{N}} = 4.7$ to 23.5 cm^{-1} , the fastest growing modes should be captured well up to the very edge of the confined plasma. It

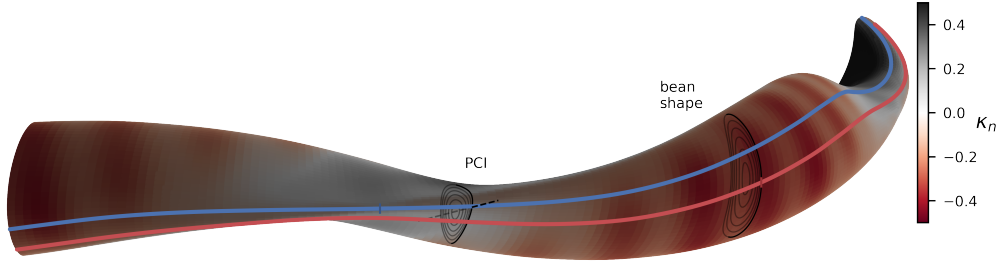


Figure 4.6: Cut of the W7-X standard configuration flux surface at $r_{\text{eff}}/a = 0.75$ with normal curvature on the surface represented by colour and flux tubes passing through the outboard LOS of the PCI diagnostic (blue) and the outboard mid-plane of the bean shaped cross section (red).

should be noted that the dominant scale of fluctuations in the nonlinearly developed spectrum does not necessarily agree with the dominant linear scale, but is usually shifted towards larger wavelengths. In conclusion, the PCI diagnostic should be sensitive to ITG modes and TEMs up until the very edge and by that also cover the radial range with the fastest growing modes.

Besides the spatial resolution, the measurement location is also particularly important for turbulence studies in stellarators. As described in section 3.3, the intensity of density fluctuations due to ITG modes varies strongly along flux tubes and across the flux surface. One of the most important aspects for the localisation of modes is the magnetic curvature, which leads to a narrow band of strong fluctuations on the outboard side mid-plane in the bean shaped cross section. The exact measurement position is therefore relevant for the interpretation of measurement data and the comparison to theoretical expectations. In figure 4.6, a flux surface at $r_{\text{eff}}/a = 0.75$ is depicted with colour coded normal curvature, $\kappa_n = \hat{\mathbf{n}} \cdot \boldsymbol{\kappa}$, across the surface. A Poincaré plot marks the toroidal position of the PCI diagnostic with the LOS being represented by a dashed black line. Similarly, the bean shaped cross section is shown. The flux tube which passes through the outboard mid-plane at the toroidal angle of the bean shaped cross section (red, in the following referred to as *bean shape flux tube*) is considered the most unstable flux tube with the most unfavourable curvature and the strongest density and potential fluctuations [28, 138]. The flux tube which

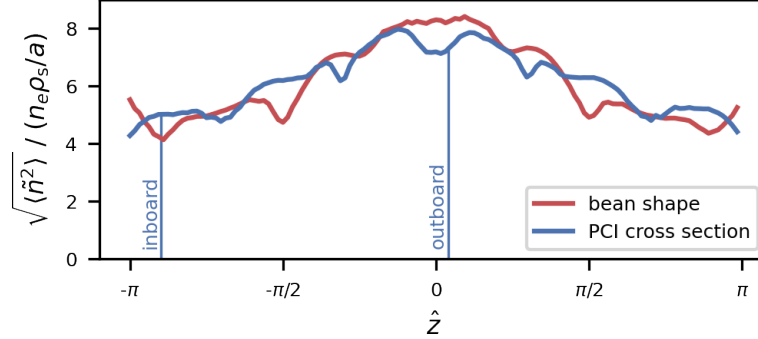


Figure 4.7: Density fluctuations along the flux tube from nonlinear simulations with GENE. \hat{z} is the coordinate along the flux tube, where $\hat{z} = 0$ is defined at the outboard mid-plane and $\hat{z} = \pm\pi$ at the inboard mid-plane. The flux tubes are on the same flux surfaces but at a different Clebsch-angle, α . The vertical lines mark the intersections with the PCI LOS.

passes through the PCI LOS (in the following referred to as *PCI flux tube*) is drawn in blue and is poloidally shifted with respect to the bean shape flux tube. For illustration purposes, the cross section at $\zeta = \frac{4}{5} \times 2\pi$ was chosen for the bean shape flux tube, which is toroidally shifted but geometrically identical to the more commonly used $\alpha = 0$ flux tube at the $\zeta = 0$ bean shaped cross section.

A nonlinear gyrokinetic simulation with GENE was carried out for a direct comparison of the two flux tubes with gyrokinetic treatment of both electrons and ions, and without collisions or magnetic perturbations. The gradient lengths for the ion temperature, electron temperature and density were taken from experiment data during a discharge with the same magnetic configuration. Figure 4.7 shows the density fluctuations from the simulation along the two flux tubes. The simulated flux tube makes one complete toroidal turn, while figure 4.6 only shows a certain section of it. The $\hat{z} = 0$ position of each flux tube is marked by a vertical line of the respective colour in figure 4.6. As expected, the bean shape flux tube exhibits the strongest fluctuations at the outboard mid-plane ($\hat{z} = 0$), where the curvature is most unfavourable. The PCI flux tube exhibits the strongest fluctuations

not at $\hat{z} = 0$, but where it passes through the region of strong unfavourable curvature close to the bean shape. Consequently, the density fluctuations peak close to $\hat{z} = 0$ in both positive and negative \hat{z} direction, which corresponds to the read area on the left hand side end and at the bean shape in figure 4.6. In both flux tubes, the density fluctuations decrease towards the inboard side and are overall on the same order of magnitude. The LOS of the PCI diagnostic probes the flux tube close to the point of strongest and weakest fluctuations on the outboard and inboard side, respectively. Generally, the PCI measurements can be considered a good representation of the fluctuation levels in W7-X, i. e. it is not expected that flux tubes or regions exist with significantly stronger fluctuations than the ones captured by PCI.

The previous discussions show that a comparison of experiment and simulation is often indirect and complicated for PCI. The only way to directly compare theoretical expectations from gyrokinetic simulations to experiment data is by modelling the PCI signal numerically. For this purpose, the whole PCI system as described in this section has also been implemented as a synthetic PCI (SPCI) diagnostic [139] following previous work for DIII-D and Alcator C-Mod [140]. The SPCI diagnostic calculates the phase contrast signal numerically based on density fluctuations from arbitrary sources, e. g. global gyrokinetic simulations. It includes the effects of optic elements such as finite aperture and the phase plate as well as the detector frequency response functions and even the sound wave calibration. Besides modelling the PCI signal for simulation results, the SPCI can also be used for investigations with simple models for e. g. plasma rotation or magnetohydrodynamic (MHD) modes [139]. Due to the line-integrated nature of the measurement, it is difficult to estimate the effect of these phenomena on the PCI data without a rigorous treatment by SPCI.

4.2 Data analysis tools

The aim of this section is to provide all required methods for analysing the data collected by the PCI diagnostic. This includes standard spectral analysis tools as well as diagnostic specific additions. Due to the integrated implementation, the description of standard and diagnostic specific methods is not separated. The general spectral analysis tools are introduced in

detail with the clear aim for PCI data with diagnostic specific additions at the appropriate places. The data output of the PCI diagnostic consists of 32 channel signals per detector with $f_s = 2$ MHz sampling rate. The data evaluation must take into account the detector frequency response, the magnification of the optical system, which affects the wavenumber measurement, as well as the laser beam profile and amplitude. Sections 4.2.1 to 4.2.3 describe the integrated spectral analysis of PCI data. In sections 4.2.4 and 4.2.5, two methods are described which were developed or adapted to the PCI diagnostic of W7-X within the framework of this project. Section 4.2.6 briefly introduces the standard tools for cross-correlation analysis of two separate signals.

4.2.1 Power spectral density

The PCI signal consists of a continuous, fluctuating time series for each of the 32 channels per detector. The appropriate quantity for a spectral analysis of this type of data is the power spectral density (PSD), which describes how the power of the signal is distributed in frequency space. One of the most common methods to estimate the PSD based on discrete signal data are *modified periodograms*. Let $x(n)$, $n = 1, \dots, N$ be a sample of a PCI channel signal with length N . As for most methods, the base of the analysis is a discrete Fourier transform (DFT) of the signal, where both the time as well as the frequency variable take only discrete values [141, 142],

$$\mathbf{DFT}\{x(n)\}(l) \equiv X(l) = \sum_{n=1}^N x(n)e^{-\frac{i2\pi}{N}nl}. \quad (4.4)$$

In practice, a DFT is calculated using a fast Fourier transform (FFT) algorithm [141]. A periodogram is calculated as

$$I(f_l) = \frac{1}{N} |X(l)|^2, \quad (4.5)$$

with the (dimensionless) frequency $f_l = \frac{l}{N}$, $l = 0, \dots, N/2$. This simple periodogram is not a good estimate of the PSD, however, since the variance of the spectrum is large and does not decrease with increasing sample size [142]. In order to reduce the spectral bias which is introduced by a finite

size data segment, a Hann window function is multiplied to the data sample before the DFT:

$$X_m(l) = \sum_{n=1}^N x(n)w(n)e^{-\frac{i2\pi}{N}nl}. \quad (4.6)$$

The window function, $w(n)$, with length N reduces the weight of the data at the ends of the segment. The modified periodogram follows as

$$I_m(f_l) = \frac{1}{N}|X_m(l)|^2/U \quad (4.7)$$

$$= |X_m(l)|^2 / \sum_{n=1}^N |w(n)|^2, \quad (4.8)$$

where $U = \frac{1}{N} \sum_{n=1}^N |w(n)|^2$ denotes the power in the temporal window. The effect on the PSD by a Hann window is less severe than that of a rectangular window, which is effectively used by selecting a finite length data segment. A method to further reduce the variance in the PSD is to average over modified periodograms of overlapping subsequences of the data sample, which is called *Welch's method* [143]. Let the subsequences be of length L and D units apart, such that $x_r(j) = x(j + (r - 1)D)$, with $j = 1, \dots, L$ and $r = 1, \dots, K$, where K is the total number of subsequences. A modified periodogram, $I_r(f)$, is calculated for each subsequence and the final estimate of the PSD is given by

$$\mathbf{PSD}\{x_{\text{ch}}(n)\}(f) \equiv S_{xx}(f) \approx \frac{1}{K} \sum_{r=1}^K I_r(f), \quad (4.9)$$

with the dimensional frequency $f = f_l f_s$. Welch's method has been shown to significantly reduce the variance of the estimated PSD [142, 143]. Even though the segments overlap, they are not strongly correlated, since the data samples at the ends of the segment have less weight due to the applied window function.

Detector frequency response

Each detector channel has a characteristic amplitude response across the frequency spectrum. It can be parametrised as a function, $H_{\text{ch}}(f)$, with a

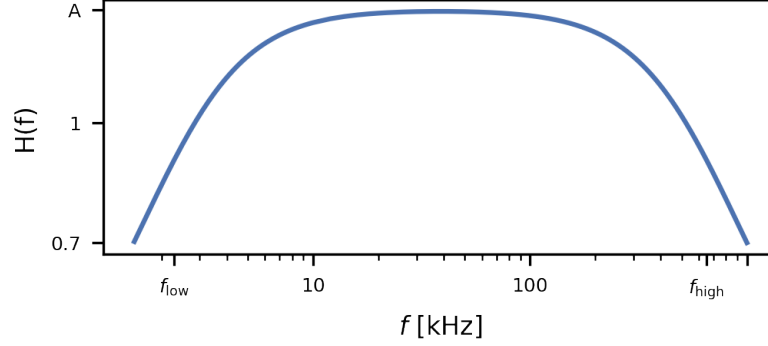


Figure 4.8: Example of a frequency response function of a detector channel.

lower and upper cutoff frequency and amplitude, A_{ch} , [113]

$$H_{\text{ch}}(f) = A_{\text{ch}} \left[1 + \left(\frac{f_{\text{low}}}{f} \right)^2 \right]^{-\frac{1}{2}} \left[1 + \left(\frac{f}{f_{\text{high}}} \right)^2 \right]^{-\frac{1}{2}}. \quad (4.10)$$

Figure 4.8 shows an example of such a response function for a specific detector channel fitted to measured calibration data. The lower and upper cutoff frequencies set the frequency range which can be observed by PCI, $f \approx 1$ to 1000 kHz. In order to compensate for the amplitude decrease close to the cutoff frequencies, the estimated PSD of each channel is divided by the respective squared amplitude response function. The magnitude of the PSD should on average not be affected where $H(f)$ is flat, but different amplitude responses between detector channels should be accounted for. Therefore, the response function is normalised by the mean amplitude parameter of the detector array,

$$A_{\text{mean}} = \frac{1}{32} \sum_{\text{ch}=1}^{32} A_{\text{ch}}.$$

Finally, the calibrated PSD of a specific channel is given by

$$S_{\text{ch}}^{\text{cal}}(f) = S_{xx}(f) \left(\frac{A_{\text{mean}}}{H_{\text{ch}}(f)} \right)^2. \quad (4.11)$$

4.2.2 Spectrogram

The turbulence in the plasma is expected to change during a discharge and accordingly the spectral properties of the density fluctuations, which can be illustrated with a spectrogram. The time series of a data stream is divided into (possibly overlapping) subsegments, similarly to Welch's method. A window of length L is moved to the position τ in the time series and a DFT is calculated for the windowed subsegment. This is called a short-time Fourier transform (STFT) [141],

$$\mathbf{STFT}\{x(n)\}(f_l, \tau) \equiv X(f_l, \tau) = \sum_{n=\tau}^{\tau+L} x(n + \tau)w(n)e^{-i2\pi f_l n}. \quad (4.12)$$

A spectrogram represents the PSD and is given by the magnitude squared of the STFT:

$$\text{spectrogram}\{x(n)\}(f_l, \tau) \equiv \frac{1}{LU}|X(f_l, \tau)|^2, \quad (4.13)$$

where U is the power of the window function. Welch's method can be applied here as well by averaging over several modified periodograms for one time point, which reduces the temporal resolution but also the variance of the spectrum.

4.2.3 Simultaneous Wavenumber-Frequency Analysis

One of the largest assets of the PCI diagnostic is the simultaneous spatial and temporal measurement of density fluctuations. In order to take advantage of this feature, a dual Fourier transform (FT) is performed on the data, $x_{\text{ch}}(t)$, $\text{ch} = 1, \dots, 32$, resulting in a wavenumber-frequency ((k, f))-spectrum, which directly shows the spectral properties of the density fluctuations in the plasma. As the first step, the calibrated DFT in time is calculated for each channel according to equations (4.6) and (4.11),

$$X_{\text{ch}}^{\text{cal}}(f_l) = X_{\text{ch,m}}(f_l) \frac{A_{\text{mean}}}{H_{\text{ch}}(f)} \quad (4.14)$$

Now the spatial FT can be performed. A Hann window function with the width of the detector array is multiplied to $\{X_{\text{ch}}^{\text{cal}}(f_l)\}$ in order to reduce

spectral bias. The DFT is then performed along the spatial axis of the detector channels for every frequency bin:

$$X(k_m, f_l) = \sum_{\text{ch}=1}^{32} X_{\text{ch}}^{\text{cal}}(f_l) w(\text{ch}) e^{-\frac{i2\pi}{32} \text{ch} m} \quad (4.15)$$

$$= \frac{A_{\text{mean}}}{H_{\text{ch}}(f)} \sum_{\text{ch}=1}^{32} \sum_{n=1}^N x_{\text{ch}}(n) w(n) w(\text{ch}) e^{-i2\pi(n f_l + \text{ch} k_m)}, \quad (4.16)$$

where $k_m = \frac{m}{32}$ is the dimensionless wavenumber. Finally, the 2-dimensional PSD is estimated as a modified periodogram,

$$S_{xx}(k_m, f_l) = \frac{1}{32N} \frac{|X(k_m, f_l)|^2}{U_t U_{\text{ch}}}. \quad (4.17)$$

with the power of the temporal window function and the power of the spatial window function,

$$U_t = \frac{1}{N} \sum_{n=1}^N |w(n)|^2, \quad U_{\text{ch}} = \frac{1}{32} \sum_{\text{ch}=1}^{32} |w(\text{ch}) w_{\text{Gauss}}(\text{ch})|^2.$$

For the latter, not only the applied Hann window function, $w(\text{ch})$, is considered, but also the Gaussian window that is additionally applied by the laser beam amplitude profile, $w_{\text{Gauss}}(\text{ch})$. The laser beam amplitude profile is determined from the sound wave measurement and can be understood as an additional window function that gives more weight to the channels close to the centre of the laser beam. Figure 4.9 shows an example colour plot of $S_{xx}(k, f)$, which in this work is called a (k, f) -spectrum, calculated from output of the SPCI diagnostic. Contrary to the frequency axis, the wavenumber axis has both positive and negative values. The sign of k represents the propagation direction with respect to the direction along which the FFT was performed. If a mode propagates from small channel number to large channel number, it appears on the positive wavenumber branch and vice versa. A dominant phase velocity, i. e. a slope with particularly high spectral power, is generally observed and will be further discussed in sections 4.2.4 and 5.1 and chapter 6.

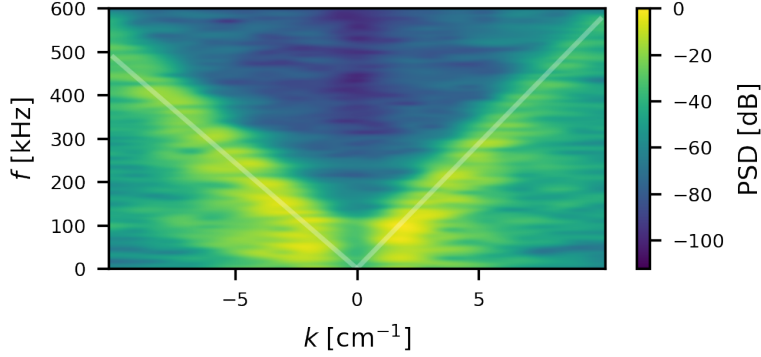


Figure 4.9: Typical wavenumber-frequency-spectrum generated from synthetic PCI output.

Wavenumber calibration via sound wave measurement

In figure 4.9, the dimensional frequency, $f = f_l f_s$, and the dimensional wavenumber, k , are shown. The magnitude of k is determined by the sampling frequency in space, which is set by the distance between the channel signals, Δ_{ch} . Since the quantity of interest is the wavenumber as it appears in the plasma and not as it is imaged on the detector, one should consider the distance between the LOSs in the plasma, Δ_{LOS} , rather than between the elements of the detector array, Δ_{det} . Δ_{LOS} depends on the variable magnification of the optical system on the receiving side of the diagnostic and the fixed Δ_{det} . As described in section 4.1.2, the magnification is set by the OAP mirrors and the variable telescope in front of detector. Given the settings of the telescope, the magnification is known in advance. Additionally, the exact magnification can be measured using the sound wave signal before every discharge. For this calibration of the wavenumber axis, a (k, f) -spectrum of the sound wave signal is calculated as described above. Initially, Δ_{ch} is chosen to be the distance between the elements of the detector array. Accordingly, the resulting wavenumber corresponds to the image on the detector. Figure 4.10 shows the (k, f) -spectrum of a sound wave measurement together with the wavenumber spectrum at the frequency of the sound wave, $S_{xx}(k, f = f_{\text{sw}})$. Only one clear spot of high PSD is visible, which is the forward sound wave. Great care has been taken to avoid

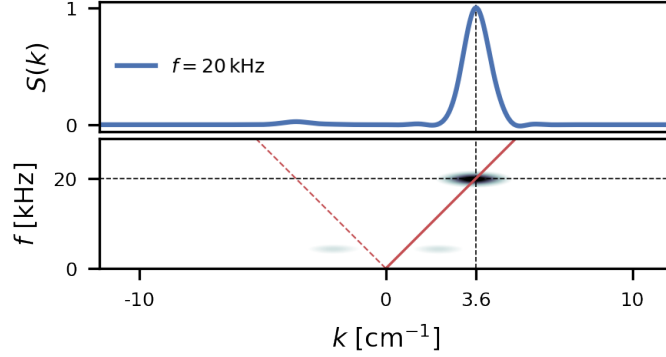


Figure 4.10: Wavenumber spectrum at 20 kHz and full wavenumber-frequency-spectrum of a sound wave measurement.

a strong reflected sound wave by including sound absorbing material in the mirror box, where the sound speaker is installed, as well as choosing a time window shortly after the launch of the sound wave, where no reflected wave as reached the laser beam, yet. The sound wave wavenumber as imaged on the detector, $k_{\text{sw}}^{\text{det}}$, is measured by taking the maximum position of $S_{xx}(k, f = f_{\text{sw}})$. The resolution is improved by cubic spline interpolation. The actual wavenumber of the sound wave is known, assuming the typical sound speed at room temperature, $k_{\text{sw}} = 2\pi f_{\text{sw}}/c_s$. The magnification of the optical system, M , is then given by the ratio of the real and the imaged wavenumber of the sound wave. The wavenumbers of the fluctuations in the plasma can be directly calculated by using the spacing between the LOSs

$$\Delta_{\text{LOS}} = M\Delta_{\text{det}}, \quad M = k_{\text{sw}}^{\text{det}}/k_{\text{sw}}. \quad (4.18)$$

With the right spacing between channel signals, the appropriate wavenumber can be calculated, $k = k_m/\Delta_{\text{LOS}}$. This method has been implemented for all experiment discharges of W7-X. The magnification as determined from the sound wave measurement agrees well with the expected value from the telescope settings and has a small variance over a period of time with unchanged telescope settings, $\sigma_M/M \approx 2\%$.

It is worthwhile discussing the interpretation of the calibrated wavenumber in the context of the expected wavenumbers of drift wave turbulence. As described in section 3.2, drift waves have an elongated structure which

is aligned with the magnetic field lines on a flux surface and propagate in the binormal direction, $\mathbf{k}_{\text{dw}} = k_{\text{dw}} \hat{\mathbf{e}}_{\alpha}$, with $\hat{\mathbf{e}}_{\alpha} = \nabla\alpha/|\nabla\alpha| = \hat{\mathbf{n}} \times \hat{\mathbf{b}}$. PCI measures the projection of the wave onto the measurement direction, which is expressed by the unit vector $\hat{\mathbf{e}}_{\text{m}}$:

$$\lambda = \lambda_{\text{dw}} \hat{\mathbf{e}}_{\alpha} \cdot \hat{\mathbf{e}}_{\text{m}} = \lambda_{\text{dw}} \cos \theta, \quad (4.19)$$

where λ and λ_{dw} are the measured wavelength and the drift wave wavelength, respectively, and $\theta = \angle(\hat{\mathbf{e}}_{\text{m}}, \hat{\mathbf{e}}_{\alpha})$ is the angle between the measurement direction of PCI and the binormal direction. For the measured wavenumber follows

$$k = k_{\text{dw}} / \cos \theta. \quad (4.20)$$

The measurement direction is fixed along the LOS (see section 4.1.2), whereas the binormal direction changes, since both the pitch angle of the magnetic field as well as the angle between the LOS and the flux-surface normal change. The projection, $\cos \theta$, is therefore dependent on the location along the LOS. Due to the line-integrated measurement of PCI and the missing radial information, it is difficult to correct for this projection in advance. It is therefore a priori only possible to investigate the wavenumber as measured by PCI but it should be kept in mind that the real wavenumber of the drift wave turbulence can be different and depends on the radial position of the drift wave.

4.2.4 Determination of dominant phase velocities

The dominant phase velocity in the (k, f) -spectrum measured by PCI as mentioned before is clearly visible by eye (see e. g. figure 4.9) but not strictly a physical quantity in the sense that it represents a specific plasma parameter. Its definition therefore somewhat arbitrary. Nevertheless, a reliable method for determining a dominant phase velocity is needed for a consistent analysis of its origin. This method also needs to be flexible enough to be adapted to the requirements of various situations.

The dominant phase velocity is defined here as the slope in the (k, f) -spectrum, which is the maximum of the distribution of local maxima in the wavenumber spectrum. The flexibility of this definition lies in the way the local maxima are selected and how their distribution is estimated. In

order to determine the local maxima, the wavenumber spectrum at each frequency is interpolated via cubic-spline interpolation. The maxima of the spline interpolation are selected if they are above a certain threshold. The threshold, s_{thr} , is defined as a fraction of the maximum spectral density, $\max[s(k)]$.

Figure 4.11a shows a (k, f) -spectrum with green markers at the position of local maxima. In the next step, these maxima are ordered by their corresponding phase velocity assuming a simple linear dispersion relation, $v_{\text{ph}} = 2\pi f/k$. In order to determine the centre of the distribution of maxima, a Gaussian kernel density estimate (KDE) [144, 145] is calculated. A KDE, which is also termed the Parzen–Rosenblatt window method, is a tool to estimate the underlying probability density function of a random variable, x , based on a set of samples of this variable. This is done by summing over kernels, $K(x)$, of a given bandwidth, h , at each sample value, X_j . The probability density function estimate based on a set of n samples is then given by [145]

$$f_n(x) = \frac{1}{nh} \sum_{j=1}^n K\left(\frac{x - X_j}{h}\right). \quad (4.21)$$

Additionally, each sample (and Kernel) can be individually weighted, taking into account measurement uncertainties. In case of the determination of the dominant phase velocity, the random variable, x , is the phase velocity of the local maxima in the spectrum and each sample is weighted equally. The phase velocities are assumed to follow some non-trivial distribution, which is not known in advance. This is the reason why a non-parametric method such as the KDE is a suitable tool. $K(x)$ is chosen to be a Gaussian function and h is chosen on a case by case basis to best fit the purpose of the v_{ph} determination. Figure 4.11b the phase velocity values of the local maxima (the samples) as vertical green lines on the x -axis, which correspond to the green markers in figure 4.11a. The resulting KDE is displayed in red and shows two major modes, which represent the positive and negative dominant phase velocity, respectively. The maximum position of each mode is finally taken as the dominant phase velocity in the spectrum. The white lines in figure 4.11a represent the dominant phase velocities determined in the KDE. There are two free parameters in this method: the threshold for selecting local maxima in the wavenumber spectra, s_{thr} , and the kernel width, h , in

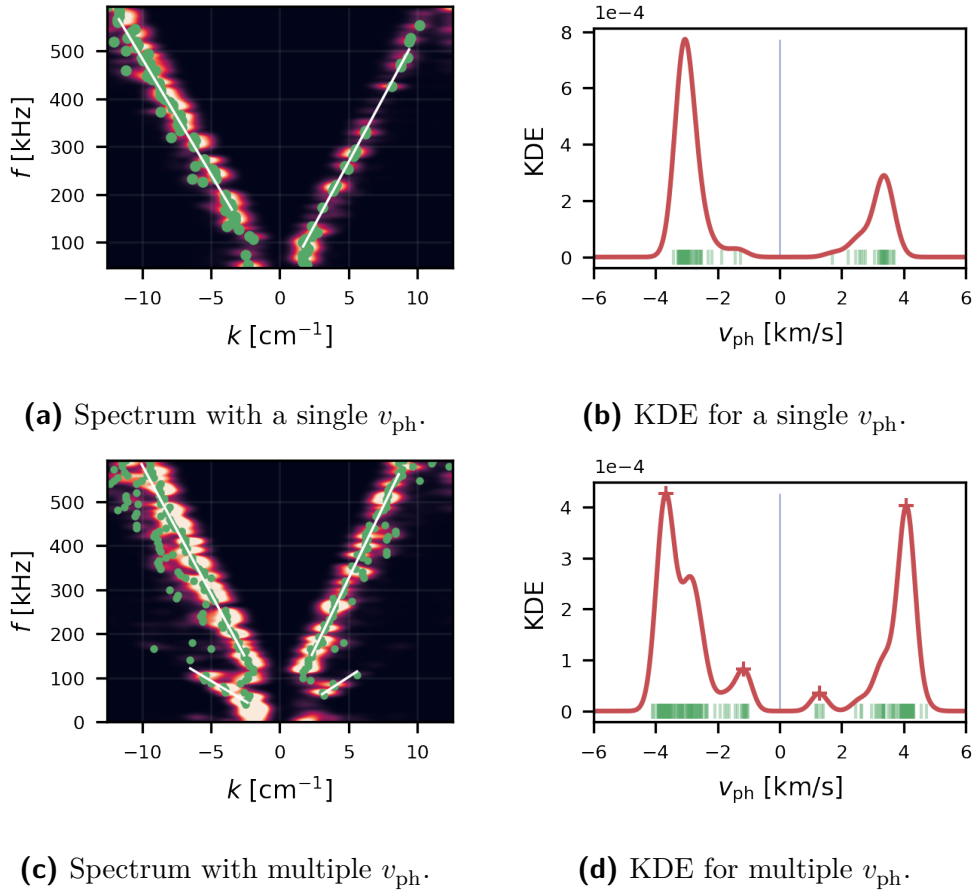


Figure 4.11: Wavenumber-frequency-spectra (a & c) with local maxima of the wavenumber spectra (green markers) and the determined phase velocities (white lines) and KDE (b & d) as used for its determination. Figures (a) and (b) show a case with one v_{ph} per wavenumber branch and figures (c) and (d) show a case with multiple v_{ph} and a multimodal KDE.

the KDE. The former acts as a sensitivity parameter for sampling the phase velocities in the spectrum and the latter acts as a smoothing parameter for the KDE. In the simple case of one obvious dominant phase velocity per wavenumber branch, the determined velocity is largely insensitive to the exact choice of parameters, but there are advantages to certain parameter choices. Setting a rather large threshold value and kernel width makes the method less sensitive to noise in the data and transient features, such as MHD modes or other coherent modes. This is particularly useful for a robust automatic determination of the dominant phase velocity throughout the discharge. However, there are situations with multiple visible velocity bands in the (k, f) -spectrum or an asymmetric distribution of spectral power along the apparent dominant phase velocity. In these cases, it is useful to choose a rather small threshold for the local maxima and a narrower kernel width, in order to have enough samples and the appropriate smoothing to show the desired features in the KDE. Figures 4.11c and 4.11d show the (k, f) -spectrum and the KDE for the case of multiple visible phase velocity bands. The smaller threshold, s_{thr} , results in a larger number of maxima (green markers) and a narrower kernel width results in a multimodal distribution, which can resolve the multiple dominant phase velocities that are visible by eye. The maxima of the modes in figure 4.11d that are accepted by the method, are marked with a +. In order to reject maxima in the KDE that do not reflect a dominant phase velocity in the (k, f) -spectrum, another threshold is introduced. The height of the maximum with respect to the closest minimum is measured and has to be larger than a the threshold value. In other words, a maximum in the KDE is only considered a separate mode of the distribution if it is high enough and well isolated from other modes.

4.2.5 Calibrated absolute density fluctuation amplitude

The absolute magnitude of the line-integrated density fluctuations is a useful quantity, which can be obtained from the PCI signal with a calibration on the basis of the sound wave measurement. In addition to the magnitude of the density fluctuations, the measured signal amplitude is affected by the optical system magnification, the alignment and the laser power. The diagnostic effects can change over the course of an experiment day, but are assumed to be constant for the duration of a discharge, which justifies

a single calibration before every discharge. The sound wave measurement accounts for all technical effects and can be used for a relative amplitude calibration. Fluctuation amplitudes from different discharges can then directly be compared to each other. Furthermore, by measuring the pressure fluctuation amplitudes of the sound wave, an absolute value for $\int \tilde{n} dl$ can be obtained. In the remainder of this section, the details of the relative and absolute amplitude calibration are described, as well as the calculation of an absolute line-integrated density fluctuation amplitude from a signal during a discharge.

For the amplitude calibration, a time window of 0.5 ms starting 0.75 ms after the launch of the sound wave is analysed. The starting and end points of the time window are marked by vertical black lines in figure 4.4. The sound wave has reached all LOSs 0.75 ms after the speaker starts emitting. A reflected wave reaches the LOSs 0.5 ms later and creates a standing wave pattern, which is visible in the amplitude profile across the detector array. Since an unperturbed amplitude profile is important for a reliable calibration, the time window between the arrival of the sound wave and the arrival of the reflected wave was chosen for the analysis. The PSD of this time window is estimated as described in section 4.2.1 for each channel. The amplitude of the sound wave signal can then be estimated by integration of the PSD,

$$\hat{A} = \sqrt{2 \int_{f_1}^{f_2} S(f) df}. \quad (4.22)$$

The factor two accounts for the fact that $S(f)$ is calculated at a one-sided spectrum. The integration boundaries are chosen to be a narrow range around the sound wave frequency, $f_{\text{sw}} \pm 4 \text{ kHz}$, in order to avoid contributions of electric noise. Calculating \hat{A} for every channel produces an amplitude profile of the sound wave measurement, which is shown in the upper panel of figure 4.12. The markers represent the measured value of \hat{A} and the continuous lines are Gaussian functions fitted to the data. Since the amplitude of the sound wave can be assumed to be more or less constant across the laser beam, the profile mainly reflects the Gaussian laser beam profile as imaged on the detector. A strong deviation from the Gaussian shape is an indicator for unwanted optical artefacts due to misalignment or electrical issues in certain channel signals. Therefore, the coefficient of determination, R^2 , as a measure of how well a Gaussian model predicts

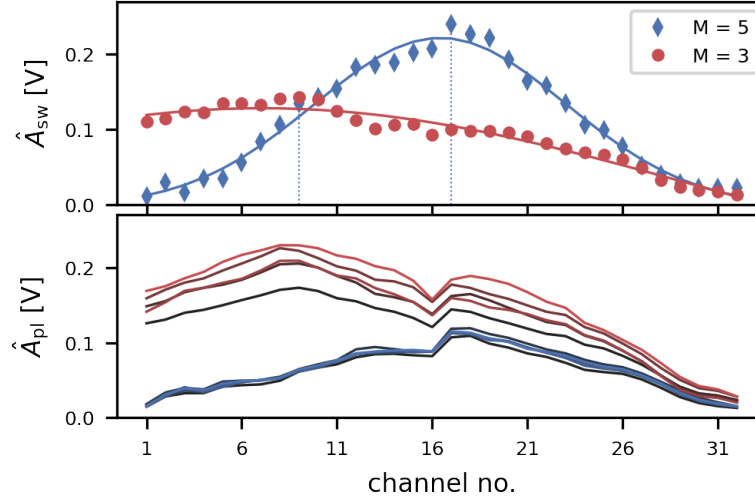


Figure 4.12: Gaussian laser beam profiles on the detector array determined from sound wave measurements (upper panel) and density fluctuation measurements during plasma discharges (lower panel). The sound wave measurement is represented by markers and a Gaussian function fitted to the data is shown as a solid line. Two cases with net magnification $M = 5$ (blue) and $M = 3$ (red) are shown. For each case, five time points during the plasma discharge were used to obtain a profile (increasing luminance of the colours).

the measured data, can be used for a quantitative test of the beam shape quality. Measurements with a bad beam shape ($R^2 < 0.8$) are rejected for calibration, since it is usually not possible to identify the exact reason for the distorted profile and it is therefore also not possible to estimate the error introduced by it. In the two cases shown in figure 4.12, the optical system had a net magnification of $M = 5$ (blue) and $M = 3$ (red), respectively. Decreasing the magnification causes the profile width to increase and the maximum amplitude to decrease, as the laser spot at the detector becomes wider and the power density of the laser beam decreases. Additionally, the centre of the Gaussian profile is shifted towards a lower channel number, which is not due to the different magnification but due to a change in the alignment. The sound wave measurement is only a good reference, if it represents the profile during the plasma discharge well. This is usually

the case, even if the profile shape slightly deviates from a Gaussian shape. The profiles in the lower panel of figure 4.12 from measurements during the discharge match the respective profile obtained from the sound wave measurement fairly well with respect to the profile shape. The profiles are calculated according to equation (4.22) but with integration boundaries set to $f_1 = 20$ kHz and $f_2 = 600$ kHz, spanning a frequency range which is relevant for ion-scale fluctuations while avoiding electric noise at very low and very high frequencies. The channel with the highest illumination, i. e. the channel with the maximum amplitude, ch_{max} , is chosen as a reference for the calibration. It can be assumed to have the highest illumination during the plasma discharge as well and therefore the best signal-to-noise ratio. In figure 4.12, the selected channels are marked by vertical dotted lines in the upper panel. The respective amplitude, $\hat{A}(\text{ch}_{\text{max}})$, is the reference value for the calibration of the signal amplitude.

For the calibration of the absolute fluctuation amplitude, the signal amplitude needs to be associated with an electron density fluctuation amplitude. The phase shift of the laser which is induced by the pressure fluctuation of the sound wave, \tilde{p}_{sw} , can be related to an analogous electron density fluctuation, \tilde{n}_e , via [125]

$$\int \tilde{n}_e dl = \frac{2\pi(N_0 - 1)}{\lambda_L^2 r_e \gamma p_0} \int \tilde{p}_{\text{sw}} dl \equiv \Pi_{\text{sw}}, \quad (4.23)$$

where N_0 is the reference refractive index at the reference air pressure, p_0 . λ_L is the wavelength of the laser, r_e is the classical electron radius, and γ is the heat capacity ratio. The line-integrated pressure fluctuation of the sound wave is determined by integration of the sound field at the height of the centre of the laser beam (see figure 4.5). As described in section 4.1.2, the value of the laterally line-integrated pressure fluctuations decreases linearly with increasing height, h , above the speaker. The value at the height of the central LOS, h_c , corresponds to the phase contrast signal of ch_{max} , when the laser is properly aligned.

In order to obtain a value for the absolute amplitude of the line-integrated density fluctuations during a plasma discharge, the signal ch_{max} is used to estimate the signal amplitude according to equation (4.22) with fixed integration boundaries (e. g. 20 to 600 kHz). The corresponding line-integrated

density fluctuation amplitude is then given by

$$\int \tilde{n}_e dl \Big|_{f_1 \leq f \leq f_2} = \hat{A}_{\text{pl}} \Big|_{f_1 \leq f \leq f_2} \frac{\Pi_{\text{sw}}}{\hat{A}_{\text{sw}}}, \quad (4.24)$$

where \hat{A}_{pl} is the signal amplitude during the discharge and \hat{A}_{sw} is that of the sound wave measurement. For a valid comparison of plasma fluctuation amplitudes, it is important to use the same frequency range for integration. Furthermore, the comparison might be marred by electric noise within that frequency range, which can significantly affect the fluctuation amplitude. The data should therefore be inspected for abnormalities before calculating the absolute density fluctuation amplitude.

In the remainder of this section, the measurement error of the absolute line-integrated density fluctuation amplitude is discussed. Several sources of systematic errors need to be considered for its estimation. The error of the sound wave signal amplitude, \hat{A}_{sw} , is negligible. When calculating the signal amplitude of the plasma density fluctuations, \hat{A}_{pl} , an error is introduced if the amplitude profile differs from that of the sound wave measurement and the selected channel is not at the maximum position of the amplitude profile. This error is estimated to be the difference of the signal amplitude of the selected sound wave channel to the profile maximum of the plasma measurement,

$$\sigma_{\hat{A}_{\text{pl}}} \approx \Delta \hat{A} = \left| \hat{A}_{\text{pl}}(\text{ch}_{\text{max,sw}}) - \hat{A}_{\text{pl}}(\text{ch}_{\text{max,pl}}) \right|. \quad (4.25)$$

Next, the error of the reference value for the line-integrated density fluctuation, Π_{sw} , is dominated by the error of the line-integrated pressure fluctuation measurement. This contribution can be reduced to an error of the height, h , that is chosen for the line-integration of \tilde{p} in . The values for h in the measurement of the sound field above the speaker (see figure 4.5) have an estimated uncertainty of ± 5 mm. The height of the laser beam above the speaker can slightly vary due to changes in the alignment and has an additional uncertainty of ± 5 mm. If the amplitude profile shape diverges from the Gaussian shape, this can introduce an additional error: if the maximum channel is not at the centre of the Gaussian beam, choosing the central LOS for the line-integration is not appropriate. The centre of the Gaussian beam, ch_c , is estimated by fitting a Gaussian function to the amplitude profile as

illustrated in figure 4.12. The combined error of h is then given by

$$\sigma_h^2 \approx 2 (5 \text{ mm})^2 + \left(\frac{D |\text{ch}_{\text{max}} - \text{ch}_c|}{w_{\text{Gauss}}} \right)^2, \quad (4.26)$$

where the difference between ch_{max} and ch_c is multiplied by the width of the laser beam above the speaker, D , which is set by the telescope on the laser optical table, and the width of the Gaussian fit in channel numbers, w_{Gauss} , in order to translate into a deviation of h above the speaker. The total error of the line-integrated density fluctuation measurement is finally:

$$\sigma = \sqrt{\frac{\sigma_{\hat{A}_{\text{pl}}}^2}{\hat{A}_{\text{pl}}^2} + \frac{\sigma_h^2}{h^2}} \int \tilde{n}_e dl. \quad (4.27)$$

All other contributions such as the microphone sensitivity, the uncertainty of the constants in equation (4.23) and the error of the sound wave signal amplitude introduced by the speaker are negligible compared to the sources discussed above.

The analysis for the absolute amplitude calibration as described in this section was developed as part of this work. It enables an automatic calibration and calculation of density fluctuation, which was applied to all data collected during the latest experiment campaign. Besides the database of raw signals, a database of absolute density fluctuation amplitudes now exists for all experiments with (successful) sound wave calibration.

4.2.6 Cross-correlation analysis

In the last section of this chapter, basic tools for the cross-correlation of two signals are described. This is important for the correlation of two turbulence-relevant quantities, but also for the evaluation of the coherence of the fluctuations by comparing different channel signals of PCI.

The auto-correlation function of wide-sense stationary stochastic signals is defined as [141, 142]

$$R_{xx}(m) = \text{E}[x(n) \overline{x(n+m)}] = \lim_{N \rightarrow \infty} \frac{1}{N} \sum_{n=1}^N x(n) \overline{x(n+m)} \quad (4.28)$$

where $E[\dots]$ is the expected value operator, the overline denotes the complex conjugate and the signal is assumed to be ergodic for the second equality. Similarly, a cross-correlation function can be defined for two signals, $x(n)$ and $y(n)$, as

$$R_{xy}(m) = \lim_{N \rightarrow \infty} \frac{1}{N} \sum_{n=1}^N x(n) \overline{y(n+m)}. \quad (4.29)$$

The free variable, m , can be transformed to a time lag, $\tau = m/f_s$, where f_s is the sampling frequency.

The cross power spectral density (CSD) of the two signals, $x(n)$ and $y(n)$, is a measure of the spectral power that is shared between them [142]. It can be defined similarly to the PSD (see equation (4.7)):

$$S_{xy}(f) = \frac{1}{NU} \overline{X_m(f)} Y_m(f), \quad (4.30)$$

where $X_m(f)$ and $Y_m(f)$ are the DFTs of windowed data segments of $x(n)$ and $y(n)$ with length N and U is the spectral power of the window. The variance of S_{xy} can be improved by averaging several CSD of overlapping time segments, similar to Welch's method in equation (4.9). While S_{xx} is always a real number, S_{xy} is generally a complex number. The magnitude of the CSD is therefore given by the absolute value $|S_{xy}|$, whereas $\arg(S_{xy})$ denotes the cross-phase between x and y .

While this method is used in practice for this work, the PSD and CSD can also be calculated as the DFT of the auto- and cross-correlation function. This is called the Blackman-Tukey method [146] and makes use of the Wiener-Khinchin theorem [147]:

$$\bar{S}_M(f) = \int_{-M}^M \bar{R}_T(\tau) e^{-i2\pi f\tau} d\tau, \quad (4.31)$$

$$\bar{R}_T(\tau) = \frac{1}{T} \int_0^T x(t)x(t+\tau)dt \quad \text{for } |\tau| \leq M \ll T, \quad (4.32)$$

where $\bar{S}_M(f)$ is the power spectrum of signal $x(t)$ and $\bar{R}_T(\tau)$ is the auto-correlation or auto-covariance function of $x(t)$. For discrete signals, the PSD

and CSD can accordingly be estimated as

$$S_{xx}(f) = \frac{1}{M} \sum_{m=-M}^M R_{xx}(m)e^{-i2\pi fm}, \quad (4.33)$$

$$S_{xy}(f) = \frac{1}{M} \sum_{m=-M}^M R_{xy}(m)e^{-i2\pi fm}, \quad (4.34)$$

respectively. This can also be reversed and $R_{xx}(m)$ and $R_{xy}(m)$ can be obtained by performing an inverse discrete Fourier transform (IDFT) on $S_{xx}(f)$ and $S_{xy}(f)$, respectively. In practice, this is a robust method to calculate the auto- and cross-correlation function, if a good estimate of PSD and CSD is available [105].

The last quantity introduced for corr-correlation analysis is the magnitude-squared coherence [142]:

$$C_{xy}(f) = \frac{|S_{xy}(f)|^2}{S_{xx}(f)S_{yy}(f)}, \quad (4.35)$$

where $S_{xy}(f)$ is the CSD and $S_{xx}(f)$ and $S_{yy}(f)$ are the respective PSDs of the signals $x(t)$ and $y(t)$. It can be understood as a normalised cross power, where $0 < C_{xy} \leq 1$. Contrary to a correlation function, it is frequency resolved. It is a measure of how coherent two signals are at a given frequency, regardless of the spectral power of each signal at that frequency.

5

Characterisation of turbulent density fluctuations

5.1 Turbulent density fluctuation spectra

Turbulent fluctuations are best described by their spectral properties. The first step of this experimental turbulence study is therefore the spectral characterisation of the measured fluctuations. This work focuses on the general case of ECRH plasmas with gas-fuelling, which was the most common type of discharge in the experiments at W7-X so far. The main features of the wavenumber and frequency spectra are presented on an example case of this type of discharge in the following section. The described properties hold true for most experiments and can be regarded as a general feature of the density fluctuations in W7-X.

Figure 5.1 shows the (k, f) -spectrum of a typical ECRH discharge in W7-X standard configuration. The PSD is represented by colour, calibrated frequency and wavenumber are on the vertical and horizontal axis, respectively. The spectrum has a positive and a negative wavenumber branch, which correspond to opposite propagation directions of the fluctuations with respect to the measurement direction. The two branches can be associated with the in- and outboard side of the plasma, which is shown explicitly in chapter 6. The positive wavenumber branch corresponds to the inboard side and vice versa. There is a gap visible between the two branches in the wavenumber range $|k| < 1.6 \text{ cm}^{-1}$. The diagnostic does not produce a phase contrast signal for fluctuations with a smaller wavenumber due to the finite

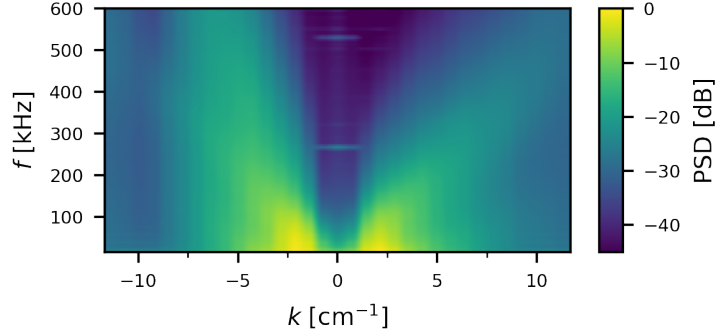


Figure 5.1: Wavenumber-frequency spectrum during an ECRH plasma in W7-X standard configuration (W7-X XP:20180920.036, average over $t = 3$ to 4 s).

width of the central groove of the phase plate (see section 4.1.2). Spectral power in the gap stems from aliasing, spectral leakage, imaging errors or electric noise. Furthermore, phase scintillation due to minor misalignment of the detector with respect to the image plane causes a suppression of the PSD at $|k| \approx 10 \text{ cm}^{-1}$. The PSD is strongest for small wavenumbers and frequencies just outside the central gap and it decreases towards higher frequencies and wavenumbers. Turbulent spectra follow a power-law decay in frequency and wavenumber space (see chapter 3). In order to investigate whether this holds true for the PCI measurements, the individual spectra are calculated by integrating the (k, f) -spectrum, $S_{xx}(k, f)$, along the wavenumber or frequency axis, respectively.

Figure 5.2 shows the frequency spectrum corresponding to the data depicted in figure 5.1. The PSD indeed follows a power-law decay, $S \propto f^{-\alpha}$, where the spectral index, α , changes around $f = 100 \text{ kHz}$. Thin black lines indicate fits to the spectrum in the range of 15 to 100 kHz and 100 to 500 kHz. At lower and higher frequencies, electric noise distorts the signal such that the signal-to-noise ratio (SNR) becomes unacceptable. The qualitative behaviour of the spectrum has previously been described for PCI measurements by BÖTTGER [113] and is as expected for broad band turbulence [14]. The spectral indices can vary between discharges and are found to be lower than what was reported previously for the frequency spectrum of a single detector

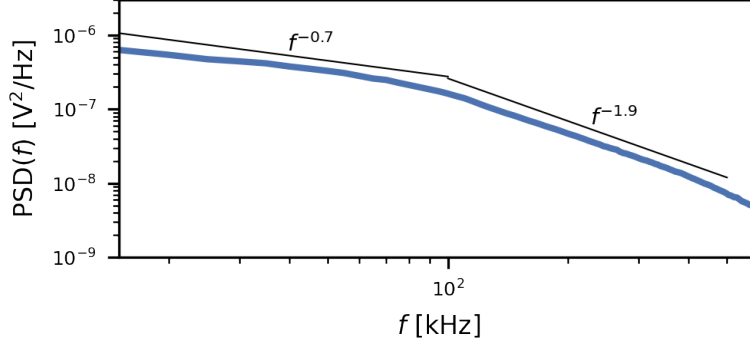


Figure 5.2: Wavenumber-integrated frequency spectrum during an ECRH plasma in W7-X standard configuration with power-law fits.

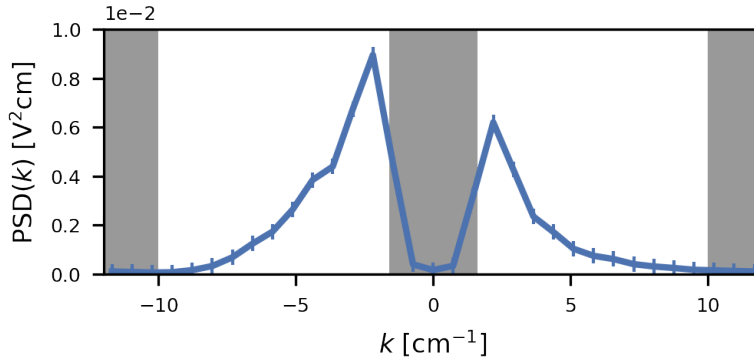
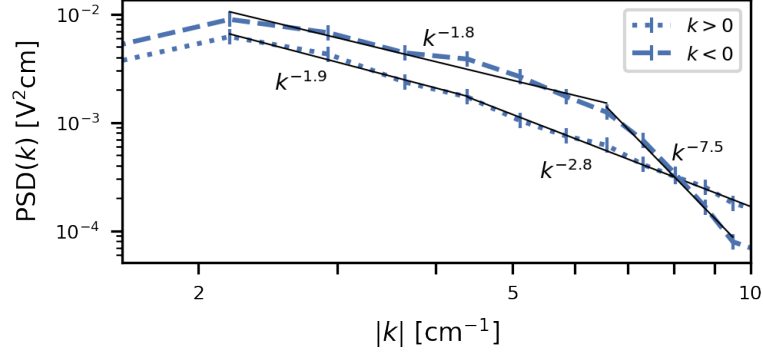


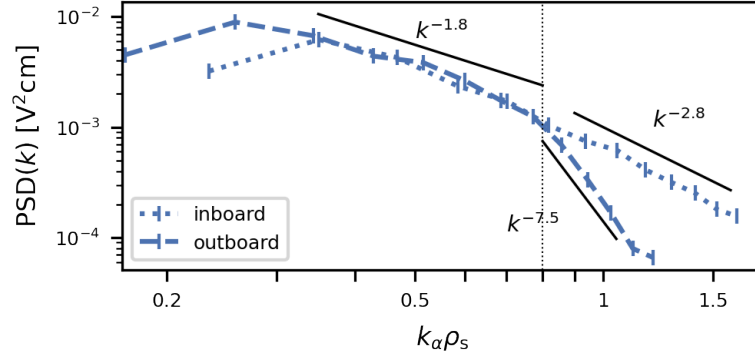
Figure 5.3: Frequency-integrated wavenumber spectrum during an ECRH plasma in W7-X standard configuration. Frequency integration range: 15 to 600 kHz. Grey areas mark wavenumber ranges in which the measurement reduced due to diagnostic limitations and alignment errors.

channel.

In figure 5.3, the frequency-integrated wavenumber spectrum is shown. The 15 to 600 kHz frequency range was chosen for integration in order to avoid the aforementioned electric noise. The wavenumber ranges in which the PSD is suppressed due to diagnostic limitations or alignment errors is greyed out. An asymmetry of power in the negative and positive wavenum-



(a) Wavenumber spectrum in the PCI measurement direction with spectral indices.



(b) Wavenumber spectrum over the normalised binormal wavenumber assuming a radial origin of $r_{\text{eff}}/a = 0.75$.

Figure 5.4: Wavenumber spectrum during an ECRH plasma in W7-X standard configuration with power-law fits. Frequency integration range: 15 to 600 kHz.

ber branch is visible, which can also be seen in figure 5.1 but becomes more obvious in the integrated spectrum. Higher PSD in the negative wavenumber branch corresponds to stronger fluctuations on the outboard side of the plasma. This fits theoretical expectations since the outboard side of the plasma exhibits stronger unfavourable curvature, which excites toroidal ITG modes. Similarly to the frequency spectrum, power-law functions, $S \propto k^{-\alpha}$,

are fitted to the spectrum in figure 5.4a. The spectral index changes at medium wavenumbers. The positive and negative wavenumber branch exhibit similar spectral indices at low k , but for the negative wavenumber branch, α changes at a higher wavenumber and is significantly larger at high k compared to the positive wavenumber branch. Geometric differences between in- and outboard side can explain the asymmetry: as previously discussed in sections 4.1 and 4.2, the wavenumber vector of the fluctuations, which points predominantly in the binormal direction, is in general not parallel to the measurement direction of PCI and a projection of the fluctuations is measured (cf. equation (4.20)). The corresponding binormal wavenumber is given by

$$k_\alpha = k \cos \theta, \quad \theta = \angle(\hat{\mathbf{e}}_m, \hat{\mathbf{e}}_\alpha), \quad (5.1)$$

where θ is the angle between the measurement direction of PCI and the binormal direction. θ is larger on the outboard side, which means that the same $|k|$ corresponds to a smaller k_α on the outboard side than on the inboard side. The projection and the difference between in- and outboard side can be accounted for under the assumption that the fluctuations originate predominantly from a certain radial position in the plasma. Linear gyrokinetic simulation results for the PCI measurement location suggest $r_{\text{eff}}/a = 0.7$, since the growth rates are particularly strong and where the ion temperature gradient in typical temperature profiles is largest at this position. Assuming radial localisation of fluctuations, the drift scale at this position can be used for normalisation of the wavenumber axis. This enables a direct comparison to theoretical expectations. For the geometric correction and the normalisation, a radial location of $r_{\text{eff}}/a = 0.75$ was chosen, where in the example discharge $T_e = T_i = 0.66$ keV and $B = 2.25$ T at the inboard and $B = 2.37$ T at the outboard position along the PCI LOS. The choice of the radial location is further justified by the findings in chapter 6. Due to the varying magnetic field strength, which is stronger on the outboard side than on the inboard side in the W7-X toroidal position where PCI is located (contrary to a tokamak), not only the geometric projection but also the drift scale normalisation is different for in- and outboard side. Figure 5.4b shows the normalised wavenumber spectra of inboard ($k > 0$) and outboard side ($k < 0$). With the given assumptions, the measured spectrum lies mostly within $k_\alpha \rho_s < 1$. In this wavenumber range at the assumed radial position, ITG modes are expected to be the dominant origin of turbulence.

Remarkably, the asymmetry in spectral power between the two branches is compensated by the shift and normalisation of k such that the spectra now are very similar in the range of $k_\alpha \rho_s = 0.35$ to 0.8 . The deviation above and below can be attributed to approaching the low and high wavenumber limitations of the spectrum.

A quantitative comparison of spectral indices to theoretical expectations was attempted for wavenumber spectra by SPCI based on gyrokinetic simulations [139], but seems rather difficult for experimental PCI spectra. The wavenumber at which the spectral index changes is similar for inboard and outboard branch after normalisation at $k_\alpha \rho_s \approx 0.8$. In the dual cascade picture, this corresponds to the energy injection scale, which fits the assumption of ITG modes being dominant, since their growth rate peaks at a similar scale (cf. figure 3.11). Recalling figure 2.2, it can be expected that the spectrum in the lower wavenumber range follows the Kolmogorov scaling, $E(k) \propto k^{-5/3}$, of the inverse energy cascade in the inertial range towards larger scales. Indeed, both the in- and outboard side spectrum roughly follow this scaling in the wavenumber range down to $k_\alpha \rho_s = 0.35$. Towards smaller scales (higher wavenumbers), Kraichnan's model predicts a direct enstrophy cascade following $E(k) \propto k^{-3}$. For the inboard side branch, the spectral index ($\alpha = 2.8$) approaches the predicted value. For the outboard side branch, the injection scale is closer to the high wavenumber cutoff and the spectral decay is much steeper, partly due to a suppression by phase scintillation. While this rudimentary comparison works astonishingly well, it should be kept in mind that the strong assumption was made that all fluctuations originate from $r_{\text{eff}}/a = 0.75$. Furthermore, there have been numerous more sophisticated analytical, numerical and experimental studies trying to refine the wavenumber scaling for ITG and TEM turbulence ([148] and references within), drift wave turbulence [13, 149] and many more examples, which find similar but slightly varying results depending on the investigated setup. Finally, even though PCI captures the spectral properties of the line-integrated density fluctuations well [139], several aspects complicate this comparison: the injection scale as well as the spectral indices are likely to vary along the plasma radius due to varying gradients of density, electron and ion temperature. Additionally, the drift scale varies along the radius, since it depends on the local density, electron and ion temperature. In section 3.3.4, this effect has already been shown to be significant in linear gyrokinetic simulations. The measured wavenumber spectrum as presented

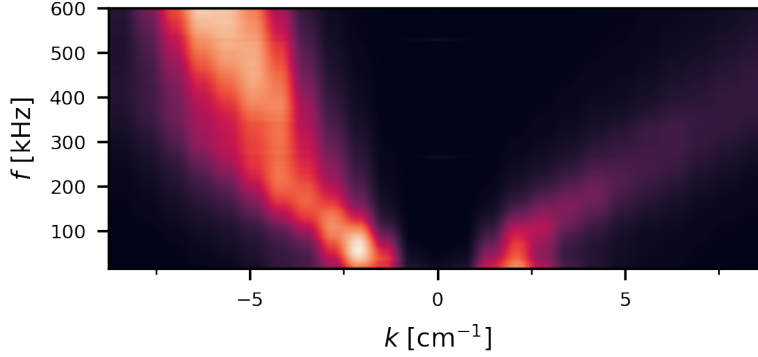


Figure 5.5: Wavenumber-frequency-spectrum during an ECRH plasma in W7-X standard configuration, normalised by the average along the wavenumber axis for each frequency bin.

in figure 5.4 is therefore a convolution of the radial change of spectral indices, the radial structure of fluctuation amplitudes and the shift of scales due to the radially varying drift scale. This makes a quantitative comparison to theoretical expectations difficult.

Returning to the (k, f) -spectrum in figure 5.1, there is one more important aspect which needs to be discussed. The spectral power is not evenly distributed in (k, f) -space, but seems to be mainly aligned along a single slope for each wavenumber branch. A turbulent density fluctuation spectrum is not expected to exhibit a broad distribution in the spectrum instead of a dominant phase velocity. In order to illustrate this better, the spectrum in figure 5.1 is normalised for each frequency bin by its mean value along the wavenumber axis, which effectively removes the power-law decay in frequency space. Figure 5.5 shows the normalised spectrum, which exhibits very clear bands of high spectral power. These bands are observed consistently in every discharge and correspond to a single phase velocity of the fluctuations in the measurement direction, $v_{\text{ph}}^{\text{PCI}} = 2\pi f/k$, which can be associated with the $\mathbf{E} \times \mathbf{B}$ rotation velocity at a specific radius, which is addressed in chapter 6.

5.2 Turbulent density fluctuation amplitudes

The density fluctuation amplitude is one of the factors determining the turbulent heat and particle transport in plasmas (cf. equation (2.19)). It should be kept in mind that the cross phase of density, temperature and electric potential fluctuations sets the transport in addition to their amplitude. Nevertheless, since measurements of the latter are not available at this point, the density fluctuation amplitude is taken as a proxy for transport in this work within the limitation of investigating similar experimental situations. Recalling the conclusions of section 3.3, density fluctuations on the observable scales are expected to be mainly driven by toroidal ITG modes. The curvature drive results in a cross phase of $\pi/2$ between density and potential leading to strong transport. With these considerations, the density fluctuation amplitude is a good proxy for transport in W7-X.

So far, the line-integrated density fluctuation amplitude has been used to monitor the dynamic development of turbulence during a discharge. It has been shown that changes of external parameters like heating power or central fuelling by hydrogen ice pellet injection [150] cause a response of the density fluctuation amplitude and spectrum [114], which can be related to changes in turbulent impurity transport [151] or improved confinement due to a reduction of turbulent transport [18, 20, 79]. Figure 5.6 shows an example spectrogram of a W7-X discharge in standard magnetic field configuration with three steps of ECRH input power. Starting at 2 MW, the power is increased by 1 MW at $t = 2$ s and $t = 4$ s, respectively. The power steps are clearly visible in the spectrum as well as in the fluctuation amplitude.

The absolute amplitude calibration described in section 4.2.5 enables a direct comparison of the fluctuation amplitudes between any discharge. The PCI diagnostic was operational during most experiments in the latest operation phase of W7-X and thus the data covers a large variety of plasma parameters and magnetic configurations. A database of plasma parameters for 200 ms long segments of every discharge of the latest experiment campaign has been compiled¹ and the calibrated PCI density fluctuation amplitude was added to the database. Figure 5.7 shows the density fluctuation amplitudes over the respective ECRH input power. Every marker

¹courtesy of S. A. Bozhenkov

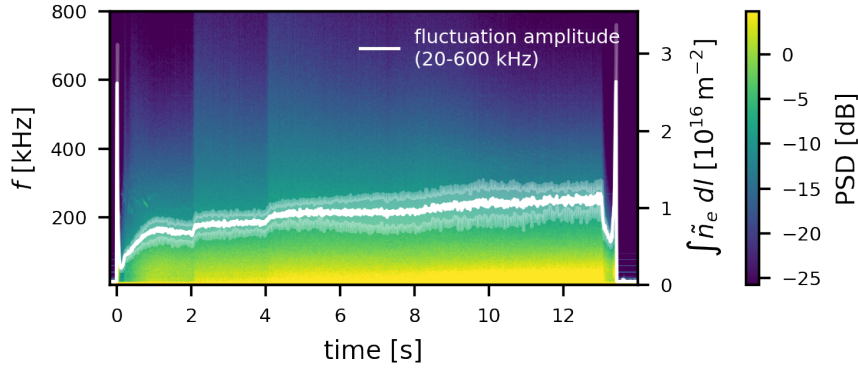


Figure 5.6: Spectrogram of one detector channel signal with absolute fluctuation amplitude of an ECRH plasma in W7-X standard configuration (W7-X XP:20180920.036). The fluctuation amplitude is calculated by integrating the spectrum over the frequency range 20 to 600 kHz and the white transparent band marks the uncertainty of the absolute value.

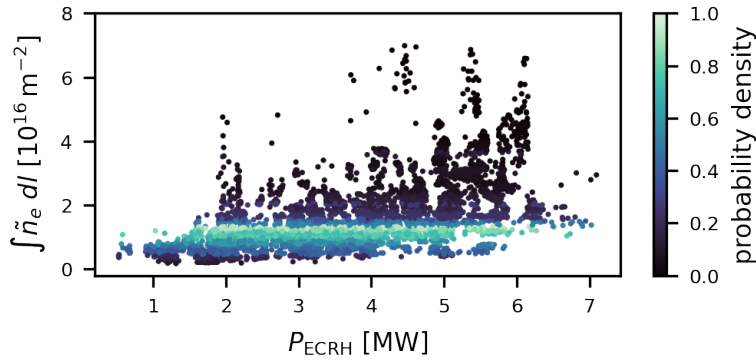


Figure 5.7: Line-integrated density fluctuation amplitude of stationary 200 ms discharge segments with ECRH and gas-fuelling. The colour represents the probability density of the fluctuation amplitude in the presented data set.

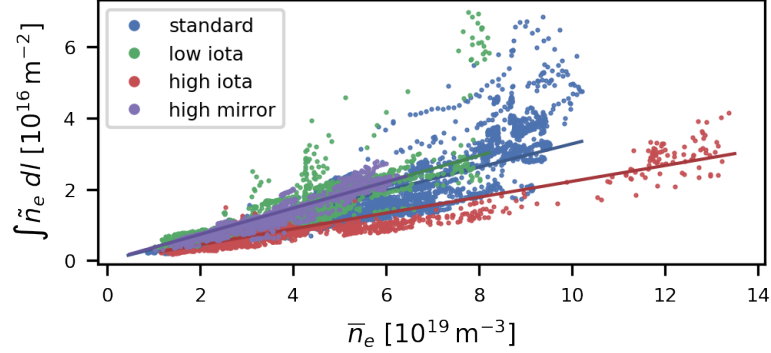


Figure 5.8: Line-integrated density fluctuation amplitude versus line-averaged density for stationary 200 ms discharge segments. Coloured lines represent fits to the data of each magnetic configuration.

represents a 200 ms time window of an ECRH plasma with gas-fuelling (i. e. no pellet injection or NBI), in which the plasma parameters are constant or vary only slowly and no perturbative diagnostics such as impurity or He-gas injections were active. The colour represents the probability density of the density fluctuation amplitude values within the presented data set. It peaks at $\int \tilde{n}_e dl = 1.3 \times 10^{16} \text{ m}^{-2}$ and is skewed towards lower values. There is a weak correlation of density fluctuation amplitude to ECRH power. For higher input power, the fluctuations tend to be stronger. Before drawing any conclusions from this, the dependency on other plasma parameters, which vary strongly within the depicted data set, as well as the magnetic configuration should be considered.

5.2.1 Plasma parameter and configuration dependencies

In this section, the line-integrated density fluctuation amplitude is related to other plasma parameters. It was already noted that the fluctuation amplitude closely follows the line-integrated density during a discharge [114]. With the database including absolutely calibrated fluctuation amplitudes, this relation can be investigated for many discharges. Figure 5.8 shows the line-integrated density fluctuation amplitude versus the line-averaged density measured via interferometry [152]. There is a good correlation between

the two quantities over the whole parameter range. Segments from different magnetic configurations (standard, low and high iota, and high mirror) are depicted with different colours. Within each configuration, the scaling is even clearer. The coloured lines represent linear fits to the data of each configuration. Discharges in the high iota configuration exhibit the lowest density fluctuations amplitudes. The standard configuration, which was run for the majority of experiments, exhibits medium density fluctuation amplitudes with a broader distribution, possibly due to a larger variety in operation parameters. The density fluctuation amplitudes of high iota and high mirror configuration discharges scale very similarly. The constant ratio of line-integrated density fluctuation amplitude to line-averaged density, $\int \tilde{n}_e dl / \bar{n}_e$, is reminiscent of a fluctuation level, \tilde{n}_e / n_e . It should be noted, however, that the fluctuation level is a local quantity and not constant within the plasma. The ion temperature profile stays fairly constant in this type of discharge regardless of other plasma parameters [153]. If ITG modes are the dominant driving mechanism on the ion-scale, the small variation of the ion temperature and other plasma parameters in the considered experiments could explain the observed dependency. In this case, the magnetic configuration has a larger impact on the fluctuation level than other plasma parameters because it influences the ITG growth rate through magnetic curvature and shear. Furthermore, a constant fluctuation level might indicate a radial localisation of the fluctuations in the outer half of the plasma (as previously discussed), where the ion temperature gradient shows very little variation across experiments. In this case, changes of density and temperature in the core do not affect the turbulence since the gradients in the outer half are unchanged. This explanation is somewhat rudimentary, but a more sophisticated approach requires a profile analysis as well as a large number of gyrokinetic simulations, which is beyond the scope of this work.

The proportionality to the line-averaged density can also be explained by the impact on the energy exchange rate from electrons to ions in the plasma, which is given by [4, 36]

$$P_{ei} = \frac{Z^2 e^4 \ln \Lambda \sqrt{m_e}}{(2\pi)^{3/2} \epsilon_0^2 m_i} n^2 \frac{T_e - T_i}{T_e^{3/2}}, \quad (5.2)$$

where Z is the ion charge number, m_e and m_i are the electron and ion mass, respectively, and T_e and T_i are the electron and ion temperature. In the

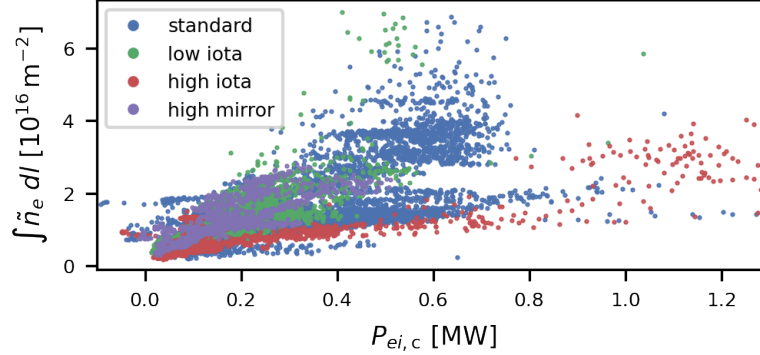


Figure 5.9: Line-integrated density fluctuation amplitude versus central energy exchange rate between electrons and ions for stationary 200 ms discharge segments.

discharges of the data set, only the electrons are heated directly via ECRH and the ions are heated via collisional energy exchange. In order to raise the ion temperature and increase its gradient, the power flux from the electrons needs to be increased. Since $P_{ei} \propto n^2$, increasing the density at similar temperatures will strongly increase the power transfer between the two species. Figure 5.9 shows the line-integrated density fluctuation amplitude versus the electron-ion power transfer in the plasma centre, where the central measurement values of n , T_e and T_i were used. In order to obtain the total power transfer, P_{ei} needs to be integrated along the plasma radius, which requires knowledge of the full profiles of n , T_e and T_i . Radial profiles are not part of the database, therefore the central value is taken as a proxy. Despite this limitation, a correlation is visible in figure 5.9. The more power is available for the ions, the stronger the density fluctuations.

Further correlations of the line-integrated density fluctuation amplitude to other plasma parameters, e. g. the diamagnetic energy, can be found in a similar manner but most of them can be related to the strong correlation to the line-averaged density. It is more interesting to find quantities which might have an impact on the fluctuation level or on $\int \tilde{n}_e dl / \bar{n}_e$. As described in section 3.2, the density gradient as well as the temperature ratio, T_e/T_i , are known to have an impact on the linear ITG mode growth rate. The database contains a density measurement from the centre and the edge of

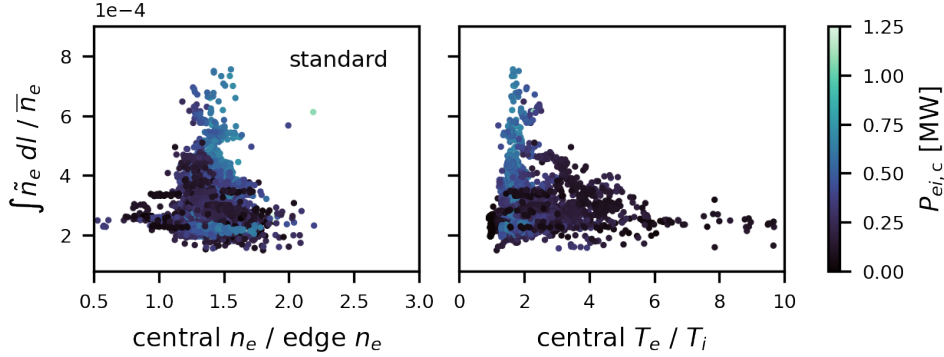


Figure 5.10: Fluctuation levels in W7-X standard configuration versus density peaking (left) and central temperature ratio (right). The colour represents the electron-ion transfer power.

the plasma. Their ratio is a measure of how peaked the density profile is and is used as a proxy for the density gradient in the core. Since the density gradient has a stabilising effect on ITG modes, a negative correlation to the fluctuation level is expected. For the temperature ratio, measurements from the plasma centre are used as well. This is not the region in which ITG modes are believed to be unstable, because the profiles are flat there. However, since the profiles are self-similar for the investigated type of discharge, it can be assumed that a larger temperature ratio in the core coincides with a larger temperature ratio throughout the plasma and vice versa. The T_e/T_i ratio has a destabilising effect on the ITG mode and a positive correlation to the fluctuation amplitude is expected. The fluctuation level versus the discussed quantities is shown in figure 5.10 for the standard configuration and in figure 5.11 for the high iota configuration. The colour of the markers represents the respective electron-ion transfer power. The density peaking has only moderate variation in the available experiments and no trend is visible in either configuration. The central temperature ratio has a larger variation, but the expected effect on the fluctuation level is not observed. On the contrary, only low fluctuation levels are observed at high values of T_e/T_i . The central ion temperature does not vary much in these discharges, which means the variation in temperature ratio is mainly due to a variation of the electron temperature. A connection to the drive of the fluctuations

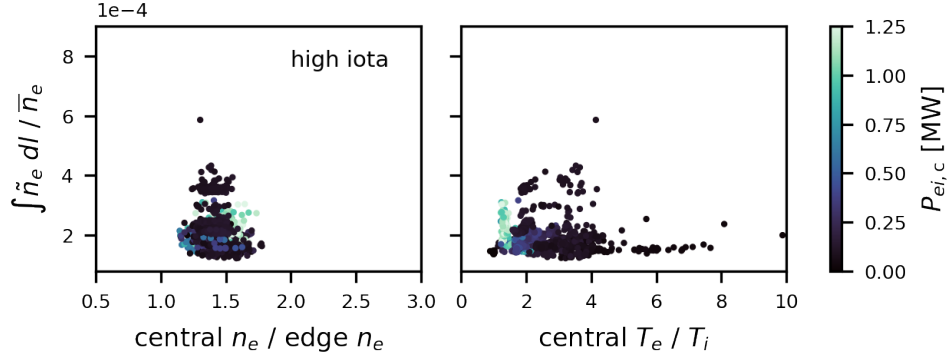
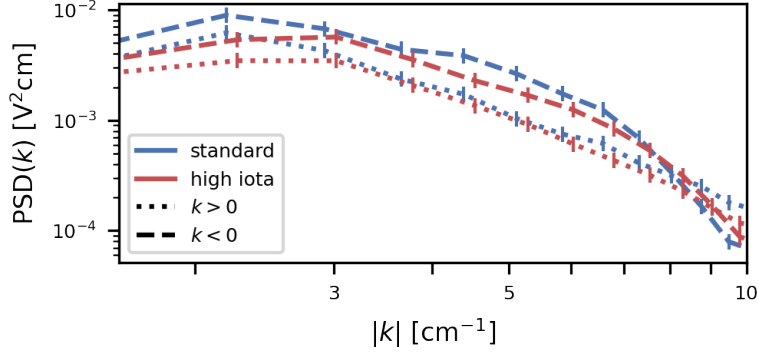


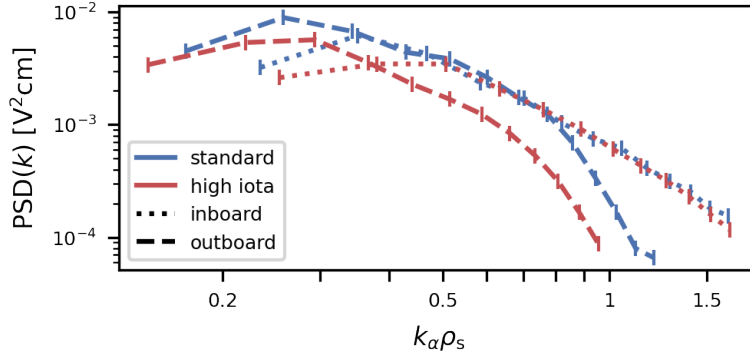
Figure 5.11: Fluctuation levels in W7-X high iota configuration versus density peaking (left) and central temperature ratio (right). The colour represents the electron-ion transfer power.

via the ion temperature gradient can therefore be neglected. A possible explanation is given by a localisation of fluctuations to a radial region which is mainly unaffected by the central temperature ratio, i. e. such that the central temperature ratio is not a good proxy for the temperature ratio at the location where the fluctuations are driven.

In summary, $\int \tilde{n}_e dl / \bar{n}_e$ appears to be constant for discharges of the same magnetic configuration. The reason for this is the self-similarity of the ion temperature and density profiles as well as a low variation of plasma parameters in the given set of experiments. The high iota configuration exhibits a lower fluctuation level than other configurations. Which property of this configuration causes this effect needs further discussion: the difference between the configurations can further be characterised via the wavenumber spectrum. Figure 5.12 shows a direct comparison of wavenumber spectra for discharge segments with similar heating power and density in standard and high iota configuration. Figure 5.12a shows the unprocessed wavenumbers, while figure 5.12b shows the spectrum after geometric correction and normalisation under the assumption of a radial origin at $r_{\text{eff}}/a = 0.75$. In both representations, the inboard ($k > 0$) branches of the two cases agree well over most of the wavenumber range. In figure 5.12a, the main difference between the spectra lies in the wavenumber range $|k| < 3 \text{ cm}^{-1}$, where the spectrum of the high iota case exhibits a lower PSD. These large scale fluc-



(a) Wavenumber spectrum in PCI measurement direction.



(b) Wavenumber spectrum over the normalised binormal wavenumber assuming a radial position of $r_{\text{eff}}/a = 0.75$.

Figure 5.12: Comparison of wavenumber-spectra from comparable discharges in W7-X standard (W7-X XP:20180920.36, $t = 3$ to 4 s) and high iota configuration (W7-X XP:20180904.4, $t = 3$ to 4 s). Frequency integration range: 15 to 600 kHz.

turbulence are more relevant for transport than small scale structures with higher wavenumbers. In figure 5.12b, the outboard side branch exhibits a lower PSD over the entire wavenumber range. It is not clear, whether this indicates a difference of the linear drive of turbulent modes or a different saturation behaviour. A different ZF amplitude could affect the largest scale fluctuations and also result in different density fluctuation levels. Linear and

nonlinear gyrokinetic simulations of the two cases should be able to identify the origin of the measured difference. Further exploration of this difference is left for future work.

6

Radial structure of density fluctuations

Knowledge of the radial distribution of density fluctuations is valuable for several reasons: it provides insight into the origin and driving mechanisms of turbulence, which are usually connected to radial gradients of the kinetic plasma profiles. Furthermore, it helps to identify the regions of strong turbulent transport in combination with a radial transport analysis and to understand differences in discharge scenarios with e. g. reduced turbulence.

The PCI diagnostic at W7-X measures density fluctuations along the entire length of its LOS, which includes the SOL, the edge and the core of the plasma. Distinguishing fluctuations from different radial regions is not possible without further instrumentation or analysis efforts. An extension to the diagnostic consisting of selective mask filters for radially localised measurements is implemented but was not operated successfully during previous experiments. The masks effectively reduce the integration path to a segment where the magnetic field has a certain pitch angle, which varies along the LOS. Even without this feature, it is possible to identify the radial origin of the strongest fluctuations which are measured. This is done by measuring the dominant phase velocity in the PCI (k, f) -spectrum and finding the radius at which it fits the local $\mathbf{E} \times \mathbf{B}$ rotation velocity. The details of this comparison are described in the remainder of this section and have previously been published [133]. Figures and large fractions of the text are reproduced with minor editing for the purpose of this section.

6.1 Reference discharge scenario

Before going on to the details of determining the radial origin of fluctuations with PCI, a paradigm reference discharge is selected as a representative example case. The experimental results as well as the gyrokinetic and neoclassical simulations will be based on the experimental data of this discharge. The discharge is an ECRH heated hydrogen plasma with fuelling by gas without addition sources such as cryogenic pellet injection or NBI. Since most discharges in W7-X have been of this type, it has the best data coverage [18]. Furthermore, this scenario represents the future long-pulse experiments at W7-X.

Figure 6.1 shows an overview of the main discharge parameters. The magnetic field is in W7-X standard configuration with 5/5-island structure in the SOL and an average magnetic field strength on the magnetic axis of $\langle B_0 \rangle = 2.41$ T. The external heating is purely ECRH with short ($t = 100$ ms) neutral beam injections for diagnostic purposes. The heating power is stepped down during the discharge, while the line-averaged density is kept constant. Accordingly, the central electron temperature and diamagnetic energy decrease during the discharge. The ion temperature is constant, which is the case for almost every gas-fuelled ECRH discharge in W7-X [153]. During the phases of constant heating power, which are respectively much longer than the energy or particle confinement times, the plasma parameters are stationary. The time window 4.5 to 6.5 s, with medium heating power, $P_{\text{ECRH}} = 3.2$ MW, (middle shaded region in figure 6.1) was selected as an experimental reference for the following analyses and simulations. Figure 6.2 shows the density and temperature profiles of the reference plasma (time average over 4.5 to 6.5 s), which are paradigmatic for ECRH plasmas in W7-X and resemble the model profiles discussed in figure 3.8. The density and ion temperature profiles are flat throughout the core and decrease only outside $r_{\text{eff}}/a = 0.7$. The electron temperature is centrally peaked and much higher than the ion temperature in the core because of the central electron heating and weak collisional coupling to ions due to the relatively low plasma density, $n_{\text{peak}} = 3.5 \times 10^{19} \text{ m}^{-3}$, and high electron temperature, $T_{e,\text{peak}} = 5.1$ keV. The right hand side of figure 6.2 shows the respective normalised gradients, a/L_X (cf. equation (3.17)). The ion temperature gradient becomes large in the outer part of the plasma, $r_{\text{eff}}/a > 0.6$, while the density gradient stays comparably small, a combination that is expected to destabilise ITG

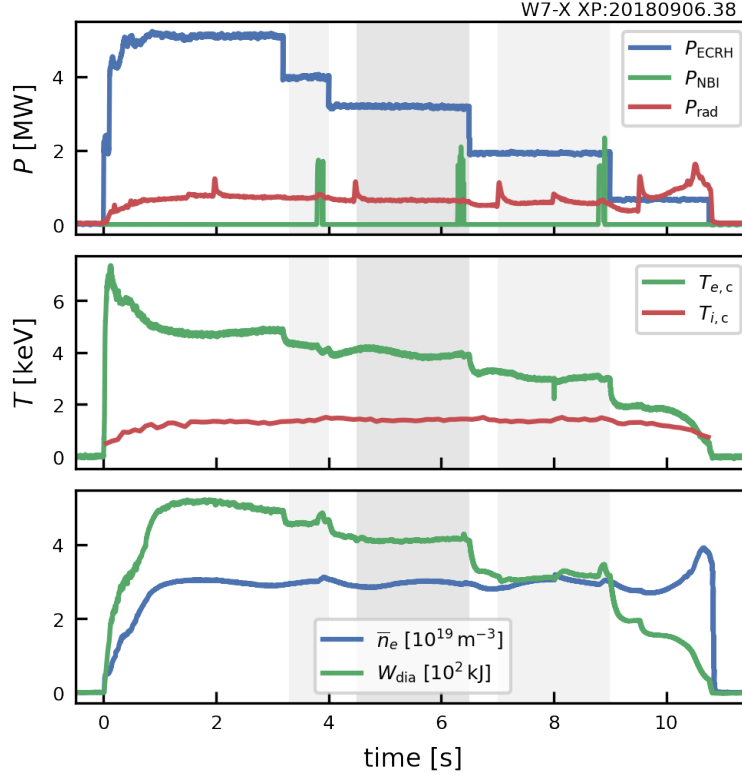


Figure 6.1: Overview of a typical ECRH discharge in W7-X with hydrogen as the main ion species. The input power was stepped down while keeping the density constant. Transient neutral beam injections were launched for diagnostic purposes. The depicted electron and ion temperatures correspond to measurements of the central channel of the electron cyclotron emission (ECE) [154] and the X-ray imaging crystal spectroscopy (XICS) [155] diagnostic, respectively. Modified from BÄHNER *et al.* [133].

turbulence.

6.2 Dominant fluctuation propagation velocity

The basis for the identification of the radial location of fluctuations is the dominant phase velocity in the PCI (k, f)-spectra, $v_{\text{ph}}^{\text{PCI}} = 2\pi f/k$, which was

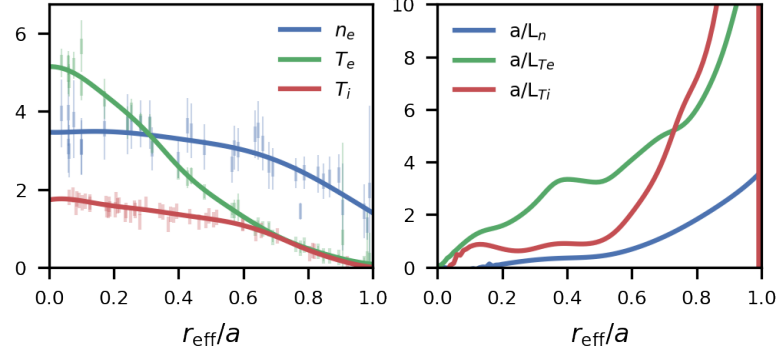


Figure 6.2: Radial profiles of the reference discharge averaged over 4.5 to 6.5 s. The left panel shows the electron density, n_e in 10^{19} m^{-3} and electron temperature, T_e in keV, both measured by the Thomson scattering (TS) diagnostic [156], as well as the ion temperature, T_i in keV, measured by charge exchange recombination spectroscopy (CXRS) [92]. The vertical lines are measurement values with error bars which represent measurement uncertainties. The solid lines are best fits to the measurement data. The right panel shows the normalised inverse gradient lengths corresponding to the best fits. Reproduced from BÄHNER *et al.* [133].

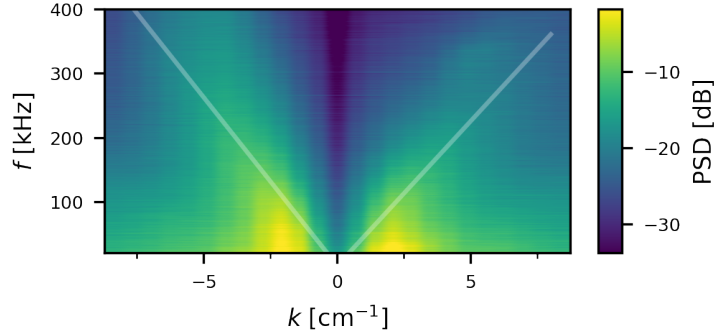


Figure 6.3: Wavenumber-frequency spectrum during an ECRH plasma in W7-X standard magnetic configuration. Modified from BÄHNER *et al.* [133].

briefly introduced in section 5.1. Most of the power in the spectrum is aligned along a single slope for both the positive and negative wavenumber branch, forming dominant velocity bands in both directions (see figure 6.3). The phase velocity of the typical instabilities in the plasma frame is comparably small ($v_{\text{ph}} \approx 500 \text{ m s}^{-1}$ for ITG modes, see figure 3.5 and the corresponding description). The $\mathbf{E} \times \mathbf{B}$ rotation of the plasma due to the neoclassical radial electric field, on the other hand, is generally much faster and adds a Doppler shift to the fluctuations' frequencies [93, 109, 157]. The propagation velocity of turbulent fluctuations in the laboratory frame, u_α , is therefore a combination of the mode's intrinsic phase velocity, v_{ph} , and the $\mathbf{E} \times \mathbf{B}$ rotation velocity, $v_{\mathbf{E} \times \mathbf{B}}$, which both point in the binormal direction,

$$u_\alpha = v_{\text{ph}} + v_{\mathbf{E} \times \mathbf{B}} \approx v_{\mathbf{E} \times \mathbf{B}}. \quad (6.1)$$

Since the radial profile of $v_{\mathbf{E} \times \mathbf{B}}$ is generally not flat, u_α depends on the radial location of the fluctuations. The line-integrated measurement of the PCI diagnostic covers fluctuations from all radial regions, which should result in a broad distribution of phase velocities in the (k, f) -spectrum, contrary to what is observed.

The apparent dominant phase velocity indicates that there is a radial region with little variation of the local $v_{\mathbf{E} \times \mathbf{B}}$ and with strong fluctuations, which cause the spectral power to be concentrated at the corresponding slope in the spectrum. In this interpretation, the two wavenumber branches correspond to the inboard and outboard side, since the $\mathbf{E} \times \mathbf{B}$ rotation changes direction in the frame of the PCI laser beam, when it passes the magnetic axis. By comparing the propagation velocity which corresponds to the strong fluctuations in the dominant band of the PCI spectrum to the radial $v_{\mathbf{E} \times \mathbf{B}}$ profile, the radial origin of the strong fluctuations can be estimated. For this comparison, an estimate of the propagation velocity of the fluctuations based on the measured phase velocity in the spectrum, $v_{\text{ph}}^{\text{PCI}}$, as well as an estimate of the local $v_{\mathbf{E} \times \mathbf{B}}$ along the LOS is required.

$v_{\text{ph}}^{\text{PCI}}$ is determined as described in section 4.2.4, but geometrical effects along the LOS have to be taken into account to obtain u_α . As discussed at the end of section 4.2.3, PCI measures a projection of the wave onto the measurement direction, $\hat{\mathbf{e}}_{\text{m}}$. Analogous to equation (4.19), there is

$$v_{\text{ph}}^{\text{PCI}} = u_\alpha \hat{\mathbf{e}}_\alpha \cdot \hat{\mathbf{e}}_{\text{m}}, \quad (6.2)$$

$$\Leftrightarrow u_\alpha = v_{\text{ph}}^{\text{PCI}} / \cos \theta, \quad (6.3)$$

where θ is the angle between the measurement direction of PCI and the binormal direction and depends on the position along the LOS. Furthermore, the projection changes even across the width of the laser beam. The difference between the two outermost LOSs can be non-negligible at certain radii. Taking this effect into account is more complicated, since all LOSs contribute to the calculated (k, f) -spectra with varying intensity corresponding to the beam cross section on the detector. For the purpose of the comparison in this work, this variation is understood as an uncertainty of the projection of the central, most illuminated LOS.

6.3 $\mathbf{E} \times \mathbf{B}$ velocity and neoclassical radial electric field

The last ingredient for the estimation of the radial location of fluctuations is the $\mathbf{E} \times \mathbf{B}$ rotation velocity of the plasma. The radial electric field, E_r , which is responsible for the $\mathbf{E} \times \mathbf{B}$ rotation, is predominantly determined by the ambipolar NC transport in stellarators [8], cf. section 2.2.2. Measurements by CXRS and XICS show the existence of an electron root in the core and an ion root in the outer half of ECR heated plasmas in W7-X [92, 155]. They generally show good agreement with numerical neoclassical calculations by codes like the drift kinetic equation solver (DKES) [158, 159]. DBS measurements also show a good agreement between the radial electric field obtained from the poloidal velocity of fluctuations, $E_r^{\text{DBS}} = u_\alpha B$, and neoclassical calculations by DKES [93, 160]. For the calculations with DKES, the experimental kinetic plasma profiles are used as input. At the plasma edge, ion and electron temperatures are assumed to be equal. Due to measurement uncertainties, the ion temperature sometimes slightly exceeds the electron temperature even though there is no ion heating. For a meaningful simulation result in these cases without reversed fluxes, T_e and T_i are manually set equal and smoothing is applied to avoid a discontinuity in the gradient. Figure 6.4 shows the neoclassical electric field calculated for the profiles of the reference plasma, cf. figure 6.2. The dashed line is the electron root solution, which only appears in the core, where $T_e \gg T_i$. The ion root, plotted as a solid line, is relevant in the outer half of the plasma, where it forms an E_r -well at $r_{\text{eff}}/a \approx 0.8$. Since it has been shown

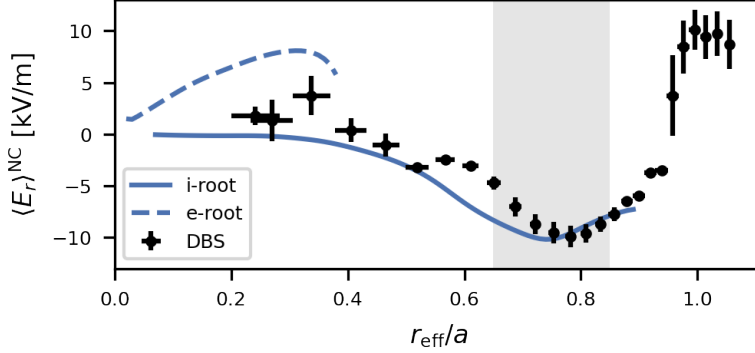


Figure 6.4: Flux surface averaged neoclassical radial electric field from simulations with DKES (blue) and measurements by DBS (black) for the reference discharge. Reproduced from BÄHNER *et al.* [133].

experimentally that an electron root radial electric field exists in the core, the corresponding electron root velocity should be preferred where both solutions exist. Sensitivity studies have previously produced an uncertainty of the simulated $\langle E_r \rangle^{\text{NC}}$ on the order of 10%, by varying the local density and temperature values and gradients by 10% [93, 161]. The black error bars are measurement points from DBS, which generally agree with the ion root solution by DKES in the region of interest (shadowed region around 75% of the minor radius, where the drive of ITG turbulence should be large, cf. section 3.3.4). At the LCFS, the measured E_r changes sign, resulting in a large shear. The corresponding $\mathbf{E} \times \mathbf{B}$ velocity of the E_r -well in the region of interest is $v_{\mathbf{E} \times \mathbf{B}} \approx 4 \text{ km s}^{-1}$, which is the same order of magnitude as the phase velocity measured in the PCI (k, f)-spectra. The good agreement of the DBS measurement and the simulated E_r supports the assumption that the propagation velocity of fluctuations is dominated by the $\mathbf{E} \times \mathbf{B}$ rotation, $u_\alpha \approx v_{\mathbf{E} \times \mathbf{B}}$.

Finally, for the direct comparison to the local propagation velocity of the fluctuations which corresponds to the PCI dominant phase velocity, the flux compression must be taken into account. The radial electric field given by DKES, $\langle E_r \rangle^{\text{NC}}$, is a flux surface averaged quantity, corresponding to $\langle E_r \rangle^{\text{NC}} = -\partial\phi/\partial r_{\text{eff}}$, where ϕ is the electrostatic potential, which is assumed to be a flux surface quantity, i. e. constant on each flux surface to first order.

In order to obtain the local NC electric field, the real space gradient of the effective radius, $|\nabla r_{\text{eff}}|$, needs to be multiplied to the flux surface average, $\langle E_r \rangle^{\text{NC}}$. The magnitude of the corresponding $\mathbf{E} \times \mathbf{B}$ velocity is then

$$v_{\mathbf{E} \times \mathbf{B}} = \frac{\langle E_r \rangle^{\text{NC}} |\nabla r_{\text{eff}}|}{B}, \quad (6.4)$$

where all components vary along the PCI LOS.

6.4 Comparison of velocities

After having discussed the estimation of u_α and $v_{\mathbf{E} \times \mathbf{B}}$, the actual comparison of the velocities for the case of the reference discharge is presented in order to investigate if and where they match. Figure 6.5 shows the direct comparison of the local $\mathbf{E} \times \mathbf{B}$ velocity from neoclassical calculations and the local binormal velocity, which corresponds to the measured dominant phase velocity in the PCI (k, f) -spectrum along the PCI LOS. The $v_{\mathbf{E} \times \mathbf{B}}$ in the ion diamagnetic direction stems from the electron root solution for E_r , the $v_{\mathbf{E} \times \mathbf{B}}$ in the electron diamagnetic direction from the ion root solution. A typical phase velocity of the ITG modes, $v_{\text{ph}} = 500 \text{ m s}^{-1}$ in the ion diamagnetic direction (see figure 3.5), is added to $v_{\mathbf{E} \times \mathbf{B}}$ at $r_{\text{eff}}/a = 0.75$ for reference. The negative phase velocity in the PCI (k, f) -spectrum was used for the outboard side mapping and the positive phase velocity for the inboard side (solid lines). The dotted lines correspond to the inverse attribution for the central LOS. The different geometrical corrections of the 32 PCI LOSs are illustrated by faded lines. Both u_α and $v_{\mathbf{E} \times \mathbf{B}}$ were calculated for each LOS and opacity-weighted by the respective laser amplitude. The difference between the LOSs is very small on the inboard side but relevant on the outboard side. The measured velocities match $v_{\mathbf{E} \times \mathbf{B}}$ best at $r_{\text{eff}}/a \approx 0.75$, which is also the position of the well in $\langle E_r \rangle^{\text{NC}}$. With the inverse attribution, the phase velocity measured by PCI would agree with the NC results only quite close to the core, near the electron-root solution. The attribution of wavenumber branches to the in- and outboard side for which the velocities match in the outer half of the plasma agrees with the expectation of linear instability growth (cf. section 3.3.4) and is therefore preferred. Additionally, the (k, f) -spectrum has qualitatively the same properties in most discharges even though the electron-root solution does not exist in every case.

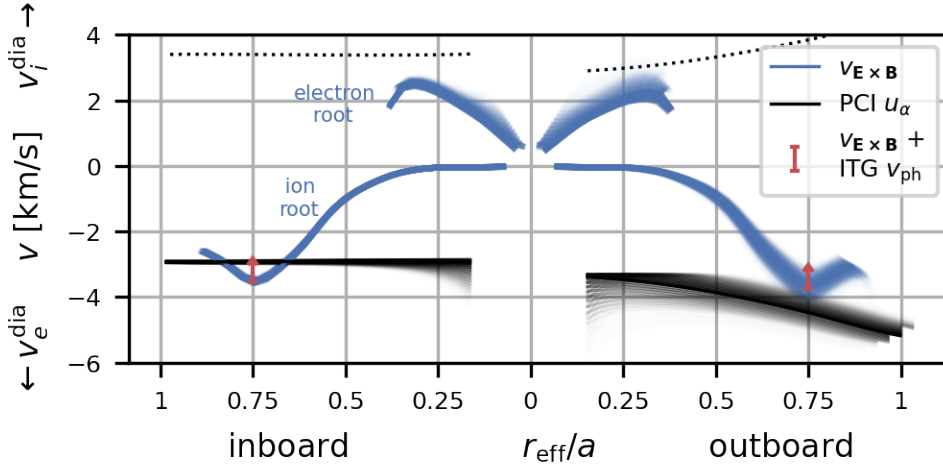


Figure 6.5: Local $\mathbf{E} \times \mathbf{B}$ rotation velocity from NC calculations and the binormal velocity corresponding to the dominant phase velocity in the PCI the spectrum along the PCI LOS. A linear estimate of the phase velocity of ITG modes at $r_{\text{eff}}/a = 0.75$ (cf. figure 3.5) is added to $v_{\mathbf{E} \times \mathbf{B}}$ for reference. The dotted lines show the alternative attribution of wavenumber branch to in-/outboard side for the central LOS. The faded black and blue lines illustrate the geometric variation of the mapping across the 32 LOSs weighted by the respective laser power. Reproduced from BÄHNER *et al.* [133].

The negative wavenumber branch can therefore be assumed to correspond almost exclusively to the outboard side of the plasma and vice versa. The ITG mode phase velocity is just a small correction and on the same order as the geometrical effects of the finite beam width and the uncertainty of $v_{\mathbf{E} \times \mathbf{B}}$ due to the uncertainty of the input profile parameters ($\approx 10\%$, not shown here). The observed match suggests that strong fluctuations exist at $r_{\text{eff}}/a \approx 0.75$ which cause a dominant linear phase velocity in the PCI (k, f) -spectrum determined by $v_{\mathbf{E} \times \mathbf{B}}$ at that position.

A simple test for the hypothesis that $v_{\text{ph}}^{\text{PCI}}$ in each wavenumber branch is determined by $v_{\mathbf{E} \times \mathbf{B}}$, is an experiment with reversed magnetic field direction but otherwise similar plasma parameters. The $\mathbf{E} \times \mathbf{B}$ rotation and diamagnetic direction change sign while everything else stays the same, if the discharges are similar enough. Two almost identical experiments in low

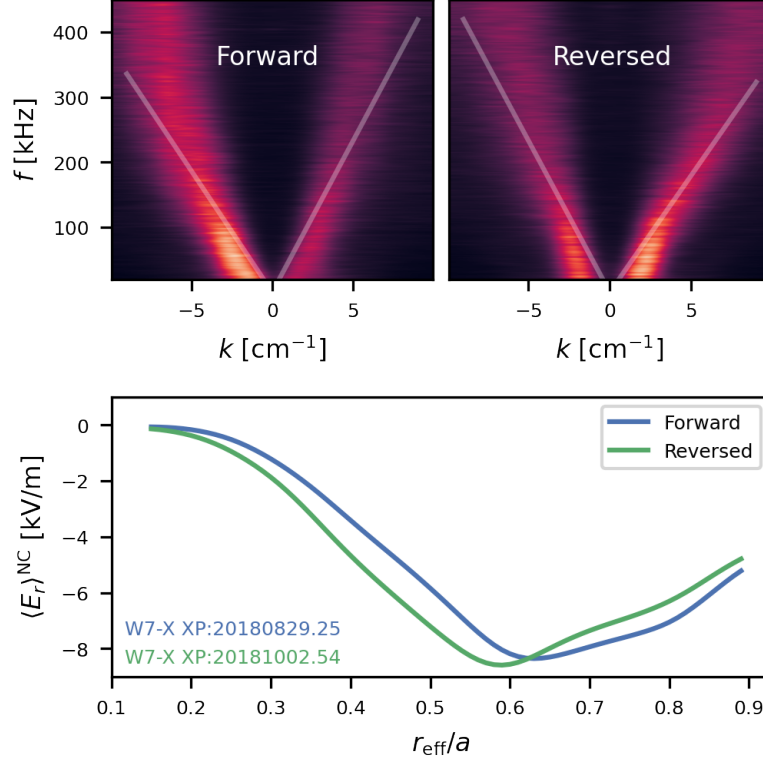


Figure 6.6: Top: Wavenumber-frequency-spectra and dominant phase velocities of discharges with forward and reversed field direction. The spectra are normalised to the mean along the k -axis for a better visualisation of the dominant phase velocity. Bottom: DKES E_r for the respective discharges. Modified from BÄHNER *et al.* [133].

iota configuration are compared. In both discharges, 5 MW of ECRH were applied at a line-integrated density of $4 \times 10^{19} \text{ m}^{-2}$. Figure 6.6 shows the (k, f) -spectra and the simulated neoclassical radial electric field of the respective discharges. The radial electric field profiles are very similar. Since $v_{\mathbf{E} \times \mathbf{B}}$ changes direction, the spectrum is mirrored at the $k = 0$ axis when going from forward to reversed field, but looks otherwise identical. The measured dominant phase velocities for the negative (positive) wavenumber branch are $v_{\text{ph}}^{\text{PCI}} = -2.3 \text{ km s}^{-1}$ (2.9 km s^{-1}) for the forward field case and

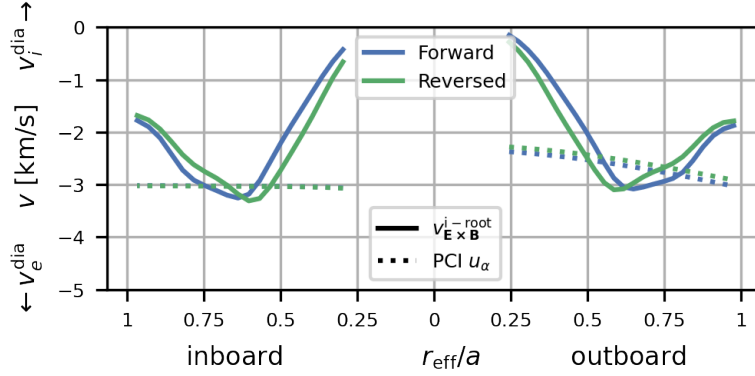


Figure 6.7: Velocity comparison for forward and reversed magnetic field experiments. Modified from BÄHNER *et al.* [133].

$v_{\text{ph}}^{\text{PCI}} = -2.9 \text{ km s}^{-1}$ (2.3 km s^{-1}) for the reversed field case. The asymmetry in the spectral power also switches sides. Figure 6.7 shows the velocity comparison for the two discharges. It yields a similarly good match as in the reference plasma for both cases only if the attribution of each k -branch to the in- or outboard side is reversed. There is no electron root solution in this case, which excludes an inverse attribution. The match is best at the location of the E_r -well, which is not at $r_{\text{eff}}/a = 0.75$ but further inwards. This poses the question, whether the location of strongest fluctuations is different to the reference case and which role the E_r -well itself plays for the dominant phase velocity in PCI spectra.

The analysis was repeated for discharges with varying input power or density. Both variations have an effect on the radial location and the depth of the well in the ion root E_r . For the scan in ECRH power, three time windows within the discharge presented in figure 6.1 (shaded regions) were analysed, where the ECRH power was stepped down from 4 MW over 3.5 MW to 2 MW, while keeping the line-integrated density constant at $4 \times 10^{19} \text{ m}^{-2}$. The comparison of u_α and $v_{\mathbf{E} \times \mathbf{B}}$ for these cases is shown in 6.8. The ion temperature stays constant throughout the discharge and the electron temperature decreases as a response to the decreasing heating power. The difference between T_e and T_i decreases and the radial location at which the two species are in thermal equilibrium moves inwards. As a consequence, both the ion and electron root E_r has a smaller magnitude for lower heating

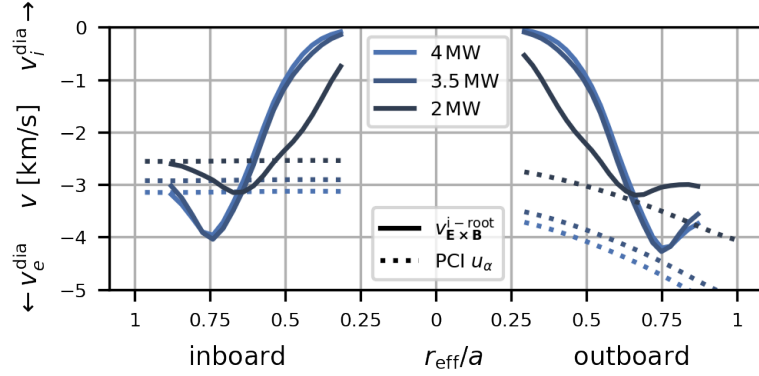


Figure 6.8: Velocity comparison for a scan of ECRH input power. Electron root solutions for $v_{\mathbf{E} \times \mathbf{B}}$ are not shown. Modified from BÄHNER *et al.* [133].

power and the transition point as well as the radial location of the E_r well move radially inwards. The measured dominant phase velocity follows this trend but the difference between the 4 MW and 3.5 MW cases is very small compared to the overall uncertainties. For the scan of plasma density, three discharges with heating power $P_{\text{ECRH}} = 4.7 \text{ MW}$ were chosen. The line-integrated density was increased between the discharges from $4 \times 10^{19} \text{ m}^{-2}$ over $6 \times 10^{19} \text{ m}^{-2}$ to $8 \times 10^{19} \text{ m}^{-2}$. The comparison of u_α and $v_{\mathbf{E} \times \mathbf{B}}$ for these cases is shown in 6.9. Increasing the density at constant heating power has a similar effect as decreasing the heating power at constant density, since in both cases less power per particle is available. Accordingly, the magnitude of the E_r decreases for higher densities and the measured u_α follows the trend closely. In all situations, the match is usually best around the position of the E_r -well, which also varies but only within the outer half of the plasma. In many cases, the electron root solution is very small or not existing at all, which makes a significant contribution of core density fluctuations to the dominant phase velocity unlikely. In conclusion, strong density fluctuations must be present in the outer half of the plasma and the well in the $v_{\mathbf{E} \times \mathbf{B}}$ -profile, which appears in the same radial region, determines the observed dominant phase velocity in PCI (k, f)-spectra.

While there is striking evidence that the origin of the observed fluctuations is located at the position of the E_r -well, the velocity variations within

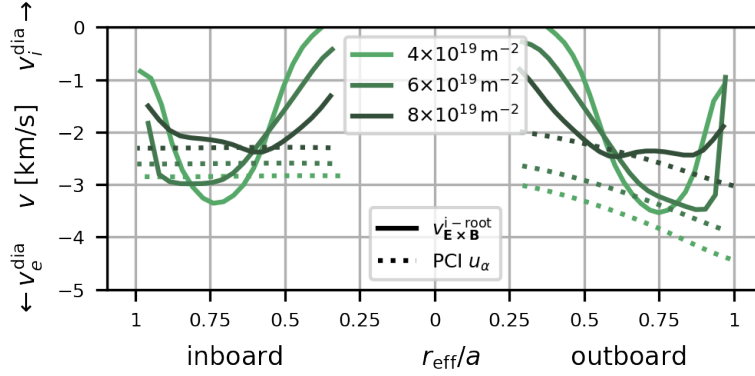


Figure 6.9: Velocity comparison for a scan of line-integrated density. Electron root solutions for $v_{\mathbf{E} \times \mathbf{B}}$ are not shown. Modified from BÄHNER *et al.* [133].

the $v_{\mathbf{E} \times \mathbf{B}}$ -profile are expected to have an impact on the observed (k, f) -spectrum as well. The spectral power originating from fluctuations at a radial location with a strong radial velocity gradient will be spread out in (k, f) -space. If the fluctuations arise at a radial location with small velocity gradient, the spectral power is focused at a single angle in the (k, f) -spectrum. Fluctuations will produce clearer dominant phase velocities, if they appear in a region in which the velocity profile is flat. While this does not disagree with the interpretation of the strongest density fluctuations causing the dominant phase velocity, both mechanisms have to be taken into account to understand the PCI spectra. In the following section, the effect of the velocity gradient on PCI spectra is examined with the SPCI diagnostic.

6.5 Simplified rotation model with SPCI

As described in section 4.1.2, the synthetic PCI diagnostic numerically reproduces the PCI signal based on global gyrokinetic simulations. Additionally, a simplified model which captures the basic features of the $\mathbf{E} \times \mathbf{B}$ rotation of turbulent density fluctuations was implemented. Here, a static snapshot of density fluctuations is derived from a GENE-3D simulation for W7-X [61] is propagated poloidally following a predefined radial rotation velocity pro-

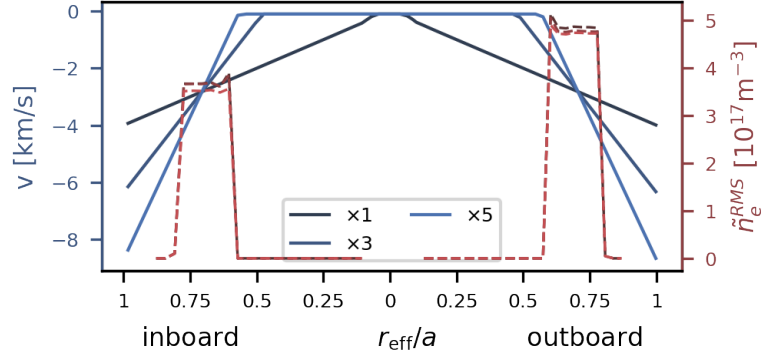


Figure 6.10: Model functions for the $v_{\mathbf{E} \times \mathbf{B}}$ -profile (blue) and corresponding density fluctuation amplitude profile (red) used as input for the rotation model of SPCI. Reproduced from BÄHNER *et al.* [133].

file. The model is described in more detail in [133, 139]. In this section, the effect of a rotating plasma background on the measurement of density fluctuations by PCI is investigated for various rotation velocity profiles. In particular, the radial gradient of the rotation velocity affects the dominant phase velocity in the measured (k, f) -spectrum.

In order to test the effect of a velocity gradient, fluctuations were restricted to a narrow radial interval by a top-hat function of width $0.2a$ centred around $r_{\text{eff}}/a = 0.7$. The individual shape of the velocity profiles is chosen such that they have the same magnitude in the centre of the regions of large fluctuation amplitudes but differ in the radial variation, as shown in figure 6.10. In principle, one would expect the resulting (k, f) -spectra to show the same dominant phase velocity for each case with a varying spread of spectral power. Figure 6.11 shows the (k, f) -spectra for three different gradients of the model velocity profile. The radial velocity gradient increases from left to right. In the left case, the gradient corresponds roughly to a rigid plasma rotation and shows a very distinct dominant phase velocity with little spectral power in other parts of the spectrum. Model profiles with even flatter gradient produced very similar results and are not shown here. For increasing gradients, the spectral power is clearly spread out over a larger area in (k, f) -space. The gradient in the right case corresponds roughly to the maximum gradient that is observed experimentally at the

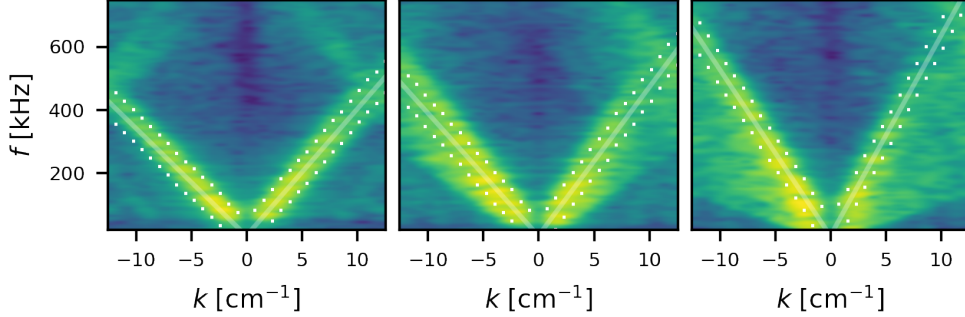


Figure 6.11: Wavenumber-frequency spectra of SPCI data corresponding to model velocity profiles with increasing radial gradient from left to right. The colour scale is in dB. The white lines mark the dominant linear phase velocities, the white dashes mark a ± 50 kHz interval around the dominant v_{ph} . Reproduced from BÄHNER *et al.* [133].

edge of the considered plasma discharges. In order to measure this effect quantitatively, the integrated spectral power in a ± 50 kHz band around the dominant phase velocity, s_v , is compared to the total power in the spectrum, s_{total} . The velocity band is marked by white dashes in figure 6.11. In the left case, 68% of the power is concentrated along the negative v_{ph} and 31% along the positive v_{ph} . Only 1% of spectral power appears outside the velocity bands. For the most severe gradient, the right case, these fractions go down to 50% and 8% for the negative and positive velocity band, respectively. Additionally, the dominant phase velocity increases for the cases with higher gradient, even though the average velocity over the top-hat function stays the same. This is because the maximum velocity on the domain of the \tilde{n}_e step function increases. Due to the nonlinear relation between phase velocity and the slope in the (k, f) -spectrum, more power is concentrated at a larger slope. In other words, the dominant phase velocity is prone to show the higher end of phase velocities in the fluctuations. These results have important consequences: if the velocity profile has a well, as it does in the experiment, two effects are responsible for a concentration of spectral power at the slope of the velocity in the well. The first effect is the low velocity gradient at that position and the second is the observed tendency that fluctuations with higher velocities are emphasised in the (k, f) -spectrum.

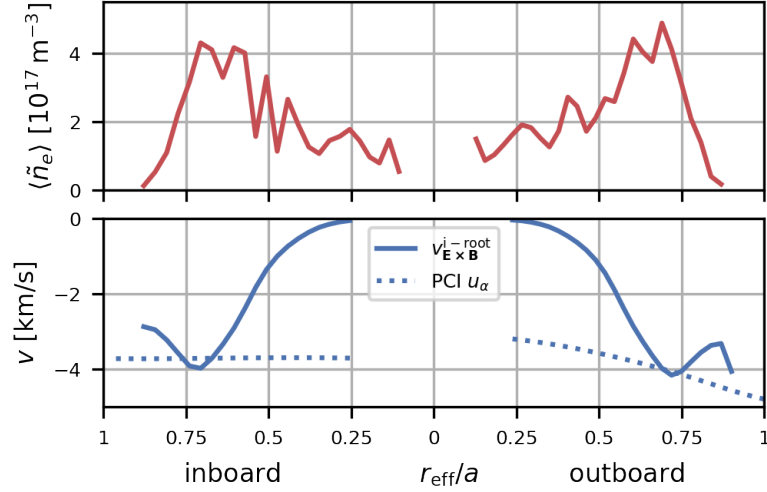


Figure 6.12: Radial profile of density fluctuation amplitude from a global GENE-3D simulation [61] (upper panel) and simulated NC $v_{\mathbf{E} \times \mathbf{B}}$ -profile from DKES (lower panel, cf. figure 6.4). Additionally, the phase velocities determined from the resulting SPCI (k, f) -spectrum are shown for comparison.

It is important to point out that the investigated effect is different from turbulence suppression by $\mathbf{E} \times \mathbf{B}$ shear [89]. Neither the linear stabilisation of turbulent modes nor the nonlinear decorrelation through $\mathbf{E} \times \mathbf{B}$ shear can be simulated with this simplified model. However, a shift of spectral power to higher wavenumbers is possible in the present model through shearing of structures spanning several flux surfaces.

Finally, for a direct comparison to the experimental (k, f) -spectrum, the simulated neoclassical $v_{\mathbf{E} \times \mathbf{B}}$ -profile, taken from figure 6.4, and a simulated fluctuation amplitude profile with radial variation taken from BAÑÓN NAVARRO *et al.* [61], are used as input for the model. Figure 6.12 shows the density fluctuation amplitude and $v_{\mathbf{E} \times \mathbf{B}}$ profiles. The fluctuation amplitude profile is highest at $r_{\text{eff}}/a \approx 0.7$ but otherwise rather flat. Figure 6.13 shows the resulting (k, f) -spectrum, which has very similar features as the experimental spectrum (see figure 6.3). The dominant phase velocities in the spectrum are marked by white lines and added to figure 6.12. They match $v_{\mathbf{E} \times \mathbf{B}}$ at the position of the well on both the in- and outboard side, which

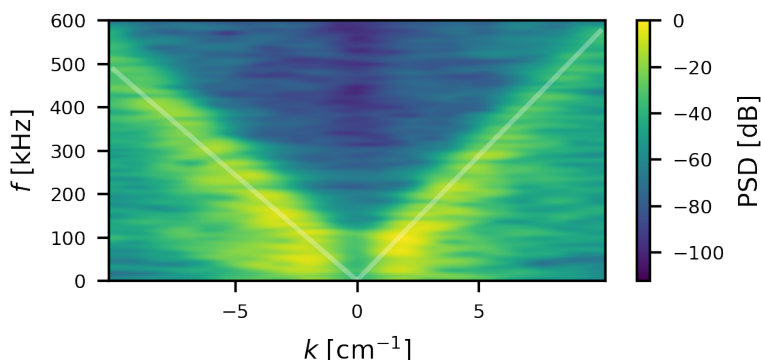


Figure 6.13: Wavenumber-frequency spectrum of SPCI data with the simplified the $\mathbf{E} \times \mathbf{B}$ rotation model based on velocity and density fluctuation amplitude profiles in figure 6.12. Reproduced from BÄHNER *et al.* [133].

confirms that the analysis is consistent. The model reproduces the qualitative behaviour of the investigated situation well: the density fluctuation amplitude is particularly strong at the position of the E_r -well and produces dominant phase velocities in the (k, f) -spectrum, which match the $\mathbf{E} \times \mathbf{B}$ velocity of the well. A more detailed or even quantitative comparison of experimental and simulated spectra is not reasonable, since the simulation by BAÑÓN NAVARRO *et al.* [61] does not closely match the experimental situation of the reference discharge. Nonlinear global simulations including the background radial electric field with GENE-3D and other global gyrokinetic codes like EUTERPE [162, 163] and the gyrokinetic toroidal code (GTC) [100, 164] are planned, which can then be directly compared to measurement data via the synthetic diagnostic.

6.6 Gyrokinetic simulations

In order to study the radial and poloidal distribution of density fluctuations in more detail, numerical nonlinear gyrokinetic flux tube simulations with GENE were conducted. Three flux tubes at different radial positions outside the half-radius were selected. The flux tubes intersect the PCI LOS on the outboard side and thus simulate the turbulence measured by PCI as closely as possible (cf. figure 4.6 and corresponding discussion in section 4.1.2). The

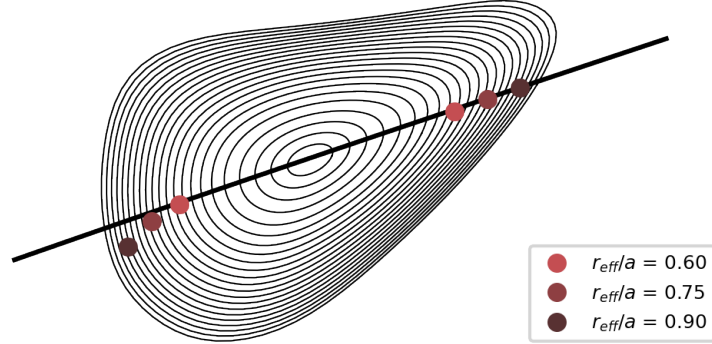


Figure 6.14: Intersections of the GENE flux tubes with the cross-section of the PCI LOS (thick black line).

r_{eff}/a	a/L_n	a/L_{T_i}	a/L_{T_e}	T_e/T_i
0.60	0.7	2.1	4.1	1.2
0.75	1.5	5.4	5.4	1.0
0.90	2.6	8.9	8.9	1.0

Table 6.1: Input parameters for GENE flux tube simulations. The values are taken from experimental profiles in figure 6.2. Outside $r_{\text{eff}}/a = 0.7$ the ion temperature and electron temperature are assumed to be equal. The simulations were run with a resolution of $(n_x, n_y, n_z, n_{v_{\parallel}}, n_{\mu}) = (128, 64, 128, 32, 9)$ in a box of $(L_x, L_y, L_z) = (125, 125, 2\pi)$ in normalised GENE units.

fluctuations on the inboard side are also captured by the same flux tubes, since they pass through the stellarator symmetric PCI cross-section in each of the five identical modules of W7-X and very close to the inboard LOS position in one of them. Figure 6.14 shows the flux tubes at the toroidal angle of the PCI diagnostic. The intersection with the LOS can be observed on the outboard (right hand) and inboard (left hand) side. The density and temperature gradients, as well as the temperature ratio for each radial position are listed in table 6.1 and represent the profiles shown in figure 6.2. Similarly as for the DKES simulation, electron and ion temperatures are set to be equal, $\tau = 1$, in the edge of the plasma, $r_{\text{eff}}/a > 0.7$. Both species were treated kinetically in the simulations and without collisions or

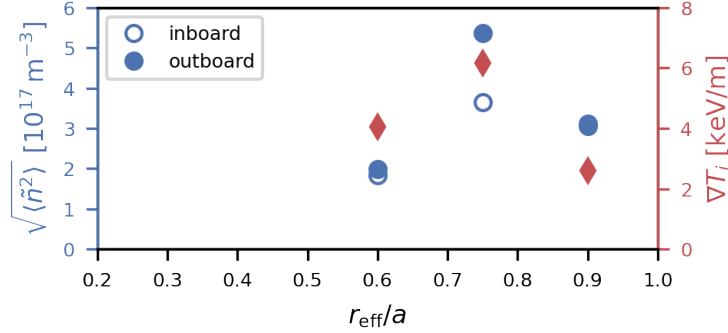


Figure 6.15: Local density fluctuations from nonlinear GENE flux tube simulations and ion temperature gradient at the corresponding radial position. The density fluctuations are evaluated at the intersection with the PCI LOS on the inboard and outboard side, respectively. Reproduced from BÄHNER *et al.* [133].

electromagnetic effects. Figure 6.15 shows the resulting density fluctuations as well as the ion temperature gradient for each flux tube versus the radial position. The density fluctuations are evaluated at the intersection with the PCI LOS on the in- and outboard side, but the respective values only show a clear difference at $r_{\text{eff}}/a = 0.75$. This can be understood from the mode structure along the flux tube, which was presented in section 4.1.2, figure 4.7. The data stems from the same simulation and shows a clear increase of density fluctuations towards the outboard side at $r_{\text{eff}}/a = 0.75$. This asymmetry between the in- and outboard side fits the experimental observation in the (k, f) -spectrum. The amplitude structure of the simulated density fluctuations along the flux tube at $r_{\text{eff}}/a = 0.6$ and $r_{\text{eff}}/a = 0.9$ is rather flat, which results in the small difference between the PCI in- and outboard measurement position at those radial locations. Both density fluctuations and ion temperature gradient are strongest in the $r_{\text{eff}}/a = 0.75$ flux tube and decrease again towards the separatrix, which shows how closely the nonlinear density fluctuations relate to the linear drive of the ITG mode. This is the numerical confirmation that the fluctuations are indeed strongest at $r_{\text{eff}}/a = 0.75$, as was already derived from the comparison of the dominant phase velocity in the PCI measurement to the neoclassical $v_{\mathbf{E} \times \mathbf{B}}$.

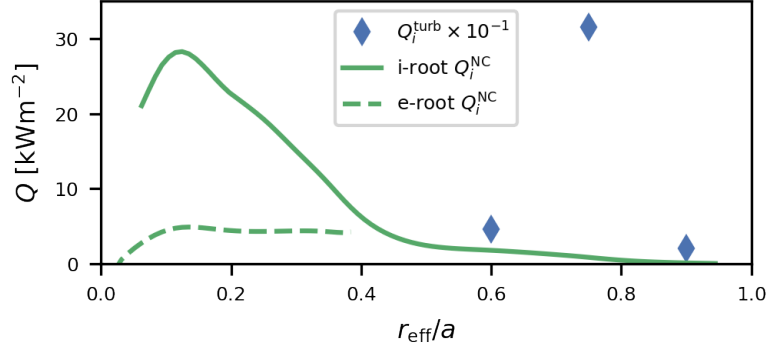


Figure 6.16: Ion heat flux from neoclassical simulations with DKES and flux tube averaged values from gyrokinetic simulations with GENE. The turbulent heat flux from gyrokinetic flux tube simulations is known to be overestimated and is artificially reduced by a factor of 10 for illustration.

In the last part of this section, the implications for transport are briefly discussed. As mentioned before, this discussion is limited since density fluctuations are only a proxy for turbulent transport. Nevertheless, the good agreement between the experimental findings for the location of strongest density fluctuations with the simulation results presented in this section give confidence in the qualitative radial evolution of turbulent transport which can be deduced from the nonlinear flux tube simulations. Figure 6.16 shows the flux tube averaged ion heat flux in real units for the three radial positions in blue. Similarly to the evolution of the density fluctuations, the $r_{\text{eff}}/a = 0.75$ flux tube exhibits by far the strongest transport. The neoclassical ion heat flux from the simulations with DKES is shown in green for comparison. It is taken from the same simulations which produced the radial electric field of the reference discharge for the velocity comparison (cf. figure 6.4). The neoclassical ion heat flux peaks further in the core of the plasma at $r_{\text{eff}}/a < 0.2$ and decreases strongly in the outer half of the plasma. This fits the qualitative understanding that the outer half of the plasma exhibits a stronger turbulent heat flux than the core. It has, however, been previously shown that for this type of discharge (cf. section 6.1), the transport is predominantly anomalous throughout the whole plasma radius and the neoclassical transport only accounts for $\approx 10\%$ of the total input power

for both electrons, ions and the combined case [20]. It is therefore likely that the radial evolution of turbulent ion heat flux as shown in figure 6.16 is exaggerated and global gyrokinetic simulations with similar parameters would yield a more evenly distributed radial ion heat flux profile. For a quantitative and self-consistent comparison of the two transport channels, a full power balance is required, as presented in [20]. This includes radial ray-tracing of ECRH power deposition, tomography inversion of radiated power and a numerical 1-dimensional transport analysis, which exceeds the scope of this work. Nevertheless, it can be concluded that the turbulent ion heat transport connected to the measured density fluctuations is likely to be strongest at the same radial position as the density fluctuations, $r_{\text{eff}}/a \approx 0.75$.

7

Zonal-flow-like modulations of the binormal flow velocity

In the previous section it was shown that the dominant propagation velocity of density fluctuations measured by the PCI diagnostic can be associated to the $\mathbf{E} \times \mathbf{B}$ flow at a certain radius in the plasma. In the presented analysis, the PCI (k, f) -spectra are averaged over a time period of typically $\gtrsim 1$ s, since the kinetic profiles are constant during this time and thus the NC transport and the ambipolar radial electric field do not vary. The minimum segment length which is needed to determine a dominant phase velocity in the PCI spectrum is, however, as short as 0.05 ms. This allows for an investigation of the propagation velocity evolution on a time scale which is much faster than changes of the ambipolar electric field. On this time scale, a persistent feature becomes apparent throughout every discharge: the dominant phase velocity is modulated at frequencies on the order of 0.1 to 1 kHz. The entire region of strong PSD amplitude is shifted up and down over the entire wavenumber axis, which is visible in the example (k, f) -spectrum depicted in figure 7.1. For illustration, only the negative wavenumber branch is depicted, but the positive wavenumber branch exhibits the same behaviour. This phenomenon is reminiscent of ZFs, which act as a turbulence driven modulation of the binormal plasma flow. As discussed in section 3.4, ZFs are expected to arise in W7-X as a saturation mechanism for drift wave turbulence, but so far they have not been measured in W7-X. An identification of the observed oscillations as ZFs is challenging with the currently available data and an alternative interpretation of the oscillations as large scale, global MHD modes exists. Therefore, the remainder of this section is

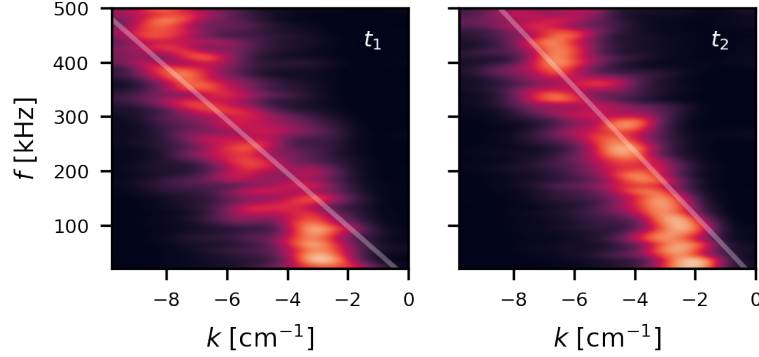


Figure 7.1: Two frames of a (k, f) -spectrum for illustration of the dominant phase velocity oscillation. The two frames have a time difference of $\Delta t = t_2 - t_1 = 2$ ms, exhibiting a difference in the dominant phase velocity of 640 m s^{-1} . The fluctuation band oscillates up and down over the entire wavenumber axis.

organised in two parts: first, in sections 7.1 to 7.3, the observed oscillation is characterised neutrally without reference to either one of the hypotheses. In the second part, sections 7.4 to 7.6, the observations are interpreted in the context of ZFs and global MHD modes.

The detailed structure is as follows: In section 7.1, the general characteristics of the oscillation are presented. A large part of the characterisation consists of correlation analyses to other plasma parameters. This is motivated by the role of ZFs and global modes in the relation between these parameters. A strong dependence on the magnetic field configuration leads to a distinction of two cases, which are described in section 7.2. In one of the two cases, a feature in the 1 to 2 kHz frequency range is observed, which can be associated with a previously characterised 1 to 2 kHz mode [165]. This connection is briefly discussed in section 7.3. In section 7.4, the observations are interpreted in the context of ZFs. Simulation results and modelling of ZFs are described in section 7.5. Finally, in section 7.6, the alternative interpretation of the observations as global modes is provided.

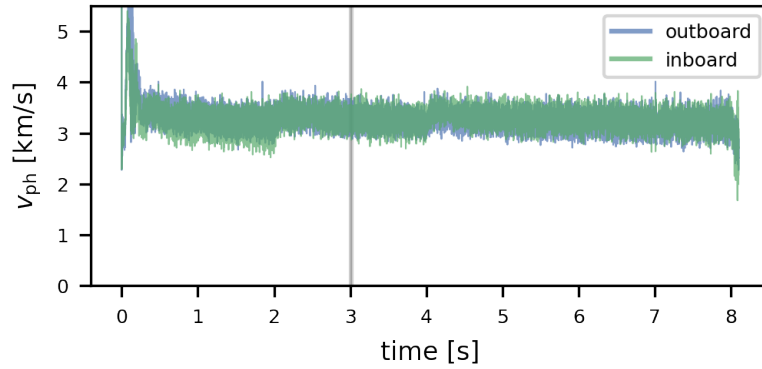
7.1 Characterisation

7.1.1 Temporal evolution

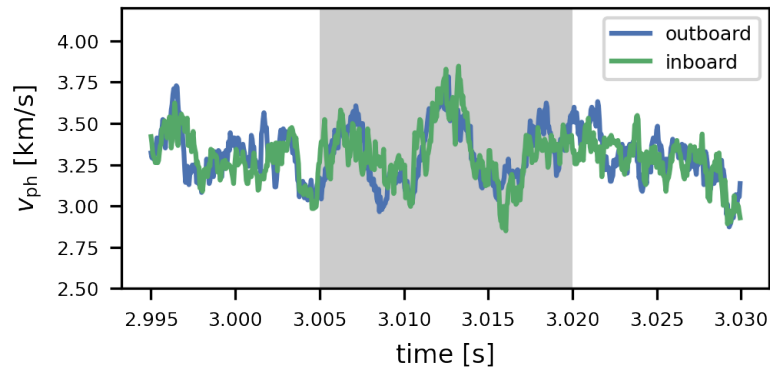
For the analysis of the temporal evolution of the binormal flow velocity throughout an entire discharge, an automatic algorithm is required. The high time resolution is achieved by reducing the length of the time segment for the (k, f) -spectrum calculation to $\Delta t = 0.05$ ms. This reduces the frequency resolution to $\Delta f = 10$ kHz, which is still sufficient for the determination of a dominant phase velocity. Following Welch's method, ten spectra are averaged in order to reduce spectral variance. The resulting averaging window of 0.5 ms is shifted by Δt for the next time step similarly to a moving average, which retains the high time resolution for the detection of changes in the phase velocity. For each discharge, the set of parameters for the determination the dominant phase velocity (cf. section 4.2.4) is selected individually to ensure a robust analysis throughout the discharge. In previous operation phases of W7-X, reference discharges with fixed density and input power settings were run in every magnetic configuration. A time segment of such a reference discharge is used for the comparison of different configurations in the following sections. Figure 7.2 shows the time traces of the inboard (positive k) and outboard (negative k) dominant phase velocity for an example discharge. The phase velocities exhibit an oscillation throughout the entire discharge. For simplicity, the phase velocity in the spectrum is not converted to the adequate binormal flow velocity under assumption of a radial origin (as in chapter 6), since the projection is constant in time and independent of the observed modulation. In figure 7.2a, the full discharge is shown, where the steps of input power, which affect the stationary neoclassical $\mathbf{E} \times \mathbf{B}$ flow, are visible at 2 s and 4 s. A small section of the displayed time trace is shown in figure 7.2b, where the irregular modulation of the phase velocity is visible. In this example, in- and outboard side flow velocity are modulated in phase on the time scale of several ms. In other examples, there is a cross-phase of π between the velocity time traces.

7.1.2 Cross-correlation to other signals

There is a number of quantities which exhibit a correlation to the oscillation of the dominant phase velocity. First, there is a strong correlation to

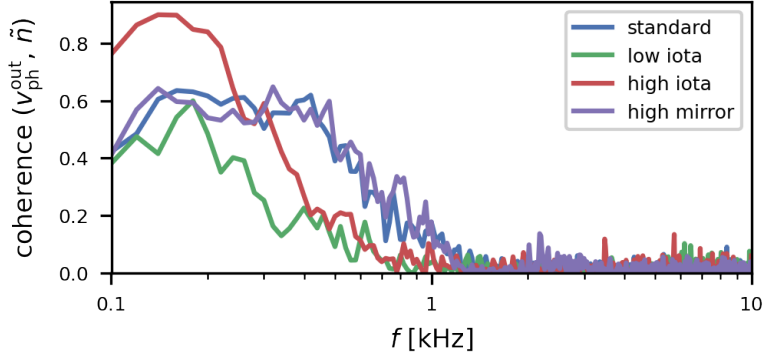


(a) Outboard and inboard side dominant phase velocity during the discharge. Input power steps at 2 s and 4 s are visible in the mean phase velocity.

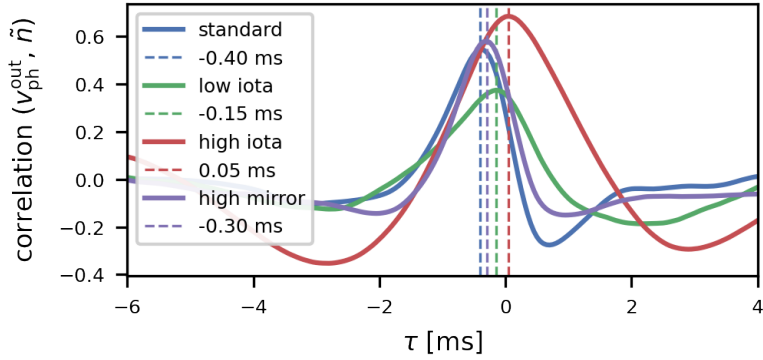


(b) Visible synchronous oscillation of dominant phase velocities on a ms time scale.

Figure 7.2: Time traces of in- and outboard dominant phase velocity in PCI spectra of an example discharge in high iota configuration (W7-X XP:20180904.004). The overview of the entire discharge is shown in (a) and a zoomed in view of the same data in (b).



(a) Coherence.



(b) Correlation function.

Figure 7.3: Coherence (a) and correlation (b) of dominant phase velocity and the density fluctuation amplitude for different magnetic configurations. The dotted lines in (b) mark the lag between the signals.

the density fluctuation amplitude as obtained by integration of the (k, f) -spectrum at every time step within the boundaries which were used for the determination of the phase velocity. Figure 7.3 shows the coherence (a) and the correlation function (b) of the dominant phase velocity and the density fluctuation amplitude for reference discharges in the W7-X standard, low iota, high iota and high mirror magnetic configuration. The coherence between the phase velocity oscillation and the density fluctuation amplitude exhibits large values at frequencies of 0.2 to 1 kHz in every configuration.

The correlation function in figure 7.3b shows a relatively strong positive correlation for each configuration and peaks at a time lag close to $\tau = 0$. The maximum position of the correlation function is marked by dashed lines and can be interpreted as the lag between the signals. In the depicted cases, the lag is -0.40 to 0.05 ms, which is close to the minimum resolvable time lag of $\Delta\tau = 0.05$ ms. The phase velocity evolves almost at the same time but generally a few $100 \mu\text{s}$ after the density fluctuation amplitude. It is important to keep in mind that the two signals represent different quantities and that the phase velocity fluctuation does not directly correspond to a density fluctuation. They are not completely independent measurements either, however, since they are derived from the same (k, f) -spectrum. A correlation analysis to the time resolved root mean square (RMS) of a single PCI channel signal shows a qualitatively similar correlation and lag in each configuration albeit at lower correlation values (maximum values of 0.15 to 0.4). In particular the chronological behaviour of the phase velocity modulation having a delay to the density fluctuation amplitude of up to a few $100 \mu\text{s}$ is observed in every case.

Furthermore, a remarkably strong correlation is observed to fluctuations of the H_α line-radiation measured by a filterscope system [166] observing the outboard side SOL close to the measurement position of the PCI diagnostic. Even though the two measurements are radially separated, a correlation and coherence of more than 0.8 is observed. A connection of the two signals via electric or mechanical coupling is implausible and other indirect correlations e. g. due to a measurement of soft X-ray (SXR) emission in the plasma core by the filterscope could be excluded. The correlation to the H_α line-radiation is further investigated in the next section.

A correlation to SXR emission in the plasma core was investigated via a single LOS signal of the soft X-ray Multi Camera Tomography System (XMCTS) [167, 168]. High correlation between the signals is observed but at a much lower level as compared to the H_α signal. The signals are coherent predominantly at frequency below 300 Hz. Further analysis of this correlation is described in section 7.3. Similarly, there is some correlation to magnetic signals from segmented Rogowski coils [169] and Mirnov coils [170]. The coherence of the phase velocity oscillation and the Rogowski coil measurement can be as large as 0.8 in the high iota configuration at a frequency of 200 Hz and exhibits a second peak at 2.5 kHz. The correlation to the Mirnov coil signal is observed exclusively in the 1 to 2 kHz frequency range

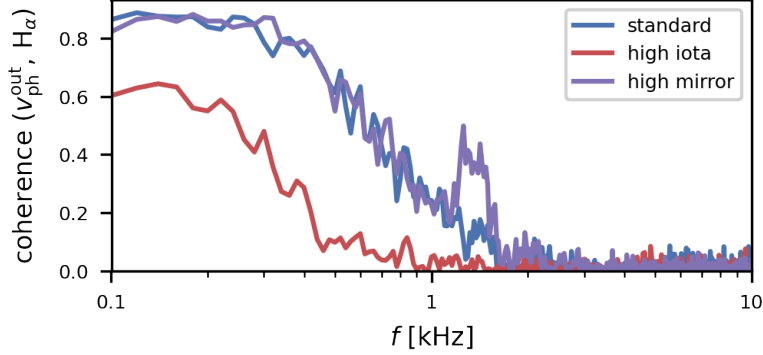


Figure 7.4: Coherence of dominant phase velocity and H_α line-radiation from the SOL for different magnetic configurations.

in certain configurations.

Finally, a similar modulation of the binormal flow velocity as in the PCI data is observed by DBS and the PCR. No direct correlation analysis between to the PCI v_{ph} oscillation has been done yet.

7.2 Magnetic configuration dependency

A remarkable feature of the dominant phase velocity oscillation is the strong dependence on the magnetic configuration. The spectral properties and correlations to other signals are qualitatively different between certain magnetic configurations and qualitatively similar for others. Two cases can be identified: first, the standard and high mirror configuration and secondly, the low and high iota configuration. Since the most obvious difference between the two groups is the ι -profile (cf. figure 2.9), they are referred to as medium range ι (M- ι) and low and high ι (LH- ι) in the following. There are, however, other differences between the configurations, such as magnetic curvature or magnetic shear, which might have an equal or more important impact on the mechanism which causes the flow velocity oscillation.

The spectral differences between the cases can be observed well in the coherency spectrum of the outboard side dominant phase velocity to the H_α radiation, which is depicted in figure 7.4. The coherency spectrum is broad

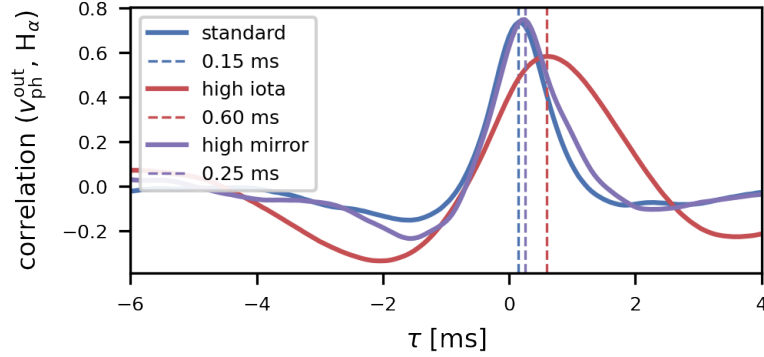
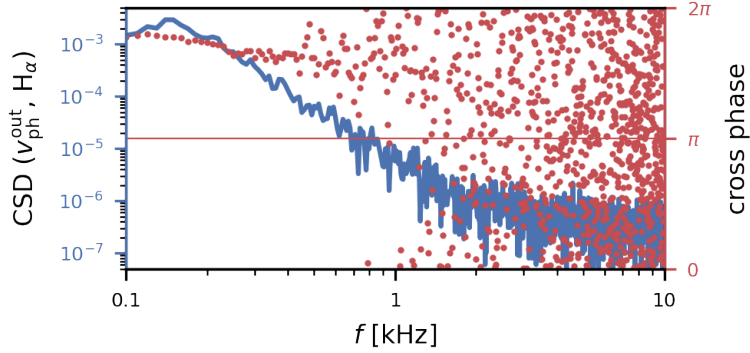
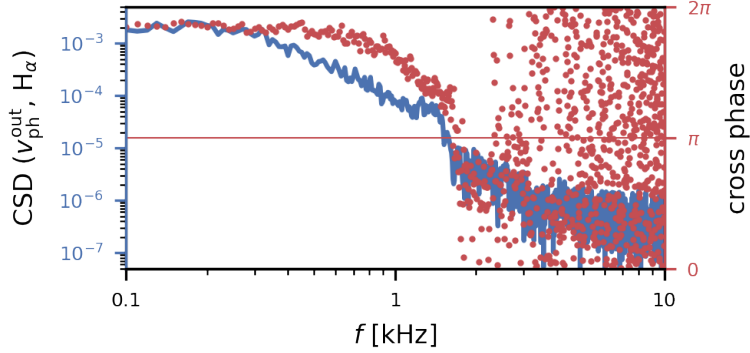


Figure 7.5: Correlation function of the dominant outboard phase velocity and the H_α -radiation for different magnetic configurations. The dotted lines mark the lag between the signals.

at low frequencies, peaks at 200 to 300 Hz and shows considerable coherence up to 1 kHz for the M- ι configurations. For the LH- ι configurations, the spectrum is narrower, peaks at 200 Hz or below and considerable coherence is only observed up to 500 Hz. Unfortunately, no suitable data is currently available for a comparison in the low iota configuration. Nevertheless, the respective properties are observed for each configuration in the coherence spectrum with other quantities, e. g. the density fluctuation amplitude in figure 7.3a. Another distinct difference between the two cases is a mode between 1 and 2 kHz, which is observed as a peak in the coherency spectrum at that frequency. In figure 7.4, this is most apparent for the high mirror configuration but the mode is consistently observed in the standard configuration as well. The spectrum of the standard configuration only exhibits a small peak in that frequency range in the selected time window. In the LH- ι case, this mode is not observed. Figure 7.5 shows the correlation function for each case. A strong positive correlation between the signals is observed. Generally, the lag is positive i. e. the H_α radiation is delayed with respect to the flow velocity oscillation. A quantitative discussion of the lag between the oscillations is not possible at this point due to unknown timing offsets between the diagnostic measurements in the range of several 10 to 100 μ s. Figure 7.6 shows the CSD and the cross-phase between the dominant phase velocity and the H_α radiation for the LH- ι case (a) and the M- ι case



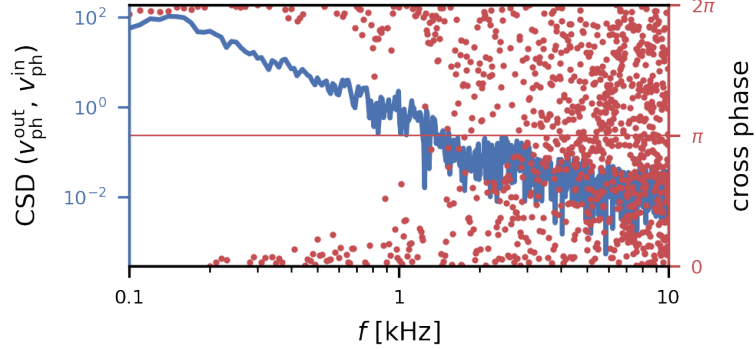
(a) LH- ι case: W7-X XP:20180904.004, high iota, 2 to 4 s.



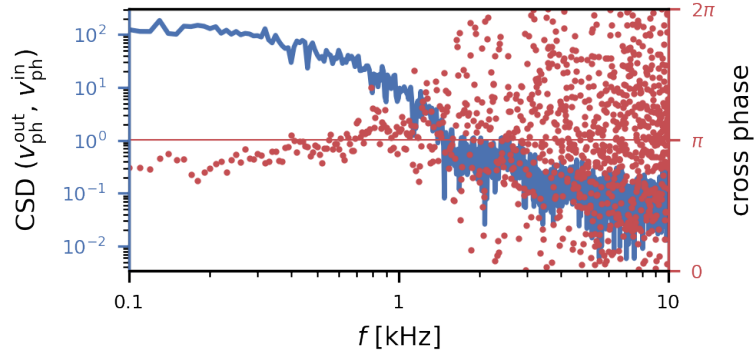
(b) M- ι case: W7-X XP:20180911.007, high mirror, 2 to 4 s.

Figure 7.6: CSD (blue) and cross-phase (red) of outboard dominant phase velocity in PCI spectrum and H_α radiation. The LH- ι case is shown in (a) and the M- ι case in (b).

(b). The spectral differences between the two cases are also visible in the CSD, in particular the 1 to 2 kHz feature. In both cases, the cross-phase is well defined in the low-frequency range, where the signals are most coherent. It is just below 2π at the lower boundary of the frequency range and slowly decreases towards higher frequencies indicating a low constant time lag between the signals rather than a fixed cross-phase. In the LH- ι case, the cross-phase becomes random above 1 kHz due to the vanishing coherence. In the M- ι case, it changes abruptly above the 1 to 2 kHz mode



(a) LH- l case: W7-X XP:20180904.004, high iota, 2 to 4 s.



(b) M- l case: W7-X XP:20180911.007, high mirror, 2 to 4 s.

Figure 7.7: CSD (blue) and cross-phase (red) of in- and outboard dominant phase velocity in PCI spectra. The LH- l case is shown in (a), where the velocities oscillate in phase, and the M- l case is shown in (b), where the velocities oscillate with a phase shift of π .

and is random only above 3 kHz.

Another distinct difference between the LH- l and the M- l case is the cross-phase between the in- and outboard side dominant phase velocity. Figure 7.7 shows the CSD and cross-phase for the two cases in (a) and (b), respectively. The CSD shows similar features as for the comparison to the H_α radiation. The cross-phase, however, is persistently different for the two cases: in the LH- l case, the flow velocities on both sides of the plasma oscillate in phase

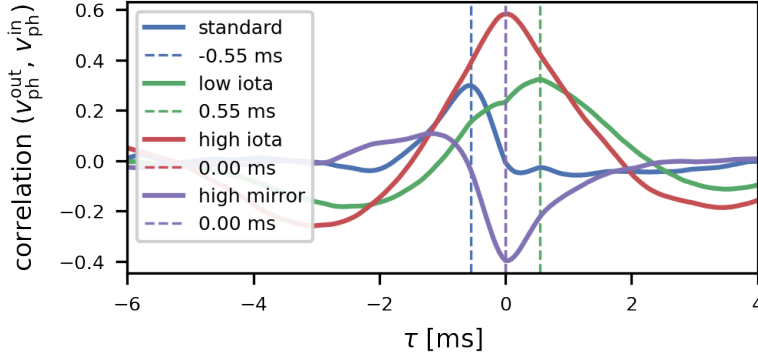


Figure 7.8: Correlation function of outboard and inboard dominant phase velocity for different magnetic configurations. The dotted lines mark the lag between the signals.

for all frequencies up to 2 kHz, where it becomes random. In the M- ι case, there is a phase of π between the two sides. Accordingly, the correlation between in- and outboard side phase velocity, which is shown in figure 7.8, is generally strongly positive for the LH- ι case and negative in the M- ι case.

7.3 1-2 kHz feature in the medium range iota case

In this section, the characteristics and the implication of the 1 to 2 kHz feature of the binormal flow velocity in M- ι case discharges is described. There has previously been a report on a 1 to 2 kHz mode in W7-X by BALLINGER *et al.* [165]: it was first observed in the visible light emission in the island divertor region of W7-X. The mode mostly appeared in $5/5$ -island configurations (i. e. the M- ι case) and is strongly suppressed in others (i. e. the LH- ι case). It was measured in various quantities, such as the line-averaged density, the diamagnetic energy, the magnetic flux, in SXR emission and by probes measuring the floating potential and the ion saturation current on the MPM in the SOL of the plasma. The measurements imply a toroidal mode number of $n = 0$ and a finite but low poloidal mode number, $m \neq 0$. The radial origin is not entirely clear, since it was measured in core

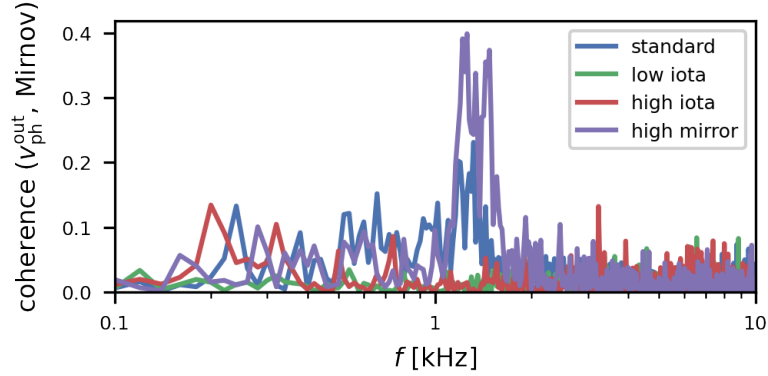


Figure 7.9: Coherence of dominant phase velocity and magnetic perturbations measured by Mirnov-coils for different magnetic configurations. The signals are only coherent if there exists a 1 to 2 kHz feature.

plasma quantities as well as in the SOL. The appearance of the mode is not connected to a decrease of the diamagnetic energy, which is the case for other large scale MHD or sound modes [171]. It is likely to be driven by the electron temperature gradient and not by pressure or plasma current. Finally, the origin and nature of the mode could not be resolved, yet [165].

Because of the frequency range, the magnetic configuration dependency, the connection to visible light from the SOL and SXR emission from the core of the plasma, the 1 to 2 kHz feature of the binormal flow velocity is identified as the mode described by BALLINGER *et al.* [165]. As mentioned above, the mode was also measured by magnetic flux diagnostics, which motivates a cross-coherence analysis of the dominant phase velocity signal to magnetic fluctuations measured by Mirnov coils. Figure 7.9 shows the coherency spectrum of the two quantities. As mentioned in section 7.1, there is very low coherence across the entire frequency regime except between 1 and 2 kHz in the M- ι case. Only the 1 to 2 kHz mode causes magnetic perturbations which are measurable by Mirnov coils. Other spectral parts of the flow velocity oscillation do not correlate to anything measured by Mirnov coils. It was mentioned in section 7.1 that the dominant phase velocity oscillation shows coherence with the SXR emission measured by a single LOS signal of the XMCTS diagnostic. The corresponding coherency spectrum is depicted in figure 7.10. The coherence is largest for low frequencies in

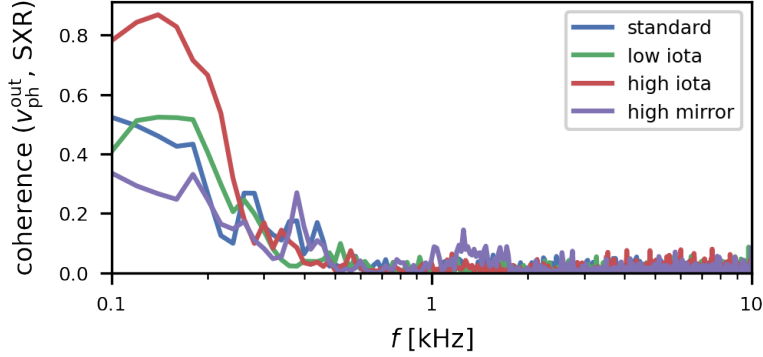


Figure 7.10: Coherence of dominant phase velocity and SXR emission measured by XMCTS for different magnetic configurations.

every configuration and there is a small peak between 1 and 2 kHz in case of the high mirror configuration. Otherwise, no major differences between the configurations are observed.

In the previous study of the mode, only single LOS measurements were analysed and a set of Mirnov coils in a poloidal arrangement was used to estimate the poloidal mode number. The measurements revealed strong $m = 2$ and $m = -3$ components of the fluctuation data [165]. The poloidal mode number estimation by the Mirnov coils is most accurate for modes in the edge of the plasma or in the SOL and becomes more uncertain for modes in the core due to a changing flux surface shape [170]. In this work, detailed tomograms of the SXR emission by the XMCTS^I are used for a poloidal mode number analysis with radial resolution. Figure 7.11 shows SXR tomograms during a phase of significant occurrence of the 1 to 2 kHz mode. The left panel depicts the unfiltered tomogram. The stationary emission follows the geometry of the flux surfaces from equilibrium calculations by the variational moments equilibrium code (VMEC) [172] but barely shows any additional features. A time series of tomograms was calculated for a window of length 15 ms. In order to make dynamic structures on the kHz time scale visible, a band pass is applied to the tomogram data. The band pass effectively removes the stationary and slowly evolving equilibrium radiation as well as numerical noise on very short time scales. The right panel shows the time

^Icourtesy of C. Brandt

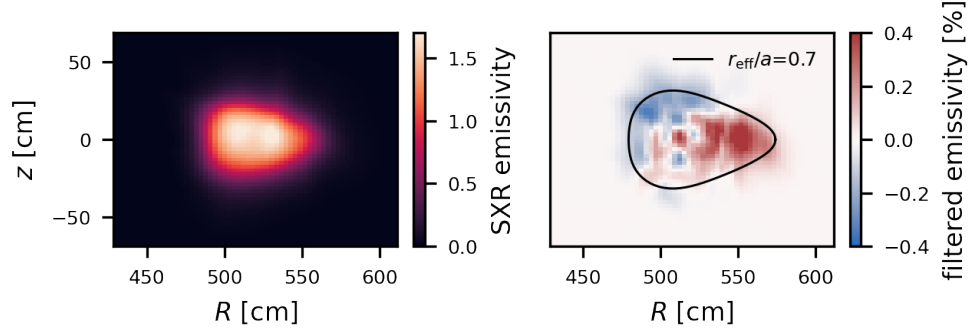


Figure 7.11: XMCTS tomograms of SXR emission during a 1 to 2 kHz feature. The unfiltered tomogram is shown on the left, exhibiting a strong background signal. On the right, a filtered tomogram is depicted, where an $m = 1$ mode is visible. The black line shows the flux surface at $r_{\text{eff}}/a = 0.7$.

frame of the filtered tomogram series which corresponds to the unfiltered tomogram on the left. A dominant $m = 1$ structure is visible, which extends over a large radial region around and within $r_{\text{eff}}/a = 0.7$, indicated by the black line. The filtered data is normalised to the maximum value of the unfiltered tomogram. Only values up to $\pm 0.4\%$ of the maximum emissivity are reached, i. e. the perturbation by the observed mode is small compared to the stationary plasma emission. The $m = 1$ structure rotates in the $\mathbf{E} \times \mathbf{B}$ direction at a frequency of $f = 1.4$ kHz, which fits the frequency observed in the PCI dominant phase velocity oscillation.

The mode intensity varies within the investigated time interval, which is seen in the SXR tomogram data as well as the time trace of the out-board dominant phase velocity. In figure 7.12, a direct comparison of the temporal evolution of the PCI dominant phase velocity and the $m = 1$ mode component in the SXR tomograms is shown. For the poloidal mode decomposition^{II}, equilibrium calculations by VMEC are used in order to locate flux surfaces in the tomogram. The mode spectrum is then obtained via a Fourier transform along these flux surfaces at various radii. The middle panel of figure 7.12 shows the amplitude of the lowest 15 poloidal mode

^{II}courtesy of C. Brandt

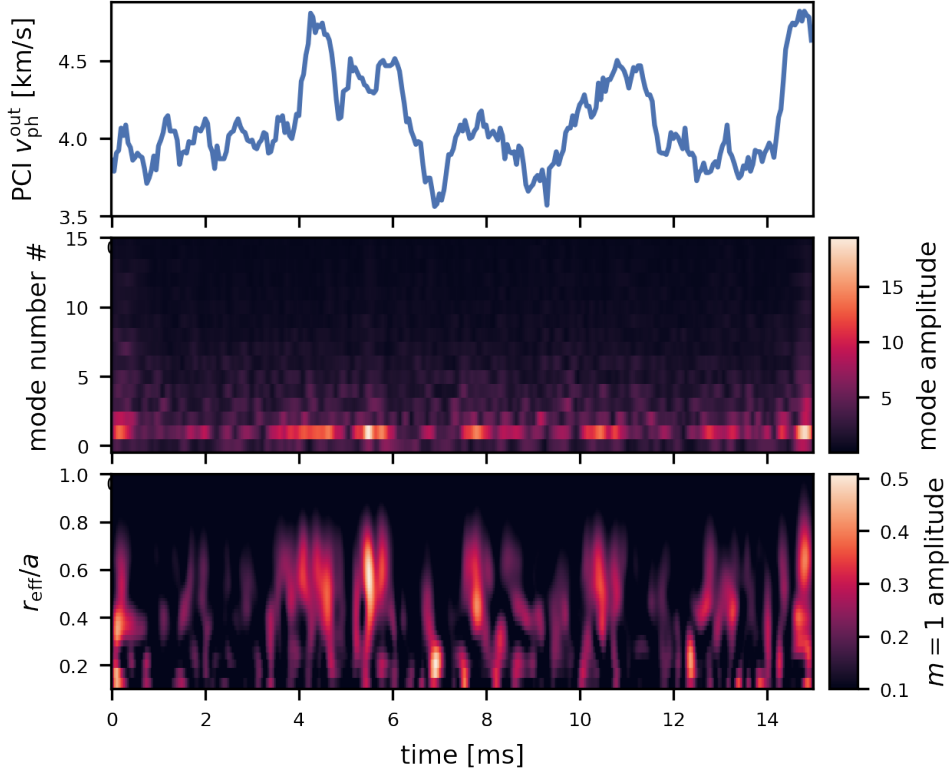


Figure 7.12: Temporal evolution of poloidal mode decomposition during a 1-2 kHz feature. The top panel shows the time trace of the outboard side dominant phase velocity by PCI. The middle panel shows the poloidal mode decomposition (averaged over the radius) of the SXR tomogram by the XMCTS, exhibiting a strong $m = 1$ component. The lower panel shows the radial profile of the $m = 1$ mode amplitude in the SXR tomogram.

numbers averaged over all radii. The $m = 1$ component exhibits the highest amplitude at most times, but varies noticeably with time. The lower panel of figure 7.12 shows the radial amplitude profile of the $m = 1$ component. The mode generally seems to be located between $r_{\text{eff}}/a = 0.5$ and 0.8 . The temporal evolution of the mode amplitude coincides with an increase of the PCI dominant phase velocity (upper panel). Particularly when the mode has a large amplitude at $r_{\text{eff}}/a = 0.7$, a clear response of the phase velocity

is visible.

These observations suggest that the $m = 1$ structure observed in the filtered tomogram is indeed the 1 to 2 kHz mode. It is rotated by the neoclassical $\mathbf{E} \times \mathbf{B}$ rotation, which was already surmised in the previous work [165]. Additionally, there is evidence for a radial origin between $r_{\text{eff}}/a = 0.5$ and 0.8, which covers the region of strong turbulent density fluctuations. At a radius of $r_{\text{eff}}/a = 0.7$, the observed frequency, $f = 1.4$ kHz, translates to a poloidal velocity of $v_{\text{pol}} = 4 \text{ km s}^{-1}$, which roughly matches the magnitude of the $\mathbf{E} \times \mathbf{B}$ rotation velocity obtained from DKES calculations at that radius. The PCI binormal flow velocity matches the $\mathbf{E} \times \mathbf{B}$ rotation velocity around the same radius. A density perturbation of this size can not be resolved by the PCI diagnostic but it is accompanied by a poloidally asymmetric perturbation of the plasma potential due to a fast electron response, which causes a poloidally asymmetric flow pattern. This causes an oscillation of the propagation velocity of small scale density fluctuations as the mode rotates through the PCI LOS. The $m = 1$ structure is likely to cause the phase shift of π between the in- and outboard flow velocity in the respective frequency range (cf. figure 7.7b). The nature and drive of the mode remains unclear. At the time of writing, efforts were started to investigate a possible connection to ZFs via simulations with EUTERPE.

7.4 Zonal flow hypothesis

In section 3.4, zonal flows were introduced as the saturation mechanism for electrostatic turbulence in fusion plasmas. They occur in gyrokinetic simulations for W7-X [75, 100, 101] and have been measured on numerous other devices [102]. With respect to the binormal propagation velocity of fluctuations, they act as an additional component to the $\mathbf{E} \times \mathbf{B}$ rotation velocity and the intrinsic mode phase velocity:

$$u_{\alpha} = v_{\text{ph}} + v_{\mathbf{E} \times \mathbf{B}} + u_{\text{ZF}}. \quad (7.1)$$

In contrast to v_{ph} and $v_{\mathbf{E} \times \mathbf{B}}$, the ZF contribution has a dynamic temporal behaviour due to Mishchenko oscillation, GAMs, and limited lifetime [104]. From a theoretical viewpoint, it is hence expected to measure ZFs as an oscillating or fluctuating addition to the $\mathbf{E} \times \mathbf{B}$ mean flow. ZFs are therefore an obvious candidate for the interpretation of the observed flow velocity

oscillations with the exception of the 1 to 2 kHz mode. The experimental observations draw a complex picture and it is difficult to come to definite conclusions, but there are a number of arguments which suggest that the fluctuations in the phase velocity are indeed caused by ZF activity.

7.4.1 Radial and poloidal structure

The radial structure of ZFs, k_r , is of particular interest since not the mean flow itself, but the flow shear is important for the mechanisms of energy transfer and suppression of turbulence (cf. section 3.4). As previously shown, the density fluctuations measured by PCI predominantly originate from a radial region, $r_{\text{eff}}/a \approx 0.7$, at which the dominant phase velocity corresponds to the neoclassical $\mathbf{E} \times \mathbf{B}$ rotation. In order to observe the oscillation of the high spectral power band in the density fluctuation spectrograms, the radial position must be within a zone of the ZF rather than a shear layer.

A key feature of ZF is the toroidal and poloidal symmetry, $(m, n) = (0, 0)$. With the currently available data the toroidal mode number is not accessible. However, with the in- and outboard phase velocity estimates, indications of the poloidal mode structure are obtained. In the LH- ι case, the two velocities oscillate in phase, which is expected for a zonal component, if the two measurement branches correspond to the same radial position. However, any perturbation of the flow velocity with an even poloidal mode number would have the same effect. In the M- ι case, the in- and outboard poloidal flow velocity modulations have a cross-phase of π . If the in- and outboard branch measurement actually correspond to neighbouring zones, they exhibit a cross-phase of π . The cross-phase can on the other hand also be caused by a flow structure with an odd poloidal mode number, as in the case of the 1 to 2 kHz mode. Contrary to the case of the 1 to 2 kHz mode, there are no indications for a poloidal mode structure in SXR tomograms for other frequency components of the flow velocity oscillation.

The idea of different radial measurement positions on the in- and outboard side in the M- ι case is further investigated. In global and flux-tube simulations for W7-X, the radial scale of ZF was identified as $k_r \rho_i = 0.005$ [99, 101]. For $\rho_i = 1.5$ mm (at $r_{\text{eff}}/a = 0.75$), this corresponds to $\lambda_r \approx 0.19$ m $\approx 0.36a$. A radial shift between the measurement positions on in- and outboard side of $0.18a$ would be necessary to measure at a phase shift of π at this k_r . This is not unreasonable, as shown by a velocity comparison as in section 6.4

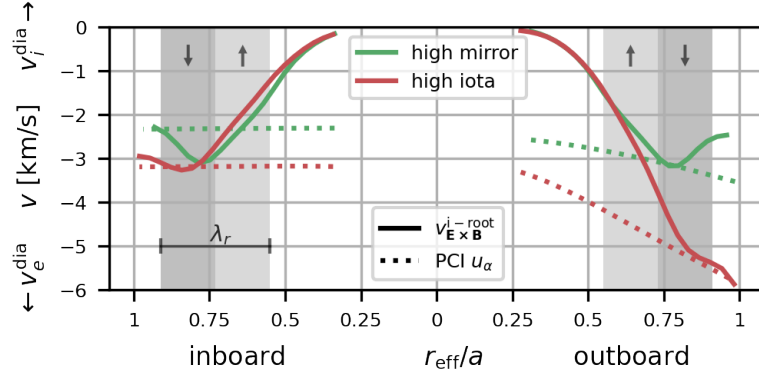


Figure 7.13: Comparison of the $\mathbf{E} \times \mathbf{B}$ velocity and the binormal propagation velocity by PCI for the high mirror and high iota configuration. Electron root solutions for $v_{\mathbf{E} \times \mathbf{B}}$ are not shown. The shaded regions illustrate a possible ZF structure.

applied to discharges in high mirror and high iota configuration. Figure 7.13 shows the comparison for both cases. The shaded regions illustrate a possible ZF structure with the width according to λ_r . For the high iota discharge, the velocities match best at $r_{\text{eff}}/a \approx 0.85$ on both in- and outboard side, even though the projection is quite different for both sides. Since the region where the velocities match is at the same radial location on the in- and outboard side, the measurement reflects the same flow zone. Contrary for the high mirror case: the velocities match best at $r_{\text{eff}}/a \approx 0.75$ on the outboard side but on the inboard side, the lines cross at $r_{\text{eff}}/a \approx 0.65$ and 0.9 , which is an “error” of $\approx 0.15a$ in either direction and therefore enough to correspond to a different flow zone. This was interpreted as a consequence of measurement uncertainties so far, but could also be caused by a poloidal asymmetry in the radial distribution of fluctuations, i. e. by a different measurement position.

Alternatively, it can be argued that the cross-phase of π between the velocity branches in the M- ι -case is indeed due to a $m = 1$ structure of the flow. The turbulence driven zonal potential also has finite mode number components, which are usually small compared to the $(m, n) = (0, 0)$ component. In global simulations with GTC, the $(1, 0)$ component was the most dominant non-zonal component [101]. It depends on the magnetic field structure, in particular the $B_{1,0}$ component of the Fourier decomposition of

the magnetic field [101], which may be the determining difference between the M- ι and LH- ι case. A direct comparison of the two cases with global simulations by EUTERPE is foreseen for the near future.

7.4.2 Cross-correlation to other signals

The correlation of the flow velocity oscillation to other quantities can be compared to expectations from ZFs as well. The correlation to the density fluctuation amplitude indicates an interaction of density fluctuations and flow velocity oscillation. ZFs are turbulence driven, hence this interaction seems natural. The flow velocity oscillation is slightly delayed with respect to the density fluctuation amplitude. The interpretation in terms of ZFs is that the density fluctuations become larger and drive ZFs, which grow in magnitude. The ZFs in turn suppress the density fluctuations via energy transfer and decorrelation. Missing the drive of the fluctuations, the ZFs amplitude eventually becomes smaller again. The lifetime of such a cycle has been measured to be $\tau \approx 1.4$ ms at the compact helical system (CHS) [104], which roughly fits the observed times at W7-X. Mishchenko oscillations [96] are a response of the potential to the magnetic field geometry and not directly driven by fluctuations. If the measured temporal behaviour of the flow velocity corresponds to Mishchenko oscillations, the oscillating flow velocity would modulate the density fluctuations and a reversed delay between the signals is expected. Furthermore, the Mishchenko oscillations occur at a specific frequency which does not vary considerably along the radius. This is not seen in the experimental observations. A possible reason for the missing evidence of Mishchenko oscillations is discussed in the next section.

The remarkably strong correlation to the H_α emission is an indication for a modulation of the particle transport into the SOL. This dynamic transport regulation by ZFs was observed at TJ-II [103] as a correlation between potential measurements with a probe head and H_α monitors in the SOL. ZFs modulate the particle transport into the SOL, which affects the H_α via interaction with recycled particles close to the wall. The time lag between the signals was related to the typical radial velocity from turbulent $\mathbf{E} \times \mathbf{B}$ convective transport. The same qualitative behaviour is found in the present measurements, where the H_α signal is modulated with a short delay with respect to the flow velocity. The timing is not quantitatively compared to a turbulent convective radial velocity because of unknown offsets between

the signals.

In summary, ZFs provide a suitable interpretation of the experimental observations. The oscillating dominant phase velocity is caused by ZFs with limited lifetime. The phase between the inboard and outboard side is either due to a radial offset or a component of the mean flow with finite poloidal mode number. The correlation to the density fluctuation amplitude is a result of the nonlinear interaction of ZFs and turbulent fluctuations. The correlation to the H_α radiation is caused by a modulation of the radial particle transport into the SOL by the ZFs. The ZF picture can, however, not explain the observed correlation to the magnetic perturbation measurement with segmented Rogowski coils. It is not impossible that the strong change of electric potential due to ZFs causes a magnetic perturbation which is measurable by the segmented Rogowski coils close to the plasma vessel, but it is not a typical feature of the ZF phenomenon.

7.5 Zonal flow modelling

The interpretation of the flow velocity oscillations as ZFs is further investigated by modelling efforts. The basis of the discussion is a global gyrokinetic simulation with GENE-3D with adiabatic electrons^{III}. The simulation does not take a neoclassical radial electric field into account and the kinetic profiles are not taken from a specific W7-X situation but are paradigm profiles. The simulation covers radial positions from $r_{\text{eff}}/a = 0.1$ to 0.9. ZFs emerge and cause a saturation by nonlinear interaction with the turbulent fluctuations.

7.5.1 Temporal evolution

Figure 7.14 shows the zonal component, $(m, n) = (0, 0)$, of the electric potential in the plasma for a time period of 0.9 ms in the saturated phase of the simulation. There is a radial structure visible but more prominently a clear oscillation of the potential between positive and negative values. The oscillation is identified as the Mishchenko oscillation and has a frequency of $f = 2.5$ kHz. A similar value was found for W7-X in a semi-analytical approach [97]. If the denormalisation is adjusted to ion temperature values

^{III}courtesy of A. Bañón Navarro

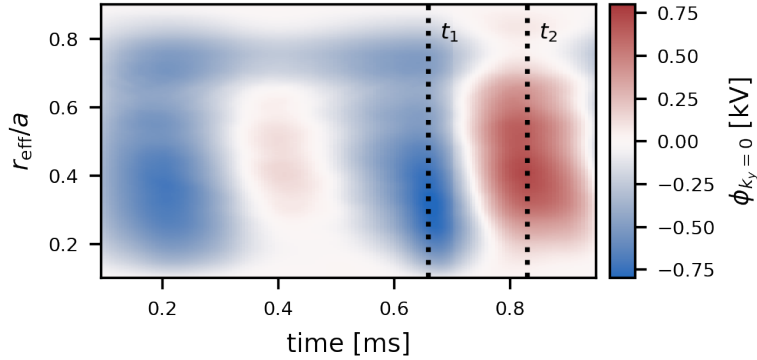


Figure 7.14: Turbulence driven zonal component of the electric potential from a global gyrokinetic simulation with GENE-3D. The Mishchenko oscillation at approximately 2.5 kHz is visible.

observed in the experiment, a frequency of $f = 1.2$ kHz is obtained, which agrees with latest, unpublished calculations with EUTERPE. Since the frequency matches the observed 1 to 2 kHz feature, further efforts are evoked for investigating the $m = 1$ component at this frequency.

7.5.2 Radial structure

A valuable information which can only be obtained from global simulations is the radial structure of the ZF. The radial profile of the zonal potential at two time points, t_1 and t_2 , which are marked by dotted lines in figure 7.14, is analysed. The profile at t_1 reflects the minimum, the profile at t_2 the maximum of the Mishchenko oscillation. The profiles are shown in figure 7.15 as dotted lines. At both time points, the potential peaks in the inner half of the plasma. Outside the half-radius, there is a fixed shape to the profile, which becomes more obvious in the (flux surface averaged) radial electric field, which is shown as solid lines. A distinct peak of the radial electric field at $r_{\text{eff}}/a = 0.7$ is visible at both time points with a well at $r_{\text{eff}}/a = 0.8$ and a shear layer in between. The principle structure is unaffected by the oscillation and the flow does not reverse. Even though the potential changes by up to 1.5 kV at some radii, the radial electric field is only moderately shifted up. This illustrates how the Mishchenko oscillation can be present and and

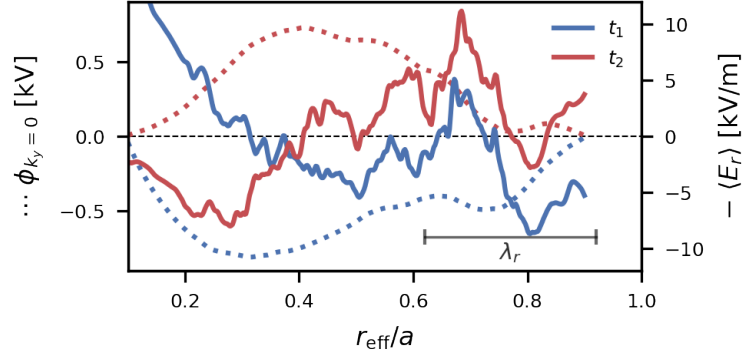


Figure 7.15: Simulated zonal component of the electric potential and corresponding radial electric field at the minimum and the maximum of the Mishchenko oscillation. The time points t_1 and t_2 are marked by vertical dotted lines in figure 7.14.

measurable in the electric potential [98], but difficult to observe in the flow velocity. The peak and well correspond to two large zones in the outer half of the plasma with the width $\lambda_r \approx 0.3a$. This roughly fits the assumptions made in the previous section for the measurement of two neighbouring zones due to a radial offset (cf. figure 7.13). The simulation does not provide any information on the lifetime of ZFs, since the simulated time window is too short. The magnitude of the ZF radial electric field is on the same order of magnitude as the neoclassical radial electric field. This seems exaggerated considering that the time averaged dominant phase velocity generally fits the NC $v_{\mathbf{E} \times \mathbf{B}}$ well. In global gyrokinetic simulations with GTC, the ZF E_r is much smaller than the equilibrium ambipolar field [164]. The effect of the ambipolar electric field on magnitude of the turbulence driven ZF was found to be small in both ion-root and electron-root cases [164].

7.5.3 SPCI modelling

Finally, the impact of the oscillating ZFs on the PCI measurements can be investigated using the SPCI. The ZF radial electric field obtained from the simulation is added to the neoclassical radial electric field as obtained from DKES for an experiment situation and used as input for the simplified

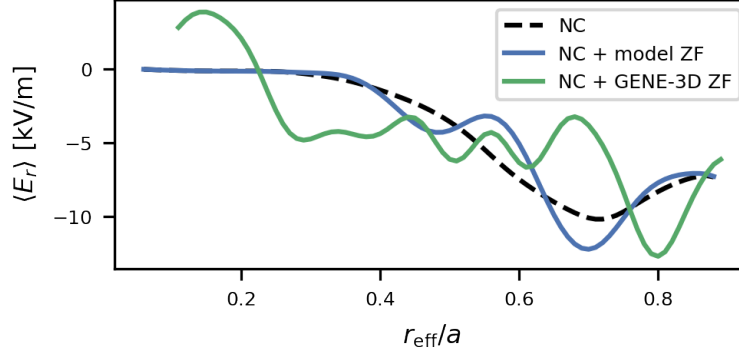


Figure 7.16: Model E_r -profiles for the simplified rotation model of SPCI. The ion-root E_r -profile by DKES calculated for an experimental situation (black dashed line) is used as a baseline. A radial ZF profile from GENE-3D simulations (green) and a model ZF profile (blue) were added to the baseline profile.

rotation model described in section 6.5.

Figure 7.16 shows three radial electric field profiles used for the rotation model of SPCI. The black dashed line represents the ambipolar electric field from DKES as it was already used in section 6.3. For the ZF contribution, the profile of the zonal electric potential in the GENE-3D simulation at $t = (t_2 - t_1)/2$ is used after some smoothing. The sum of the corresponding E_r and the NC field is plotted in green. Additionally, a model profile for the ZF contribution was implemented and added to the NC E_r , which is shown in blue. The model ZF profile has a comparable shape as the GENE-3D outcome but a smaller magnitude and is radially shifted such that a well of the velocity profile still forms at $r_{\text{eff}}/a \approx 0.7$. It is considered a better guess for the underlying ZF structure of the experiment observation. The (k, f) -spectra of the phase contrast signal from SPCI are shown in figure 7.17. The left panel shows the pure NC case as it was already shown in figure 6.13, which is similar to a time averaged experimental (k, f) -spectrum. The middle panels shows the result with the model ZF contribution. The dominant phase velocity is increased and shifted as a whole. Additionally, a second band at a lower velocity is formed on each branch in this particular example, presumably due to the second well in the E_r profile at $r_{\text{eff}}/a \approx 0.5$. The

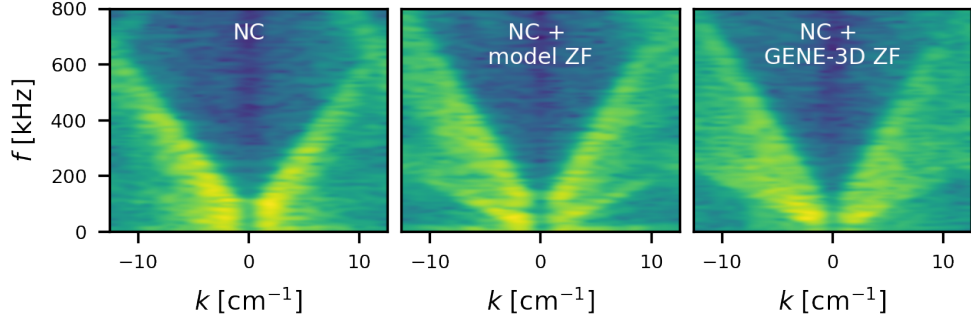


Figure 7.17: Wavenumber-frequency-spectra of SPCI data from the simplified rotation model with velocity profiles corresponding to the E_r -profiles in figure 7.16. The colour scale is in dB.

right panel shows the result with the GENE-3D outcome for the ZF E_r . The power is spread out in (k, f) -space due to the shear layer and the large amplitude of the additional component rather than moving the velocity band up or down. The example with model ZF structure agrees better with experiment observations that then GENE-3D outcome, even though a spread of spectral power as in the latter case is observed occasionally. These results directly show how a ZF contribution to the binormal flow can change the PCI (k, f) -spectrum in a way which fits experimental observations.

7.6 Global mode hypothesis

At the end of the discussion of the oscillating flow velocity, an alternative hypothesis for the observations is provided. Large scale global MHD or sound modes can also partially explain the observations. Due to their large binormal wavelength, these modes can not be directly measured as density perturbations by the PCI diagnostic. If the electric potential perturbation is large enough, it can however act as an additional component to the binormal flow velocity and cause an oscillation of the dominant phase velocity in PCI (k, f) -spectra as the mode moves through the LOS. In favour of this interpretation is a correlation to the magnetic field perturbations measured by segmented Rogowski coils, as briefly described in section 7.1. The signals

are coherent not only for the 1 to 2 kHz mode but also for lower frequency ranges. A similar coherency spectrum was observed between the DBS flow velocity measurement and the segmented Rogowski coil signal. MHD and sound modes are known to cause this kind of perturbation. The poloidally arranged set of segmented Rogowski coils in W7-X can be used to estimate the dominant poloidal mode number at a given frequency. In the high iota discharge, measurements suggest an $m = 1$ structure for the 2.5 kHz component but were inconclusive for the 200 Hz component. In earlier unpublished work^{IV} investigating this component in the DBS flow velocity measurement, a global mode with $(m, n) = (4, 5)$ structure was identified as the origin. This mode is believed to appear at relatively low frequencies of 200 Hz due to a propagation opposite to the $\mathbf{E} \times \mathbf{B}$ rotation and a related downwards Doppler-shift of the frequency. Finally, the sensitivity of these large scale modes on the magnetic field structure and resonances in the ι -profile may be the reason for the qualitative differences between the M- ι and LH- ι case.

It is not clear how a MHD mode would affect the small scale density fluctuation amplitude and the H_α radiation in the SOL in a way to explain the observed strong correlation to the PCI phase velocity oscillation.

^{IV}courtesy of T. Windisch and C. Nührenberg

8

Summary and Conclusion

This work investigates turbulence in the core plasma of the optimised stellarator Wendelstein 7-X. It focuses on experimental characterisation and evaluation of the electrostatic micro-instabilities, which drive turbulent fluctuations, and the saturation of turbulence by zonal flows. The aim is to close the gap between theoretical expectations and experimental understanding for the most fundamental aspects of turbulence in an optimised stellarator such as W7-X. This is the basis for turbulence control and mitigation of turbulent heat loss by means of optimised discharge scenarios or magnetic field configurations in the future.

As a basis for this endeavour, the device-specific theoretical understanding of micro-instabilities was reviewed in chapter 3. Tangible expectations for W7-X were formulated with the help of dedicated linear gyrokinetic simulations in section 3.3.4, which can be summarised as follows: density fluctuations on the ion-scale are relevant for turbulent transport and taken as an experimentally measurable proxy for transport. Fluctuations on this scale are mainly driven by ITG modes, which experience the strongest drive in the outer half of the plasma and which saturate via ZFs. At W7-X, core density fluctuations are measured via PCI, which was introduced in section 4.1. The PCI measurements were found to cover an appropriate poloidal position and range of spatial scales for the investigation of the density fluctuations in question. General and diagnostic-specific analysis tools were introduced in section 4.2 with additional methods developed specifically for this work.

The analysis focuses on ECRH hydrogen discharges with gas-fuelling from the edge, which is the baseline scenario for upcoming long-pulse experiments.

PCI spectra exhibit a power-law dependency on frequency and wavenumber (cf. section 5.1) with a change of spectral index around $k_\alpha \rho_s = 0.8$. This indicates fully developed strong turbulence (as opposed to weak turbulence) and qualitatively fits the fundamental picture of a dual cascade with energy injection at the scale at which ITG modes grow the fastest.

The line-averaged fluctuation level, $\int \tilde{n}_e dl / \bar{n}_e$, is constant for discharges of the same magnetic configuration (cf. section 5.2), mostly due to the self-similarity of the ion temperature and density profiles in the given set of experiments. However, it is found to vary between magnetic configurations in the same parameter space. In particular, the high iota configuration exhibits a lower fluctuation level than others. The reason for the influence of the magnetic configuration could not be conclusively clarified within the framework of this project. Several geometric properties affect ITG turbulence and ZFs in W7-X, including normal and geodesic curvature, local and global shear, rotational transform (also affecting the SOL structure and thus the island divertor) and flux compression (affecting the real space gradients of density and temperature as well as radial flow shear). The reduced fluctuation level in the high iota configuration could, for example, be caused by a reduced linear growth rate or a more effective ZF stabilisation (e.g. through the increased shearing rate). It should be possible to answer this question via a more sophisticated profile-resolved database approach similar to the recent work of CARRALERO *et al.* [173] in combination with linear and non-linear gyrokinetic simulations in different magnetic configurations.

It was shown in chapter 6 that the strongest fluctuations arise at $r_{\text{eff}}/a \approx 0.7$, which is expected on the basis of the linear growth rate of ITG modes. The dominant phase velocity in PCI (k, f)-spectra corresponds to the $\mathbf{E} \times \mathbf{B}$ rotation velocity at that radius, which enables experimental localisation despite the line-integrated nature of the measurement. With a simplified rotation model implemented in the SPCI it was confirmed that suitable radial profiles of density fluctuation amplitude and rotation velocity yield the correct dominant phase velocity. The radial localisation of density fluctuations was confirmed by nonlinear gyrokinetic flux tube simulations. The density fluctuation amplitudes as well as the turbulent ion heat flux were largest in the flux tube at $r_{\text{eff}}/a = 0.75$, which also exhibits the largest ion temperature gradient. The density fluctuations were found to be stronger on the outboard side, both in experimental spectra as well as in the non-linear simulation. This asymmetry arise due to the unevenly distributed

unfavourable curvature, but is less severe than in a tokamak.

Due to the characteristics of the wavenumber spectra, the radial localisation of density fluctuations, and the respective interpretation it is concluded that ITG modes are the dominant instabilities driving turbulent density fluctuations in W7-X. This is the case even towards the edge of the plasma, where density-gradient-driven TEMs are usually dominant in a tokamak. While the dominant drive is clearly through the ion temperature gradient, it is not entirely clear which role trapped electrons and the electron temperature gradient play for turbulence quantitatively. So far, it is not possible to experimentally distinguish a destabilising contribution of trapped electrons to ITG modes from a finite ITEM contribution, since the modes blend into each other. In contrast to ITG modes, ITEMs vanish in regions without trapped electrons and do not necessarily peak in regions of strong bad curvature. There are, however, indications from nonlinear gyrokinetic simulations that the experimentally measurable fully developed fluctuations are distributed similarly in both cases. Furthermore, even though ETG mode growth peaks at large wavenumbers, they considerably contribute to the growth rate at small wavenumbers in some cases (cf. figure 3.6). It was additionally found that there is some destabilising effect of the electron temperature gradient even when ETG modes should be stabilised by a density gradient (cf. figure 3.7).

Finally, strong indications for ZFs are found in fluctuations of the dominant phase velocity, as described in chapter 7. A direct influence of the dominant phase velocity fluctuations on turbulent density fluctuation amplitudes and radial transport is observed, which matches the picture of ZFs as a saturation mechanism for ITG turbulence in W7-X. The currently available data does not allow for a definite conclusion on this matter, but the observations give confidence that this issue can be resolved with dedicated experiments including e.g. the correlation of toroidally separated measurements by PCR, DBS and PCI. A more detailed understanding of the turbulence saturation in W7-X could help control turbulent transport in future devices not only via reduction of micro-instability growth but also via more effective saturation.

Overall, theoretical expectations are met by experimental findings. Turbulence in W7-X is determined by the same fundamental excitation and saturation mechanisms as in a tokamak with important differences and interesting features due to the specific magnetic geometry and the quasi-isodynamicity.

While this conclusion may seem straightforward, the experimental evaluation of expectations is particularly important at this point of turbulence studies at the new device W7-X. It helps identify aspects which require more experimental or theoretical attention. Furthermore, it gives confidence in theory and simulations in the complex magnetic geometry and provides a basis for the understanding of more complex experimental situations such as turbulence reduction by profile shaping.

Bibliography

1. ECKE, R. The Turbulence Problem: An Experimentalist's Perspective. *Los Alamos Science*, 124–141 (2005).
2. *Millennium Problems* Clay Mathematics Institute. <http://www.claymath.org/millennium-problems>.
3. FRISCH, U. Turbulence nears a final answer. *Physics World* **12**, 53. doi:10.1088/2058-7058/12/12/15 (1999).
4. WESSON, J. *Tokamaks* 4th. *International Series of Monographs on Physics* **149**. 812 pages (Oxford University Press, Oxford, 2011).
5. GRIEGER, G., RENNER, H. & WOBIG, H. Wendelstein stellarators. *Nuclear Fusion* **25**, 1231–1242. doi:10.1088/0029-5515/25/9/040 (1985).
6. BOOZER, A. H. What is a stellarator? *Physics of Plasmas* **5**, 1647–1655. doi:10.1063/1.872833 (1998).
7. HELANDER, P. Theory of plasma confinement in non-axisymmetric magnetic fields. *Reports on Progress in Physics* **77**, 087001. doi:10.1088/0034-4885/77/8/087001 (2014).
8. HELANDER, P. *et al.* Stellarator and tokamak plasmas: a comparison. *Plasma Physics and Controlled Fusion* **54**, 124009. doi:10.1088/0741-3335/54/12/124009 (2012).
9. XU, Y. A general comparison between tokamak and stellarator plasmas. *Matter and Radiation at Extremes* **1**, 192–200. doi:10.1016/j.mre.2016.07.001 (2016).
10. WAGNER, F. *et al.* Regime of Improved Confinement and High Beta in Neutral-Beam-Heated Divertor Discharges of the ASDEX Tokamak. *Physical Review Letters* **49**, 1408–1412. doi:10.1103/PhysRevLett.49.1408 (1982).

11. WAGNER, F. A quarter-century of H-mode studies. *Plasma Physics and Controlled Fusion* **49**, B1–B33. doi:10.1088/0741-3335/49/12B/S01 (2007).
12. WAGNER, F. *et al.* Development of an Edge Transport Barrier at the H-Mode Transition of ASDEX. *Physical Review Letters* **53**, 1453–1456. doi:10.1103/PhysRevLett.53.1453 (1984).
13. HORTON, W. Drift waves and transport. *Reviews of Modern Physics* **71**, 735–778. doi:10.1103/RevModPhys.71.735 (1999).
14. DOYLE, E. *et al.* Chapter 2: Plasma confinement and transport. *Nuclear Fusion* **47**, 18–127. doi:10.1088/0029-5515/47/6/S02 (2007).
15. NÜHRENBERG, J. Development of quasi-isodynamic stellarators. *Plasma Physics and Controlled Fusion* **52**, 124003. doi:10.1088/0741-3335/52/12/124003 (2010).
16. BEIDLER, C. *et al.* Physics and Engineering Design for Wendelstein VII-X. *Fusion Technology* **17**, 148–168. doi:10.13182/FST90-A29178 (1990).
17. BEIDLER, C. D. *et al.* Demonstration of reduced neoclassical energy transport in Wendelstein 7-X. *Nature* **596**, 221–226. doi:10.1038/s41586-021-03687-w (2021).
18. KLINGER, T. *et al.* Overview of first Wendelstein 7-X high-performance operation. *Nuclear Fusion* **59**, 112004. doi:10.1088/1741-4326/ab03a7 (2019).
19. GEIGER, B. *et al.* Observation of anomalous impurity transport during low-density experiments in W7-X with laser blow-off injections of iron. *Nuclear Fusion* **59**, 046009. doi:10.1088/1741-4326/aaff71 (2019).
20. BOZHENKOV, S. A. *et al.* High-performance plasmas after pellet injections in Wendelstein 7-X. *Nuclear Fusion* **60**, 066011. doi:10.1088/1741-4326/ab7867 (2020).
21. BEURSKENS, M. N. A. *et al.* Ion temperature clamping in Wendelstein 7-X electron cyclotron heated plasmas. *Nuclear Fusion* **61**, 116072. doi:10.1088/1741-4326/ac1653 (2021).

-
22. HELANDER, P., PROLL, J. H. E. & PLUNK, G. G. Collisionless microinstabilities in stellarators. I. Analytical theory of trapped-particle modes. *Physics of Plasmas* **20**, 122505. doi:10.1063/1.4846818 (2013).
 23. PROLL, J. H. E., XANTHOPOULOS, P. & HELANDER, P. Collisionless microinstabilities in stellarators. II. Numerical simulations. *Physics of Plasmas* **20**, 122506. doi:10.1063/1.4846835 (2013).
 24. PLUNK, G. G. *et al.* Collisionless microinstabilities in stellarators. III. The ion-temperature-gradient mode. *Physics of Plasmas* **21**, 032112. doi:10.1063/1.4868412 (2014).
 25. PLUNK, G. G., CONNOR, J. W. & HELANDER, P. Collisionless microinstabilities in stellarators. Part 4. The ion-driven trapped-electron mode. *Journal of Plasma Physics* **83**. doi:10.1017/S0022377817000605 (2017).
 26. HELANDER, P. *et al.* Advances in stellarator gyrokinetics. *Nuclear Fusion* **55**, 053030. doi:10.1088/0029-5515/55/5/053030 (2015).
 27. ZOCCO, A. *et al.* Threshold for the destabilisation of the ion-temperature-gradient mode in magnetically confined toroidal plasmas. *Journal of Plasma Physics* **84**, 715840101. doi:10.1017/S0022377817000988 (2018).
 28. XANTHOPOULOS, P. *et al.* Turbulence Mechanisms of Enhanced Performance Stellarator Plasmas. *Physical Review Letters* **125**, 075001. doi:10.1103/PhysRevLett.125.075001 (2020).
 29. ALCUSÓN, J. A. *et al.* Suppression of electrostatic micro-instabilities in maximum- J stellarators. *Plasma Physics and Controlled Fusion* **62**, 035005. doi:10.1088/1361-6587/ab630e (2020).
 30. FRISCH, U. *Turbulence: The Legacy of A. N. Kolmogorov* doi:10.1017/CB09781139170666 (Cambridge University Press, 1995).
 31. RICHARDSON, L. F. *Weather prediction by numerical process*, (University Press, Cambridge, 1922).
 32. HEISENBERG, W. & TAYLOR, G. I. On the theory of statistical and isotropic turbulence. *Proceedings of the Royal Society of London. Series A. Mathematical and Physical Sciences* **195**, 402–406. doi:10.1098/rspa.1948.0127 (1948).

33. SCOTT, B. in *Plasma Physics: Confinement, Transport and Collective Effects* (eds DINKLAGE, A. *et al.*) 173–211 (Springer, Berlin, Heidelberg, 2005). doi:10.1007/11360360_8.
34. KRAICHNAN, R. H. Inertial Ranges in Two-Dimensional Turbulence. *The Physics of Fluids* **10**, 1417–1423. doi:10.1063/1.1762301 (1967).
35. STROTH, U. *Plasmaphysik: Phänomene, Grundlagen, Anwendungen* 1. Aufl. 488 pages (Vieweg + Teubner, Wiesbaden, 2011).
36. STROTH, U. in *Plasma Physics: Confinement, Transport and Collective Effects* (eds DINKLAGE, A. *et al.*) 213–267 (Springer, Berlin, Heidelberg, 2005). doi:10.1007/11360360_9.
37. MYNICK, H. E. & HITCHON, W. N. G. Effect of the ambipolar potential on stellarator confinement. **23**, 1053–1059. doi:10.1088/0029-5515/23/8/006 (1983).
38. YOKOYAMA, M. *et al.* Core electron-root confinement (CERC) in helical plasmas. **47**, 1213–1219. doi:10.1088/0029-5515/47/9/018 (2007).
39. HIRSCH, M. *et al.* Major results from the stellarator Wendelstein 7-AS. *Plasma Physics and Controlled Fusion* **50**, 053001. doi:10.1088/0741-3335/50/5/053001 (2008).
40. WEILAND, J. & ZAGORODNY, A. Drift wave theory for transport in tokamaks. *Reviews of Modern Plasma Physics* **3**, 8. doi:10.1007/s41614-019-0029-x (2019).
41. REYNOLDS, O. On the dynamical theory of incompressible viscous fluids and the determination of the criterion. *Philosophical Transactions of the Royal Society of London. (A.)* **186**, 123–164. doi:10.1098/rsta.1895.0004 (1895).
42. HORTON, W. *et al.* Turbulent electron thermal transport in tokamaks. *New Journal of Physics* **5**, 14. doi:10.1088/1367-2630/5/1/314 (2003).
43. BOSCH, H.-S. *et al.* Technical challenges in the construction of the steady-state stellarator Wendelstein 7-X. *Nuclear Fusion* **53**, 126001. doi:10.1088/0029-5515/53/12/126001 (2013).

-
44. PEDERSEN, T. S. *et al.* Confirmation of the topology of the Wendelstein 7-X magnetic field to better than 1:100,000. *Nature Communications* **7**, 13493. doi:10.1038/ncomms13493 (2016).
 45. PEDERSEN, T. S. *et al.* First results from divertor operation in Wendelstein 7-X. *Plasma Physics and Controlled Fusion* **61**, 014035. doi:10.1088/1361-6587/aaec25 (2018).
 46. WOLF, R. C. *et al.* Wendelstein 7-X Program—Demonstration of a Stellarator Option for Fusion Energy. *IEEE Transactions on Plasma Science* **44**, 1466–1471. doi:10.1109/TPS.2016.2564919 (2016).
 47. PERSEO, V. *Impurity flow measurements with Coherence Imaging at Wendelstein 7-X* PhD thesis (University of Greifswald, Greifswald, Germany, 2020).
 48. PROLL, J. H. E. *et al.* Resilience of Quasi-Isodynamic Stellarators against Trapped-Particle Instabilities. *Physical Review Letters* **108**, 245002. doi:10.1103/PhysRevLett.108.245002 (2012).
 49. HELANDER, P. & NÜHRENBERG, J. Bootstrap current and neoclassical transport in quasi-isodynamic stellarators. *Plasma Physics and Controlled Fusion* **51**, 055004. doi:10.1088/0741-3335/51/5/055004 (2009).
 50. GEIGER, J. *et al.* Physics in the magnetic configuration space of W7-X. *Plasma Physics and Controlled Fusion* **57**, 014004. doi:10.1088/0741-3335/57/1/014004 (2014).
 51. WOLF, R. C. *et al.* Performance of Wendelstein 7-X stellarator plasmas during the first divertor operation phase. *Physics of Plasmas* **26**, 082504. doi:10.1063/1.5098761 (2019).
 52. RUTHERFORD, P. H. & FRIEMAN, E. A. Drift Instabilities in General Magnetic Field Configurations. *The Physics of Fluids* **11**, 569–585. doi:10.1063/1.1691954 (1968).
 53. TAYLOR, J. B. & HASTIE, R. J. Stability of general plasma equilibria - I formal theory. *Plasma Physics* **10**, 479–494. doi:10.1088/0032-1028/10/5/301 (1968).
 54. BRIZARD, A. J. & HAHM, T. S. Foundations of nonlinear gyrokinetic theory. *Reviews of Modern Physics* **79**, 421–468. doi:10.1103/RevModPhys.79.421 (2007).

55. CATTO, P. J., TANG, W. M. & BALDWIN, D. E. Generalized gyrokinetics. *Plasma Physics* **23**, 639–650. doi:10.1088/0032-1028/23/7/005 (1981).
56. PLUNK, G. G. *The theory of gyrokinetic turbulence: A multiple-scales approach* PhD thesis (University of California Los Angeles (UCLA), Los Angeles, USA, 2009). arXiv: 0903.1091.
57. PROLL, J. H. E. *Trapped-particle instabilities in quasi-isodynamic stellarators* PhD thesis (University of Greifswald, Greifswald, Germany, 2014). <https://nbn-resolving.org/urn:nbn:de:gbv:9-001733-4>.
58. MIYAMOTO, K. *Plasma Physics for Nuclear Fusion* (The MIT Press, 1980).
59. JENKO, F. *et al.* Electron temperature gradient driven turbulence. *Physics of Plasmas* **7**, 1904–1910. doi:10.1063/1.874014 (2000).
60. MAURER, M. *et al.* GENE-3D: A global gyrokinetic turbulence code for stellarators. *Journal of Computational Physics* **420**, 109694. doi:10.1016/j.jcp.2020.109694 (2020).
61. BAÑÓN NAVARRO, A. *et al.* Global gyrokinetic simulations of ITG turbulence in the magnetic configuration space of the Wendelstein 7-X stellarator. *Plasma Physics and Controlled Fusion* **62**, 105005. doi:10.1088/1361-6587/aba858 (2020).
62. HASEGAWA, A. & MIMA, K. Stationary Spectrum of Strong Turbulence in Magnetized Nonuniform Plasma. *Physical Review Letters* **39**, 205–208. doi:10.1103/PhysRevLett.39.205 (1977).
63. HASEGAWA, A. & MIMA, K. Strong turbulence, self-organization and plasma confinement. *The European Physical Journal H* **43**, 499–521. doi:10.1140/epjh/e2018-90033-4 (2018).
64. HASEGAWA, A. & WAKATANI, M. Plasma Edge Turbulence. *Physical Review Letters* **50**, 682–686. doi:10.1103/PhysRevLett.50.682 (1983).
65. HASEGAWA, A. & WAKATANI, M. Self-organization of electrostatic turbulence in a cylindrical plasma. *Physical Review Letters* **59**, 1581–1584. doi:10.1103/PhysRevLett.59.1581 (1987).

-
66. HASEGAWA, A., MACLENNAN, C. G. & KODAMA, Y. Nonlinear behavior and turbulence spectra of drift waves and Rossby waves. *The Physics of Fluids* **22**, 2122–2129. doi:10.1063/1.862504 (1979).
 67. WEILAND, J. *Stability and Transport in Magnetic Confinement Systems* doi:10.1007/978-1-4614-3743-7 (Springer New York, New York, NY, 2012).
 68. RUDAKOV, L. I. & SAGDEEV, R. Z. Instability of homogeneous attenuated plasma in a strong magnetic field. *Doklady Akademii Nauk SSSR* **138**, 581 (1961).
 69. COPPI, B., ROSENBLUTH, M. N. & SAGDEEV, R. Z. Instabilities due to Temperature Gradients in Complex Magnetic Field Configurations. *The Physics of Fluids* **10**, 582–587. doi:10.1063/1.1762151 (1967).
 70. COPPI, B. & PEGORARO, F. Theory of the ubiquitous mode. *Nuclear Fusion* **17**, 969–993. doi:10.1088/0029-5515/17/5/009 (1977).
 71. HORTON, W., CHOI, D.-I. & TANG, W. M. Toroidal drift modes driven by ion pressure gradients. *The Physics of Fluids* **24**, 1077–1085. doi:10.1063/1.863486 (1981).
 72. ROMANELLI, F. Ion temperature-gradient-driven modes and anomalous ion transport in tokamaks. *Physics of Fluids B: Plasma Physics* **1**, 1018–1025. doi:10.1063/1.859023 (1989).
 73. ADAM, J. C., TANG, W. M. & RUTHERFORD, P. H. Destabilization of the trapped-electron mode by magnetic curvature drift resonances. *The Physics of Fluids* **19**, 561–566. doi:10.1063/1.861489 (1976).
 74. BEER, M. A. & HAMMETT, G. W. Bounce averaged trapped electron fluid equations for plasma turbulence. *Phys. Plasmas* **3**, 6 (1996).
 75. XANTHOPOULOS, P. & JENKO, F. Gyrokinetic analysis of linear microinstabilities for the stellarator Wendelstein 7-X. *Physics of Plasmas* **14**, 042501. doi:10.1063/1.2714328 (2007).

76. RIEMANN, J., KLEIBER, R. & BORCHARDT, M. Effects of radial electric fields on linear ITG instabilities in W7-X and LHD. *Plasma Physics and Controlled Fusion* **58**, 074001. doi:10.1088/0741-3335/58/7/074001 (2016).
77. PLUNK, G. G. *et al.* Stellarators Resist Turbulent Transport on the Electron Larmor Scale. *Physical Review Letters* **122**, 035002. doi:10.1103/PhysRevLett.122.035002 (2019).
78. WEIR, G. M. *et al.* Heat pulse propagation and anomalous electron heat transport measurements on the optimized stellarator W7-X. *Nuclear Fusion* **61**, 056001. doi:10.1088/1741-4326/abea55 (2021).
79. STECHOW, A. v. *et al.* Suppression of core turbulence by profile shaping in Wendelstein 7-X. *submitted to Physical Review Letters*. arXiv: 2010.02160 (2020).
80. DIAMOND, P. H. *et al.* Zonal flows in plasma—a review. *Plasma Physics and Controlled Fusion* **47**, R35–R161. doi:10.1088/0741-3335/47/5/R01 (2005).
81. MANZ, P., RAMISCH, M. & STROTH, U. Physical Mechanism behind Zonal-Flow Generation in Drift-Wave Turbulence. *Physical Review Letters* **103**, 165004. doi:10.1103/PhysRevLett.103.165004 (2009).
82. STRINTZI, D. & JENKO, F. On the relation between secondary and modulational instabilities. *Physics of Plasmas* **14**, 042305. doi:10.1063/1.2720370 (2007).
83. COWLEY, S. C., KULSRUD, R. M. & SUDAN, R. Considerations of ion-temperature-gradient-driven turbulence. *Physics of Fluids B: Plasma Physics* **3**, 2767–2782. doi:10.1063/1.859913 (1991).
84. DIAMOND, P. H. *et al.* Secondary instability in drift wave turbulence as a mechanism for zonal flow and avalanche formation. **41**, 1067–1080. doi:10.1088/0029-5515/41/8/310 (2001).
85. PLUNK, G. G. & NAVARRO, A. B. Nonlinear growth of zonal flows by secondary instability in general magnetic geometry. *New Journal of Physics* **19**, 025009. doi:10.1088/1367-2630/aa5fdf (2017).

-
86. MERZ, F. & JENKO, F. Nonlinear Saturation of Trapped Electron Modes via Perpendicular Particle Diffusion. *Physical Review Letters* **100**, 035005. doi:10.1103/PhysRevLett.100.035005 (2008).
 87. CHEN, L., LIN, Z. & WHITE, R. Excitation of zonal flow by drift waves in toroidal plasmas. *Physics of Plasmas* **7**, 3129–3132. doi:10.1063/1.874222 (2000).
 88. DIAMOND, P. H. & KIM, Y.-B. Theory of mean poloidal flow generation by turbulence. *Physics of Fluids B: Plasma Physics* **3**, 1626–1633. doi:10.1063/1.859681 (1991).
 89. BURRELL, K. H. Effects of ExB velocity shear and magnetic shear on turbulence and transport in magnetic confinement devices. *Physics of Plasmas* **4**, 1499–1518. doi:10.1063/1.872367 (1997).
 90. TERRY, P. W. Suppression of turbulence and transport by sheared flow. *Reviews of Modern Physics* **72**, 109–165. doi:10.1103/RevModPhys.72.109 (2000).
 91. PABLANT, N. *et al.* Investigation of the neoclassical ambipolar electric field in ion-root plasmas on W7-X. *Nuclear Fusion* **60**, 036021. doi:10.1088/1741-4326/ab6ea8 (2020).
 92. FORD, O. P. *et al.* Charge exchange recombination spectroscopy at Wendelstein 7-X. *Review of Scientific Instruments* **91**, 023507. doi:10.1063/1.5132936 (2020).
 93. CARRALERO, D. *et al.* Characterization of the radial electric field and edge velocity shear in Wendelstein 7-X. *Nuclear Fusion*. doi:10.1088/1741-4326/ab9885 (2020).
 94. ITOH, K., HALLATSCHKE, K. & ITOH, S.-I. Excitation of geodesic acoustic mode in toroidal plasmas. *Plasma Physics and Controlled Fusion* **47**, 451–458. doi:10.1088/0741-3335/47/3/004 (2005).
 95. HELANDER, P. *et al.* Oscillations of zonal flows in stellarators. *Plasma Physics and Controlled Fusion* **53**, 054006. doi:10.1088/0741-3335/53/5/054006 (2011).
 96. MISHCHENKO, A., HELANDER, P. & KÖNIES, A. Collisionless dynamics of zonal flows in stellarator geometry. *Physics of Plasmas* **15**, 072309. doi:10.1063/1.2963085 (2008).

97. MONREAL, P. *et al.* Semianalytical calculation of the zonal-flow oscillation frequency in stellarators. *Plasma Physics and Controlled Fusion* **59**, 065005. doi:10.1088/1361-6587/aa6990 (2017).
98. ALONSO, J. A. *et al.* Observation of Oscillatory Radial Electric Field Relaxation in a Helical Plasma. *Physical Review Letters* **118**, 185002. doi:10.1103/PhysRevLett.118.185002 (2017).
99. XANTHOPOULOS, P. *et al.* Zonal Flow Dynamics and Control of Turbulent Transport in Stellarators. *Physical Review Letters* **107**, 245002. doi:10.1103/PhysRevLett.107.245002 (2011).
100. WANG, H. Y. *et al.* Global gyrokinetic particle simulations of microturbulence in W7-X and LHD stellarators. *Physics of Plasmas* **27**, 082305. doi:10.1063/5.0014198 (2020).
101. NICOLAU, J. H. *et al.* Global gyrokinetic simulation with kinetic electron for collisionless damping of zonal flow in stellarators. *Nuclear Fusion* **61**, 126041. doi:10.1088/1741-4326/ac31da (2021).
102. FUJISAWA, A. A review of zonal flow experiments. *Nuclear Fusion* **49**, 013001. doi:10.1088/0029-5515/49/1/013001 (2008).
103. ALONSO, J. A. *et al.* Dynamic transport regulation by zonal flow-like structures in the TJ-II stellarator. *Nuclear Fusion* **52**, 063010. doi:10.1088/0029-5515/52/6/063010 (2012).
104. FUJISAWA, A. *et al.* Identification of Zonal Flows in a Toroidal Plasma. *Physical Review Letters* **93**, 165002. doi:10.1103/PhysRevLett.93.165002 (2004).
105. GRULKE, O. & KLINGER, T. in *Plasma Physics: Confinement, Transport and Collective Effects* (eds DINKLAGE, A. *et al.*) 375–397 (Springer, Berlin, Heidelberg, 2005). doi:10.1007/11360360_14.
106. BRETZ, N. Diagnostic instrumentation for microturbulence in tokamaks. *Review of Scientific Instruments* **68**, 2927–2964. doi:10.1063/1.1148387 (1997).
107. KILLER, C. *et al.* Turbulent transport in the scrape-off layer of Wendelstein 7-X. *Nucl. Fusion* **61**, 096038. doi:10.1088/1741-4326/ac1ae3 (2021).

-
108. KILLER, C. Reciprocating probe measurements in the test divertor operation phase of W7-X. *submitted to Plasma Phys. Control. Fusion* (2021).
 109. WINDISCH, T. *et al.* Phased array Doppler reflectometry at Wendelstein 7-X. *Review of Scientific Instruments* **89**, 10H115. doi:10.1063/1.5039287 (2018).
 110. WEIR, G. M. *et al.* A comparison of measurements from radial and poloidal correlation ECE diagnostics on Wendelstein 7-X in *Europhysics Conference Abstracts (ECA) 45th EPS Conference on Plasma Physics*. **42A** (European Physical Society (EPS), Prague, Czech Republic, 2018), 1. <http://ocs.ciemat.es/EPS2018ABS/pdf/P2.1107.pdf>.
 111. WINDISCH, T. *et al.* Poloidal correlation reflectometry at W7-X: radial electric field and coherent fluctuations. *Plasma Physics and Controlled Fusion* **59**, 105002. doi:10.1088/1361-6587/aa759b (2017).
 112. EDLUND, E. M. *et al.* Overview of the Wendelstein 7-X phase contrast imaging diagnostic. *Review of Scientific Instruments* **89**, 10E105. doi:10.1063/1.5038804 (2018).
 113. BÖTTGER, L.-G. *Phase Contrast Imaging: A Turbulence Diagnostic for the Wendelstein 7-X Stellarator* PhD thesis (Technical University of Denmark, Kgs. Lyngby, Denmark, 2019). 131 pages.
 114. HUANG, Z. *et al.* The Wendelstein 7-X phase contrast imaging diagnostic. *Journal of Instrumentation* **16**, P01014. doi:10.1088/1748-0221/16/01/P01014 (2021).
 115. ZERNIKE, V. F. Beugungstheorie des Schneidverfahrens und seiner verbesserten Form, der Phasenkontrastmethode. *Physica* **1**, 689–704. doi:10.1016/S0031-8914(34)80259-5 (1934).
 116. NOBEL PRIZE OUTREACH, A. *The Nobel Prize in Physics 1953* nobelprize.org. <https://www.nobelprize.org/prizes/physics/1953/summary/>.
 117. PRESBY, H. M. & FINKELSTEIN, D. Plasma Phasography. *Review of Scientific Instruments* **38**, 1563–1572. doi:10.1063/1.1720602 (1967).

118. WEISEN, H. The phase contrast method as an imaging diagnostic for plasma density fluctuations (invited). *Review of Scientific Instruments* **59**, 1544–1549. doi:10.1063/1.1140193 (1988).
119. CODA, S., PORKOLAB, M. & CARLSTROM, T. N. A phase contrast interferometer on DIII-D. *Review of Scientific Instruments* **63**, 4974–4976. doi:10.1063/1.1143516 (1992).
120. CODA, S. *An experimental study of turbulence by phase-contrast imaging in the DIII-D tokamak* PhD thesis (Massachusetts Institute of Technology, Cambridge, MA, USA, 1997).
121. PORKOLAB, M. *et al.* Phase contrast imaging of waves and instabilities in high temperature magnetized fusion plasmas. *IEEE Transactions on Plasma Science* **34**, 229–234. doi:10.1109/TPS.2006.872181 (2006).
122. DORRIS, J. R., ROST, J. C. & PORKOLAB, M. Localized measurement of short wavelength plasma fluctuations with the DIII-D phase contrast imaging diagnostic. *Review of Scientific Instruments* **80**, 023503. doi:10.1063/1.3065094 (2009).
123. DORRIS, J. R. *Phase Contrast Imaging Measurements and Modeling of Short Wavelength Turbulence in the DIII-D Tokamak* PhD thesis (Massachusetts Institute of Technology, 2010).
124. DAVIS, E. M. *A combined phase contrast imaging and heterodyne interferometer system for multiscale fluctuation measurements on DIII-D* PhD thesis (Massachusetts Institute of Technology, Cambridge, MA, USA, 2018).
125. MAZURENKO, A. *Phase Contrast Imaging on the Alcator C-Mod tokamak* PhD thesis (Massachusetts Institute of Technology, Cambridge, MA, USA, 2001).
126. LIN, L. *et al.* Studies of turbulence and transport in Alcator C-Mod H-mode plasmas with phase contrast imaging and comparisons with GYRO. *Physics of Plasmas* **16**, 012502. doi:10.1063/1.3057420 (2009).
127. EDLUND, E. M. *A Study of Reversed Shear Alfvén Eigenmodes in Alcator C-Mod with Phase Contrast Imaging* PhD thesis (Massachusetts Institute of Technology, Cambridge, MA, USA, 2009).

-
128. MARINONI, A. *et al.* Design of a tangential phase contrast imaging diagnostic for the TCV tokamak. *Review of Scientific Instruments* **77**, 10E929. doi:10.1063/1.2222333 (2006).
 129. HUANG, Z. *Experimental study of plasma turbulence in the TCV tokamak* PhD thesis (École Polytechnique Fédérale de Lausanne, 2017).
 130. GONG, S. B. *et al.* Design of phase contrast imaging on the HL-2A tokamak. *Fusion Engineering and Design. Proceedings of the 29th Symposium on Fusion Technology (SOFT-29) Prague, Czech Republic, September 5-9, 2016* **123**, 802–806. doi:10.1016/j.fusengdes.2017.04.072 (2017).
 131. TANAKA, K. *et al.* Phase contrast imaging interferometer for edge density fluctuation measurements on LHD. *Review of Scientific Instruments* **74**, 1633–1637. doi:10.1063/1.1538361 (2003).
 132. TANAKA, K. *et al.* Two-dimensional phase contrast imaging for local turbulence measurements in large helical device (invited). *Review of Scientific Instruments* **79**, 10E702. doi:10.1063/1.2988821 (2008).
 133. BÄHNER, J.-P. *et al.* Phase contrast imaging measurements and numerical simulations of turbulent density fluctuations in gas-fuelled ECRH discharges in Wendelstein 7-X. *Journal of Plasma Physics* **87**. doi:10.1017/S0022377821000635 (2021).
 134. SWANSON, D. G. *Plasma Waves, 2nd Edition* 960 pages (CRC Press, 2003).
 135. LO, E. *et al.* Calibration and test of the tangential phase contrast imaging diagnostic on CDX-U. *Review of Scientific Instruments* **68**, 1206–1216. doi:10.1063/1.1147883 (1997).
 136. YU, Y. *et al.* Calibration of phase contrast imaging on HL-2A Tokamak. *Journal of Instrumentation* **12**, C10005–C10005. doi:10.1088/1748-0221/12/10/C10005 (2017).
 137. KINOSHITA, T. *et al.* Determination of absolute turbulence amplitude by CO₂ laser phase contrast imaging. *Journal of Instrumentation* **15**, C01045–C01045. doi:10.1088/1748-0221/15/01/C01045 (2020).

138. XANTHOPOULOS, P. *et al.* Controlling Turbulence in Present and Future Stellarators. *Physical Review Letters* **113**, 155001. doi:10.1103/PhysRevLett.113.155001 (2014).
139. HANSEN, S. K. *et al.* Development of a synthetic phase contrast imaging diagnostic for Wendelstein 7-X. *submitted to Plasma Phys. Control. Fusion*, 35 (2022).
140. ROST, J. C., LIN, L. & PORKOLAB, M. Development of a synthetic phase contrast imaging diagnostic. *Physics of Plasmas* **17**, 062506. doi:10.1063/1.3435217 (2010).
141. RABINER, L. R. & GOLD, B. *Theory and application of digital signal processing* 1st edition (Prentice Hall, New Jersey, 1975).
142. STOICA, P. & MOSES, R. L. *Spectral analysis of signals* 452 pages (Pearson/Prentice Hall, Upper Saddle River, N.J, 2005).
143. WELCH, P. The use of fast Fourier transform for the estimation of power spectra: A method based on time averaging over short, modified periodograms. *IEEE Transactions on Audio and Electroacoustics* **15**, 70–73. doi:10.1109/TAU.1967.1161901 (1967).
144. ROSENBLATT, M. Remarks on Some Nonparametric Estimates of a Density Function. *The Annals of Mathematical Statistics* **27**, 832–837. doi:10.1214/aoms/1177728190 (1956).
145. PARZEN, E. On Estimation of a Probability Density Function and Mode. *The Annals of Mathematical Statistics* **33**, 1065–1076. doi:10.1214/aoms/1177704472 (1962).
146. BLACKMAN, R. B. & TUKEY, J. W. *The Measurement of Power Spectra: From the Point of View of Communications Engineering* (Dover, New York, 1959).
147. BUTTKUS, B. in *Spectral Analysis and Filter Theory in Applied Geophysics* 1st edition (Springer, Berlin, Heidelberg, 2000). https://doi.org/10.1007/978-3-642-57016-2_10.
148. GÖRLER, T. & JENKO, F. Multiscale features of density and frequency spectra from nonlinear gyrokinetics. *Physics of Plasmas* **15**, 102508. doi:10.1063/1.3006086 (2008).

-
149. PÉCSELI, H. L. Spectral properties of electrostatic drift wave turbulence in the laboratory and the ionosphere. *Annales Geophysicae* **33**, 875–900. doi:10.5194/angeo-33-875-2015 (2015).
 150. BALDZUHN, J. *et al.* Pellet fueling experiments in Wendelstein 7-X. *Plasma Physics and Controlled Fusion* **61**, 095012. doi:10.1088/1361-6587/ab3567 (2019).
 151. WEGNER, T. *et al.* Impact of the temperature ratio on turbulent impurity transport in Wendelstein 7-X. *Nuclear Fusion*. doi:10.1088/1741-4326/abb869 (2020).
 152. BRUNNER, K. J. *et al.* Real-time dispersion interferometry for density feedback in fusion devices. *Journal of Instrumentation* **13**, P09002–P09002. doi:10.1088/1748-0221/13/09/P09002 (2018).
 153. BOZHENKOV, S. A. *et al.* Plasma performance in high-density and high-confinement regimes in Wendelstein 7-X in *Europhysics Conference Abstracts (ECA) 46th EPS Conference on Plasma Physics*. **43C** (European Physical Society (EPS), Milan, Italy, 2019), 1. <http://ocs.ciemat.es/EPS2019ABS/pdf/03.105.pdf>.
 154. HIRSCH, M. *et al.* ECE Diagnostic for the initial Operation of Wendelstein 7-X. *EPJ Web of Conferences* **203**, 03007. doi:10.1051/epjconf/201920303007 (2019).
 155. PABLANT, N. A. *et al.* Core radial electric field and transport in Wendelstein 7-X plasmas. *Physics of Plasmas* **25**, 022508. doi:10.1063/1.4999842 (2018).
 156. PASCH, E. *et al.* The Thomson scattering system at Wendelstein 7-X. *Review of Scientific Instruments* **87**, 11E729. doi:10.1063/1.4962248 (2016).
 157. CONWAY, G. D. *et al.* Mean and Oscillating Plasma Flows and Turbulence Interactions across the L-H Confinement Transition. *Physical Review Letters* **106**, 065001. doi:10.1103/PhysRevLett.106.065001 (2011).
 158. HIRSHMAN, S. P. *et al.* Plasma transport coefficients for nonsymmetric toroidal confinement systems. *The Physics of Fluids* **29**, 2951–2959. doi:10.1063/1.865495 (1986).

159. TURKIN, Y. *et al.* Neoclassical transport simulations for stellarators. *Physics of Plasmas* **18**, 022505. doi:10.1063/1.3553025 (2011).
160. WINDISCH, T. *et al.* W-band Doppler reflectometry at Wendelstein 7-X: Diagnostic setup and initial results in 14th Intl. Reflectometry Workshop 14th Intl. Reflectometry Workshop (Lausanne, 2019), 9. <https://www.aug.ipp.mpg.de/IRW/IRW14/papers/207-IRW14-Windisch-paper.pdf>.
161. ESTRADA, T. *et al.* Radial electric field and density fluctuations measured by Doppler reflectometry during the post-pellet enhanced confinement phase in W7-X. *Nuclear Fusion* **61**, 046008. doi:10.1088/1741-4326/abddee (2021).
162. JOST, G. *et al.* Global linear gyrokinetic simulations in quasi-symmetric configurations. *Physics of Plasmas* **8**, 3321–3333. doi:10.1063/1.1374585 (2001).
163. SÁNCHEZ, E. *et al.* Nonlinear gyrokinetic PIC simulations in stellarators with the code EUTERPE. *Journal of Plasma Physics* **86**. doi:10.1017/S0022377820000926 (2020).
164. FU, J. Y. *et al.* Global gyrokinetic simulation of neoclassical ambipolar electric field and its effects on microturbulence in W7-X stellarator. *Physics of Plasmas* **28**, 062309. doi:10.1063/5.0047291 (2021).
165. BALLINGER, S. B. *et al.* Dynamics and dependencies of the configuration-dependent 1–2 kHz fluctuation in W7-X. *Nuclear Materials and Energy* **27**, 100967. doi:10.1016/j.nme.2021.100967 (2021).
166. COLCHIN, R. J. *et al.* The Filterscope. *Review of Scientific Instruments* **74**, 2068–2070. doi:10.1063/1.1537038 (2003).
167. BRANDT, C. *et al.* Installation of the soft X-ray multi-camera tomography system (XMCTS) in the Wendelstein 7-X stellarator. *Fusion Engineering and Design. Proceedings of the 29th Symposium on Fusion Technology (SOFT-29) Prague, Czech Republic, September 5-9, 2016* **123**, 887–891. doi:10.1016/j.fusengdes.2017.02.111 (2017).

-
168. BRANDT, C. *et al.* Soft x-ray tomography measurements in the Wendelstein 7-X stellarator. *Plasma Physics and Controlled Fusion* **62**, 035010. doi:10.1088/1361-6587/ab630d (2020).
 169. ENDLER, M. *et al.* Engineering design for the magnetic diagnostics of Wendelstein 7-X. *Fusion Engineering and Design* **100**, 468–494. doi:10.1016/j.fusengdes.2015.07.020 (2015).
 170. RAHBARNIA, K. *et al.* Alfvénic fluctuations measured by in-vessel Mirnov coils at the Wendelstein 7-X stellarator. *Plasma Physics and Controlled Fusion* **63**, 015005. doi:10.1088/1361-6587/abc395 (2020).
 171. WURDEN, G. A. *et al.* *Structure of island localized modes in Wendelstein 7-X* in. 46th EPS Conference on Plasma Physics (European Physical Society (EPS), Milan, 2019), 4. https://pure.mpg.de/rest/items/item_3168993/component/file_3317968/content.
 172. SCHILLING, J. *et al.* Soft x-ray tomograms are consistent with the magneto-hydrodynamic equilibrium in the Wendelstein 7-X stellarator. *Plasma Physics and Controlled Fusion* **63**, 055010. doi:10.1088/1361-6587/abe0fa (2021).
 173. CARRALERO, D. *et al.* An experimental characterization of core turbulence regimes in Wendelstein 7-X. *Nuclear Fusion*. doi:10.1088/1741-4326/ac112f (2021).

Acronyms

Engineering

LOS line of sight

General Physics

IR infrared

SXR soft X-ray

MCF magnetic confinement fusion

Nuclear Fusion Experiments

CHS compact helical system

HL-2A Huan-Liuqi-2A

TCA Tokamak Chauffage Alfvén

TJ-II Tokamak de la Junta II

Alcator C-Mod Alto Campo Toro C-Mod

DIII-D Doublet III-D

LHD large helical device

TCV Tokamak à configuration variable

W7-X Wendelstein 7-X

Nuclear Fusion Machine Components

NBI neutral beam injection

Optics

CW continuous wave

OAP off-axis parabolic

Plasma Diagnostics

CXRS charge exchange recombination spectroscopy

MPM Multi-purpose manipulator

TS Thomson scattering

XICS X-ray imaging crystal spectroscopy

XMCTS soft X-ray Multi Camera Tomography System

Plasma Physics

ECE electron cyclotron emission

ECRH electron cyclotron resonance heating

ICRH ion cyclotron radiation heating

SOL scrape-off layer

Plasma Physics Laboratories

IPP Max-Planck Institute for Plasma Physics

PSFC MIT Plasma Science and Fusion Center

Plasma Theory

LCFS last closed flux surface

MHD magnetohydrodynamic

NC neoclassical

Plasma Theory Codes

DKES drift kinetic equation solver

GENE gyrokinetic electromagnetic numerical experiment

GENE-3D 3-dimensional expansion of GENE

GTC gyrokinetic toroidal code

VMEC variational moments equilibrium code

Plasma Turbulence Diagnostics

BES beam emission spectroscopy

CECE correlation ECE

DBS Doppler back-scattering

ECEI ECE imaging

GPI gas puff imaging

HIBP heavy ion beam probe

PCI phase contrast imaging

PCR poloidal correlation reflectometer

SPCI synthetic PCI

Plasma Turbulence Theory

ETG electron-temperature-gradient-driven

GAM geodesic acoustic mode

ITEM ion-driven TEM

ITG ion-temperature-gradient-driven

RH Rosenbluth-Hinton

TEM trapped-electron mode

ZF zonal flow

Signal Processing

(k, f) wavenumber-frequency

CSD cross power spectral density

DFT discrete Fourier transform

FFT fast Fourier transform

FT Fourier transform

IDFT inverse discrete Fourier transform

PSD power spectral density

RMS root mean square

SNR signal-to-noise ratio

STFT short-time Fourier transform

Statistics

KDE kernel density estimate

Thesis specific acronyms

LH- ι low and high ι

M- ι medium range ι

List of Figures

1.1	Tokamak and stellarator concept.	3
2.1	Energy cascade in 3D turbulence.	8
2.2	Dual-cascade in 2D turbulence.	9
2.3	Neoclassical transport regimes in tokamaks.	13
2.4	Neoclassical transport regimes in stellarators.	14
2.5	Mixing length approach to turbulent transport.	16
2.6	Turbulence interaction in fusion plasmas.	18
2.7	Wendelstein 7-X	19
2.8	5-fold symmetry of W7-X with different cross sections.	21
2.9	ι -profiles of W7-X magnetic configurations.	22
3.1	Typical micro-instability growth rate spectra in tokamaks.	31
3.2	Drift wave and interchange mechanism.	32
3.3	Curvature drive of the interchange instability.	35
3.4	ITG mode growth rate increase with a/L_{T_i} and T_e/T_i	41
3.5	Linear ITG & TEM growth rate and frequency spectra.	42
3.6	Impact of ETG on linear growth rates.	43
3.7	Impact of density gradient on linear ETG growth rates.	44
3.8	Typical radial profiles of plasma parameters during in W7-X.	47
3.9	Radial evolution of micro-instabilities in W7-X.	48
3.10	ITG vs. TEM	49
3.11	Simulated growth rate spectra at different radii.	50
3.12	Illustration of zonal flows on Jupiter and in W7-X.	52
3.13	Zonal flow decorrelation and thinning of vortices.	53
4.1	Principle phase contrast imaging diagnostic setup.	59
4.2	Setup of the PCI diagnostic at W7-X.	62
4.3	Schematic of a sound wave measurement for calibration.	64

List of Figures

4.4	20 kHz sound wave measurement by PCI.	64
4.5	2D measurement of the speaker sound field.	66
4.6	3D view of the W7-X $r_{\text{eff}}/a = 0.75$ flux surface with normal curvature and flux tubes.	67
4.7	Simulated density fluctuations along flux tubes.	68
4.8	Frequency response function of a detector element.	72
4.9	Typical PCI wavenumber-frequency-spectrum.	75
4.10	Sound wave (k, f) - and wavenumber-spectrum.	76
4.11	Example plots illustrating the v_{ph} determination method.	79
4.12	Laser beam profile during sound wave and plasma measurements.	82
5.1	Wavenumber-frequency spectrum of a W7-X standard configuration ECRH plasma.	90
5.2	Frequency-spectrum of a W7-X standard configuration ECRH plasma.	91
5.3	Wavenumber spectrum of a W7-X standard configuration ECRH plasma.	91
5.4	Wavenumber spectrum with spectral indices.	92
5.5	Normalised wavenumber-frequency-spectrum of a W7-X standard configuration ECRH plasma.	95
5.6	Example spectrogram and fluctuation amplitude.	97
5.7	Density fluctuation amplitude of ECRH discharge segments.	97
5.8	Density fluctuation amplitude versus line-integrate density.	98
5.9	Density fluctuation amplitude versus electron-ion energy exchange rate.	100
5.10	Fluctuation levels vs density peaking and temperature ratio in standard configuration.	101
5.11	Fluctuation levels vs density peaking and temperature ratio in high iota configuration.	102
5.12	Wavenumber spectra for standard and high iota configuration.	103
6.1	Discharge overview of a typical ECRH discharge in W7-X.	107
6.2	Radial profiles of plasma parameters during in the reference discharge.	108

6.3	Wavenumber-frequency spectrum during an ECRH plasma in W7-X standard magnetic configuration. Modified from BÄHNER <i>et al.</i> [133].	108
6.4	E_r from NC DKES simulations and DBS measurements. . .	111
6.5	Direct comparison of $\mathbf{E} \times \mathbf{B}$ -velocity to dominant poloidal velocity of fluctuations.	113
6.6	Wavenumber-frequency-spectra and E_r of forward and reversed field experiments.	114
6.7	Velocity comparison for forward and reversed field experiments.	115
6.8	Velocity comparison for scan of input power.	116
6.9	Velocity comparison for density scan.	117
6.10	Model velocity and density fluctuation profiles for SPCI. . .	118
6.11	Wavenumber-frequency spectra by SPCI for increasing radial gradient of the poloidal velocity.	119
6.12	Radial profile of \tilde{n}_e from GENE-3D and $v_{\mathbf{E} \times \mathbf{B}}$ from DKES for SPCI model.	120
6.13	Simplified rotation model output for GENE-3D density fluctuations and DKES E_r	121
6.14	Flux tube intersections along the LOS of PCI.	122
6.15	Density fluctuation amplitude from GENE simulations and ITG along minor radius.	123
6.16	Comparison of simulated neoclassical and turbulent ion heat flux.	124
7.1	Example of dominant phase velocity oscillation.	128
7.2	Example time traces of PCI dominant phase velocity.	130
7.3	Coherence and correlation of dominant phase velocity and density fluctuation amplitude.	131
7.4	Coherence of dominant phase velocity and H_α -radiation. . .	133
7.5	Cross-correlation of dominant phase velocity and H_α	134
7.6	CSD and cross-phase of dominant phase velocity and H_α . . .	135
7.7	CSD and cross-phase of outboard and inboard dominant phase velocity.	136
7.8	Cross-correlation of outboard and inboard dominant phase velocity.	137
7.9	Coherence of dominant phase velocity and magnetic perturbations.	138

7.10	Coherence of dominant phase velocity and SXR emission. . .	139
7.11	Tomograms of SXR emission.	140
7.12	Temporal evolution of poloidal mode decomposition during 1-2 kHz feature.	141
7.13	Velocity comparison for high mirror and high iota configuration.	144
7.14	Zonal component of electric potential from a global gyrokin- etic simulation.	147
7.15	Radial structure of zonal potential and corresponding radial electric field.	148
7.16	Model E_r -profiles for the simplified rotation model of SPCI.	149
7.17	SPCI wavenumber-frequency spectra for different ZF rotation models.	150

Statutory declaration

Eigenständigkeitserklärung

Hiermit erkläre ich, dass diese Arbeit bisher von mir weder an der Mathematisch-Naturwissenschaftlichen Fakultät der Universität Greifswald noch einer anderen wissenschaftlichen Einrichtung zum Zwecke der Promotion eingereicht wurde. Ferner erkläre ich, dass ich diese Arbeit selbstständig verfasst und keine anderen als die darin angegebenen Hilfsmittel und Hilfen benutzt und keine Textabschnitte eines Dritten ohne Kennzeichnung übernommen habe.

Greifswald, 24.01.2022

JAN-PETER BÄHNER

Acknowledgements

Being given the opportunity to work on this project within the impressive team of Wendelstein 7-X was an honouring and humbling experience. It has been a challenging time, not least because we were hit by a global pandemic. But with the help of my coworkers, friends and family, this project came to a successful end and I will always be grateful for their support.

First, my gratitude goes to my supervisors. To Dr. Adrian von Stechow, my day-to-day supervisor, oracle for questions of all sorts and with whom working on the diagnostic is always a pleasure. To Prof. Olaf Grulke, my scientific supervisor, who kept track of every little turn of the project, making sure it will end up somewhere fruitful with his guidance. Having survived three years of his thorough feedback, I fear nothing ahead. To Prof. Thomas Klinger, my academic supervisor, who somehow knows exactly when advice or encouragement is needed and is always happy to provide it. Next, I need to thank the group around the PCI diagnostic including Dr. Zhouji Huang, Dr. Søren K. Hansen, Dr. Lukas-Georg Böttger, Dr. Eric M. Edlund and Prof. Miklos Porkolab. Working in this group really feels like being part of a team and each member contributed greatly to this project. I would like to thank Dr. Jorge A. Alcusón, who supported me in every aspect regarding the gyrokinetic simulations and made working with theory seem like fun. Furthermore, thanks go out to Dr. Gabriel G. Plunk for discussing the theoretical interpretation of results. There are many more people within the turbulence group and the entire Wendelstein 7-X team, who supported me with advice, data or feedback and I would like to thank them all. It is truly exceptional how one can feel that everyone in this institute is working towards one goal.

I feel a great deal of gratitude for all my friends and my family, who endured the stressful and difficult times with me and celebrated every one

Acknowledgements

of my accomplishments. This includes the many wonderful people I met during my time in Greifswald as well as my friends from home, from Aachen and from London. The past two years have been hard on us and I can not express how important each of you is for me. To my family, my rock in turbulent fluids: zu wissen, dass ihr immer für mich da seid, mein zu Hause und Fels in der Brandung, und immer stolz auf mich — das ist für mich unersetzlich und war unfassbar wichtig in den letzten Jahren.

This work has been carried out within the framework of the EUROfusion Consortium, funded by the European Union via the Euratom Research and Training Programme (Grant Agreement No 633053 & 101052200 — EUROfusion). Views and opinions expressed are however those of the author only and do not necessarily reflect those of the European Union or the European Commission. Neither the European Union nor the European Commission can be held responsible for them.